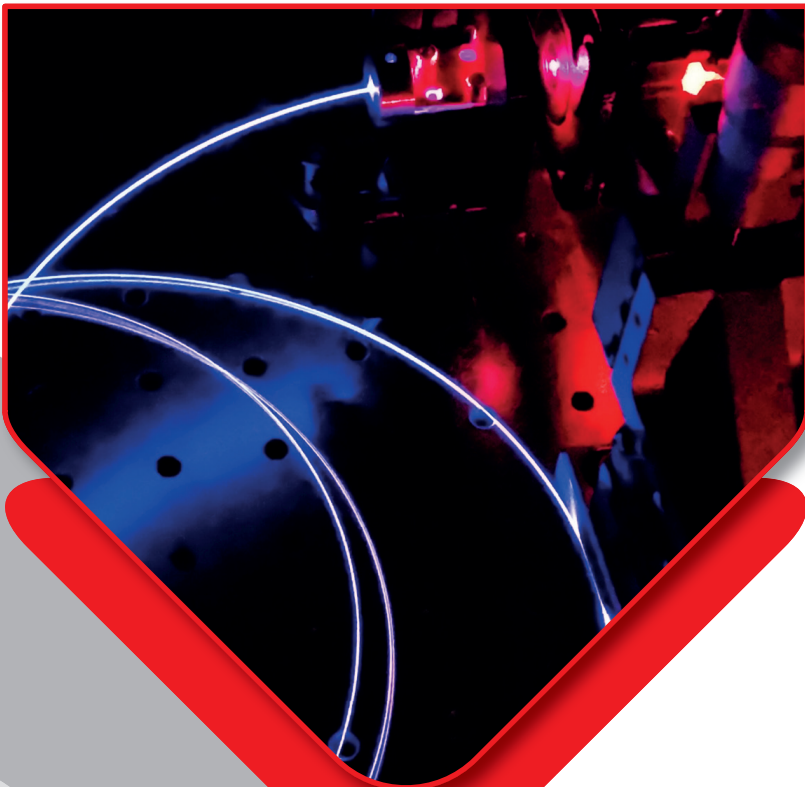


# Thulium:Holmium-Co-Doped Fiber Lasers

Power Scaling and Long-Wavelength Emission





Patrick Forster

## **Thulium:Holmium-Co-Doped Fiber Lasers**

Power Scaling and Long-Wavelength Emission

Lasers and Optronics:  
Materials, Technologies and Applications  
**Volume 1.2024**

Editor: Prof. Dr. rer. nat. habil. Marc Eichhorn

Professur für Optronik am  
Karlsruher Institut für Technologie (KIT)

Fraunhofer-Institut für Optronik, Systemtechnik  
und Bildauswertung (IOSB)

# Thulium:Holmium-Co-Doped Fiber Lasers

Power Scaling and Long-Wavelength Emission

by  
Patrick Forster

Karlsruher Institut für Technologie  
Institut für Regelungs- und Steuerungssysteme

Thulium:Holmium-Co-Doped Fiber Lasers:  
Power Scaling and Long-Wavelength Emission

Zur Erlangung des akademischen Grades eines Doktors der  
Ingenieurwissenschaften von der KIT-Fakultät für Elektrotechnik und  
Informationstechnik des Karlsruher Instituts für Technologie (KIT)  
genehmigte Dissertation

von Patrick Forster, M. Sc.

Tag der mündlichen Prüfung: 9. November 2023  
Referent: Prof. Dr. rer. nat. habil. Marc Eichhorn  
Korreferent: Prof. Dr. rer. nat. Uli Lemmer

#### Impressum



Karlsruhe Institute of Technology (KIT)  
Kaiserstraße 12  
76131 Karlsruhe  
Institute of Control Systems  
[www.irs.kit.edu](http://www.irs.kit.edu)



*This document – excluding parts marked otherwise, the cover, pictures and graphs –  
is licensed under a Creative Commons Attribution-Share Alike 4.0 International License  
(CC BY-SA 4.0): <https://creativecommons.org/licenses/by-sa/4.0/deed.en>*



*The cover page is licensed under a Creative Commons  
Attribution-No Derivatives 4.0 International License (CC BY-ND 4.0):  
<https://creativecommons.org/licenses/by-nd/4.0/deed.en>*

2024

Print: Campus Services (CSE) – Medienproduktion  
100 % recycled paper with the quality label „Der Blaue Engel“

ISSN 2943-2308

DOI 10.5445/IR/1000169153







# Thulium:Holmium-Co-Doped Fiber Lasers Power Scaling and Long-Wavelength Emission

Zur Erlangung des akademischen Grades eines  
DOKTORS DER INGENIEURWISSENSCHAFTEN (Dr.-Ing.)

von der KIT-Fakultät für Elektrotechnik und Informationstechnik des  
Karlsruher Instituts für Technologie (KIT)  
angenommene

DISSERTATION

von

Patrick Forster, M. Sc.

geboren am 19.02.1992 in Memmingen

Tag der mündlichen Prüfung: 09.11.2023

Hauptreferent: Prof. Dr. rer. nat. habil. Marc Eichhorn

Korreferent: Prof. Dr. rer. nat. Uli Lemmer



# Zusammenfassung

Ein wesentlicher Bestandteil der aktuellen Laserforschung befasst sich mit der Leistungsskalierung und Erzeugung neuer Emissionswellenlängen zur schrittweisen Schließung der Lücken im elektromagnetischen Spektrum der optischen Strahlung. Die Grundlage für die Erzeugung direkter Laserstrahlung in einem bestimmten Wellenlängenbereich liegt in geeigneten aktiven Materialien. Die eingeschränkte Verfügbarkeit dieser aktiven Materialien schränkt die möglichen zu erzeugenden Wellenlängen bereits stark ein.

Zwei Wellenlängenbereiche, die sich gerade aufgrund eines breiten potentiellen Einsatzbereiches aus einer Nische heraus entwickeln, befinden sich bei  $2\ \mu\text{m}$  und  $3\text{--}5\ \mu\text{m}$ . Durch das Abdecken von atmosphärischen Transmissionsfenstern und verschiedenen Absorptionsbanden zeigt sich die Strahlung als hochinteressant für Anwendungen wie z.B. der Fernerkundung, der Kunststoffbearbeitung oder der Medizin. Während es im  $2\ \mu\text{m}$  Bereich noch geeignete aktive Materialien in Kombination mit passenden Wirtsmaterialien gibt, die sich hervorragend für den Hochleistungsbereich eignen, wie mit seltenen Erden dotierten Silika Glasfasern, ist dies im mittleren Infrarotbereich von  $3\text{--}5\ \mu\text{m}$  nicht mehr der Fall. Als Alternative kann hier auf nichtlineare Konversion zurückgegriffen werden, wobei  $2\ \mu\text{m}$  Laserquellen bereits das Potential gezeigt haben als Pumpquelle zu dienen. Sowohl für die direkten Anwendungen als auch die indirekte Anwendung des Laserlichts für die nichtlineare Konversion ist das Erzeugen von längerer  $2\ \mu\text{m}$  Strahlung ( $\geq 2,09\ \mu\text{m}$ ) essentiell und bietet im Vergleich zu den etwas kürzeren Wellenlängen ( $< 2,09\ \mu\text{m}$ ) erhebliche Vorteile. Die beiden Zugpferde im  $2\ \mu\text{m}$  Faserlaserbereich basierend auf Thulium und Holmium kommen jedoch bei den angedachten Wellenlängen an ihre Grenzen oder sind schlichtweg ungeeignet für kompakte Aufbauten. Dies stellt die Leistungsskalierung im langwelligen  $2\ \mu\text{m}$  Bereich vor enorme Herausforderungen.

Die durchgeführte Arbeit beschäftigt sich mit der Untersuchung von Tm:Ho-kodotierten Faserlasern zur Leistungsskalierung des Wellenlängenbereichs  $\geq 2,09 \mu\text{m}$ . Ausgehend von der grundlegenden Idee vereinigt dieser Fasertyp die Vorteile von Thulium und Holmium Fasern und sollte daher hervorragend geeignet sein für eine kompakte Laserlichterzeugung in diesem Wellenlängenbereich. Die kodotierte Faser wird jedoch normalerweise gemieden, da die Herstellung der Ionenzusammensetzung innerhalb des Kerns kompliziert ist und diese zu einem hohen zu erwartenden Wärmeeintrag führt.

**Kapitel 1** gibt einen Überblick über mögliche Anwendungen von Faserlaser-Quellen im  $2 \mu\text{m}$  Bereich und im speziellen für Laserstrahlung  $\geq 2,09 \mu\text{m}$ . Die momentan verwendeten Faserlaser basierend auf Thulium und Holmium Ionen werden kurz mit ihren Vor- und Nachteilen vorgestellt. Dabei wird deutlich, dass der erwähnte langwellige  $2 \mu\text{m}$  Bereich im Moment nicht effizient, nur mit relativ aufwendigen Aufbauten und auch nur mit relativ geringer Leistung adressiert werden kann. Als mögliche Lösung dieses Problems wird ein meist vernachlässigter Faserlaser aufbauend auf einer Thulium:Holmium-kodotierten Faser (THF) untersucht. Die Vor- und Nachteile dieses Fasertyps werden ebenfalls vorgestellt. Im weiteren Teil der Arbeit wird das Potential neuartiger kodotierten Fasern ermittelt.

In **Kapitel 2** werden die theoretischen Grundlagen der Arbeit gelegt. Dieser Abschnitt ist zweigeteilt. Primär wird auf den Faserlaser an sich eingegangen, wobei verschiedene Laserkonzepte, die verwendeten aktiven Ionen, das Laserprinzip und die Güteschaltung erläutert werden. Der zweite Teil befasst sich mit den Grundlagen der nichtlinearen Optik. Diese werden für die Realisierung eines optischen parametrischen Oszillators benötigt, der die gepulste  $2 \mu\text{m}$  Strahlung ins mittlere Infrarot ( $3\text{--}5 \mu\text{m}$ ) konvertiert. Dafür ist das Verständnis für einen effizienten nichtlinearen Prozess, also die Auswirkungen einer ungenügenden Phasenanpassung, von essentieller Bedeutung. Dies hat direkten Einfluss auf die Optimierung des Faserlasers und die notwendigen optischen Eigenschaften, die dieser besitzen muss.

Aufbauend auf einer sich im niedrigen Leistungsbereich bewährten Freistrahl-Laserkonfiguration wird eine erfolgreiche Leistungsskalierung vollzogen. **Kapitel 3** stellt kurz den ursprünglichen Aufbau vor und erläutert essentielle Punkte für einen Hochleistungsbetrieb. Das Kapitel bündelt alle während der Doktorarbeit vorgenommenen Optimierungen. Es werden die Schwachstellen und Probleme des Lasersystems analysiert und mögliche Lösungs- und Optimierungsvarianten dargelegt. Als besonders kritisch stellten sich die chromatischen Abbildungsfehler zwischen Pumpstrahlung und Laserlicht in der Koppellinse zur aktiven Faser heraus.

Diese führen aus mehreren Gründen zu einer starken Performanzreduktion und konnte durch die Nutzung nicht kollimierter Pumpstrahlung behoben werden. Des Weiteren wird die Faserendkonfektionierung mittels einer Faserendkappe als essentielles Laserbauelement zur Steigerung der Lasererstörschwelle am Faserausgang untersucht. Die vorhandenen Schwierigkeiten durch das direkte Verschweißen der aktiven Faser mit der Faserendkappe in Kombination mit dem üblichen Einkoppelvorgang des Pumplichts werden erläutert. Mehrere Methoden für eine stabile Faser-Endkappen Verbindung, welche die optischen Eigenschaften der Laserstrahlung nicht degradiert, werden präsentiert. Alle Optimierungen unterliegen der Prämisse eines maximal kompakten Laseraufbaus mit möglichst wenigen Komponenten.

In **Kapitel 4** werden die ersten experimentellen Ergebnisse im Dauerstrichbetrieb vorgestellt. Zuerst wird ein durchstimmbarer Laser mittels eines Beugungsgitters realisiert. Dieser soll ausgehend von verschiedenen Faserlängen aufdecken in welchem spektralen Emissionsbereich eine Leistungsskalierung durchführbar sein wird. Basierend auf diesen Erkenntnissen wird anschließend eine explizite Leistungsskalierung des Faserlasers durchgeführt. Hierfür wird anstelle des Beugungsgitters ein schmalbandiges Volumen Bragg Gitter für einen stabilen Laserbetrieb benutzt. Dabei werden wichtige optische Eigenschaften des Lasers wie die Strahlqualität, die Langzeitstabilität und das Emissionsspektrum untersucht. Sowohl für den durchstimmbaren Laser als auch für den skalierbaren Laser werden anfängliche Resultate und die Ergebnisse eines optimierten Laseraufbaus gegenübergestellt. Dadurch sind die Auswirkungen der Optimierung direkt erkennbar.

In **Kapitel 5** werden mehrere gütegeschaltene Laser im Bereich von 2,05 bis 2,2  $\mu\text{m}$  realisiert. Es wird das Verhalten des Systems in Abhängigkeit von verschiedenen Laserkomponenten untersucht. Mit diesen Erkenntnissen kann im folgenden Kapitel 6 eine für die Anwendung der nichtlinearen Konversion optimierte Laserquelle aufgebaut werden.

In **Kapitel 6** wird nun die als primär angedachte Anwendung für den THF-Laser, ein optisch parametrischer Oszillator (OPO) basierend auf dem nichtlinearen Material Zink Germanium Phosphid (ZGP), aufgebaut. Zuerst werden der Phasenanpassungswinkel und die Akzeptanzbreite des Pumpspektrums von ZGP berechnet. Anschließend werden der Aufbau des linearen OPOs und die optischen Eigenschaften der realisierten Pumpquelle, die auf den Erkenntnissen von Kapitel 5 beruht, vorgestellt. Als letzter Schritt werden OPO Experimente durchgeführt.

In **Kapitel 7** wird die Arbeit zusammengefasst und es wird ein kurzer Ausblick zu möglichen zukünftigen Themen gegeben.

Die gewonnen wissenschaftlichen Erkenntnisse und Ergebnisse zeigen zum ersten Mal, dass mit einer Tm:Ho-kodotierten Faser eine effiziente und kompakte Leistungsskalierung in einem Wellenbereich, der normalerweise nur von Holmium-dotierten Fasern erzeugt wird, möglich ist. Dies erschließt neue Möglichkeiten zur Erzeugung und Skalierung von Laserlicht im 2  $\mu\text{m}$  Bereich und zeigt, dass die selten genutzte und durchaus mit Vorurteilen behaftete Faser, neben den einfach dotierten Thulium und Holmium Fasern, einen weitaus größeren Bereich in der Forschung einnehmen kann als bisher gezeigt. Dies zeigt sich im Besonderen, wenn extreme Wellenlängen bis zu 2,2  $\mu\text{m}$  erzeugt werden sollen, wobei aktuelle Leistungswerte um den Faktor 15 überboten werden konnten. Bestehende Leistungsgrenzen, Effizienzen und Emissionsbereiche von aktuellen THF-Lasern konnten uneingeschränkt überboten genauso wie neue Bestmarken im Bereich Faserlaser gepumpte nichtlineare Konversion durch ZGP OPOs aufgestellt werden.

# Abstract

Two main aspects of the current laser research focus on power scaling and developing new emission wavelengths to bridge gaps in the electromagnetic spectrum of optical radiation. The success of this endeavor is heavily connected to suitable active materials responsible for generating direct laser radiation within specific wavelength ranges. However, the limited accessibility of these active media constrains the range of wavelengths that can be generated. Two wavelength ranges, which have emerged from a niche driven by a wide range of possible applications, are located at  $2\ \mu\text{m}$  and in the range of  $3\text{--}5\ \mu\text{m}$ . These wavelengths cover broad atmospheric transmission windows and various material absorption bands, making the dedicated radiation highly promising for remote sensing, plastic processing, and medicine applications. At  $2\ \mu\text{m}$ , there are suitable active materials in combination with matching host materials, like rare-earth-doped silica fibers, which are excellent for high-power operation. However, the mid-infrared range from  $3\text{--}5\ \mu\text{m}$  lacks this advantageous combination. As an alternative, nonlinear frequency conversion can be employed, where  $2\ \mu\text{m}$  laser sources already have proven their potential as a pump source. Both direct and indirect applications for nonlinear frequency conversion of the laser radiation necessitate the generation of long-wavelength  $2\ \mu\text{m}$  radiation ( $\geq 2.09\ \mu\text{m}$ ), which offers significant advantages compared to shorter wavelengths ( $< 2.09\ \mu\text{m}$ ). However, the two main driving forces in the  $2\ \mu\text{m}$  fiber laser domain, based on thulium and holmium, come to their limits at the intended wavelengths or are simply not suitable for compact laser design. This sets a serious challenge for the power scaling of the long-wavelength  $2\ \mu\text{m}$  region.

The accomplished work investigates Tm:Ho-codoped fiber lasers for power scaling in the wavelength region  $\geq 2.09\ \mu\text{m}$ . This type of fiber combines the advantages of both thulium and holmium fibers and is expected to be well-suited for compact laser generation at this wavelength range.

Despite this promising concept, the Tm:Ho-codoped fiber is typically avoided in current laser research due to the highly challenging manufacturing process of the ion composition inside the core and the relatively high expected thermal load within the fiber.

**Chapter 1** gives an overview of possible applications of fiber laser sources operating in the 2  $\mu\text{m}$  region, more precisely for laser radiation  $\geq 2.09 \mu\text{m}$ . The mainly utilized fiber lasers based on thulium and holmium ions are briefly introduced with their advantages and disadvantages. This demonstrates that the long-wavelength 2  $\mu\text{m}$  region is currently inefficiently addressed and shows a lower power regime than the slightly shorter wavelengths in a relatively complex laser setup. To solve this problem, a mainly neglected fiber laser based on a Thulium:Holmium-codoped fiber (THF) is investigated. The advantages and disadvantages of this type of fiber are presented. Further parts of the work investigate the potential of novel codoped fibers.

**Chapter 2** provides the theoretical basics for the experimental work conducted in this thesis. This chapter is thematically divided into two. Firstly, the theory of fiber lasers is explained, focusing on various laser concepts and active laser ions, the laser principle, and Q-switching. Secondly, the fundamentals of nonlinear optics and frequency conversion are presented. These are essential for the realization of an optical parametric oscillator (OPO), which converts the pulsed 2  $\mu\text{m}$  radiation into the mid-IR (3–5  $\mu\text{m}$ ). Understanding the principles of nonlinear processes, including the effects of insufficient phase matching, is critical for achieving efficient frequency conversion. The requirements for efficient phase matching directly influence the design of the fiber laser to obtain certain optical properties.

Successful power scaling is accomplished based on a free-space laser setup, which has proven to work efficiently in a low-power regime. **Chapter 3** introduces the initial laser setup and explains critical preconditions for high-power operation. The chapter contains all optimization steps carried out during the thesis. The weaknesses and problems of the laser system are analyzed, and possible solutions and optimization approaches are explained. Especially the chromatic aberration of pump and signal radiation, coupled via one lens into the active fiber, has been identified as a significant challenge. This led to a strong degradation of the laser performance for many reasons, but it has been resolved by working with non-collimated pump radiation. In addition, proper fiber end confectioning using fiber end caps is investigated as a practical component to increase the laser damage threshold at the fiber end face.



The issues encountered when directly splicing an active fiber to an end cap and the unusual incoupling of the pump radiation are explained. Different methods for establishing a stable fiber to end cap connection, which does not impair the laser radiation, are introduced. All optimizations are subject to the premise of a compact laser setup.

**Chapter 4** presents the first experimental results in continuous-wave operation. In the beginning, various tunable lasers are realized using a diffraction grating. Based on the measured laser performance for different fiber lengths, a spectral emission range is determined where a successful power scaling can be accomplished. Subsequently, an actual power scaling of the fiber laser is performed, with the diffraction grating replaced by a narrow band volume Bragg grating for a more stable laser operation. Essential optical laser characteristics such as the laser beam quality, long-term power stability, and the laser emission spectrum are investigated. The initial and laser results obtained after a complete setup optimization are compared. By this, the effects of the setup optimization are directly observable.

**Chapter 5** focuses on the realization of various Q-switched fiber lasers, covering a wavelength region from 2.05 to 2.2  $\mu\text{m}$ . The chapter investigates the influence of different laser components on the laser performance. Based on the knowledge gained, an optimized Q-switched laser source will be addressed in Chapter 6, targeting nonlinear frequency conversion.

**Chapter 6** contains the initially intended experiments for building and investigating a Q-switched Tm:Ho-codoped fiber laser, which serves as the pump source for an optical parametric oscillator (OPO) based on the nonlinear material Zinc Germanium Phosphide (ZGP). Firstly, the phase-matching angle and the spectral pump acceptance bandwidth of ZGP are calculated. Subsequently, the setup of the linear OPO is introduced, and the optical characteristics of a revised Q-switched pump source, which relies on the findings of Chapter 5, are presented. Finally, OPO experiments are performed.

**Chapter 7** summarizes the conducted work and gives an outlook for possible improvements.

The scientific findings and results demonstrate that Tm:Ho-codoped fibers can serve as a basis for efficient and compact power scaling in a wavelength region traditionally dedicated to holmium-doped fibers. This opens up new possibilities for generating and power scaling laser radiation in the 2  $\mu\text{m}$  region and highlights that the rarely used and underestimated codoped fiber can play a more significant role within this scientific area besides the commonly used singly doped thulium and holmium fibers.

Notably, the extreme wavelengths up to  $2.2\mu\text{m}$  can be generated, resulting in a remarkable increase in current power values by a factor of 15. The power records, efficiencies, and emission ranges of state-of-the-art THF lasers have been surpassed completely. New records have been set regarding fiber-laser-pumped nonlinear conversion via ZGP OPOs.

# Acknowledgements

At the end of my doctoral thesis, it is important for me to express my gratitude to all the people who made this work possible and accompanied me on this phase of my life. I apologize for not being able to mention everyone by name, and if anyone feels overlooked, please accept my sincerest apologies. Besides the scientific work, assisting in establishing two research groups at different locations (one at the Karlsruhe Institute of Technology and one at Fraunhofer IOSB in Ettlingen) also consumed a significant amount of my time. Without the latter, conducting this doctoral thesis would not have been possible, making it essential for me to thank all those who supported me and our research group.

First and foremost, I would like to thank Prof. Eichhorn and Dr. Kieleck for providing me with the opportunity to conduct this exciting research under their guidance for my doctoral thesis. I am grateful for the time they devoted to me and for investing in my development. Their extensive knowledge has been invaluable to me throughout.

I would also like to extend my thanks to my fellow doctoral students and direct colleagues from the LAS and IRS-Optronics working groups, who have been with me throughout these past years. Special thanks goes to Steffen Güntert for our routine morning coffees and his time and open ear, which have been a great support over the years. I would like to express my gratitude to our simulator, Marius Rupp, who was a perfect office colleague. He generously took the time to proofread my entire doctoral thesis. Additionally, I want to thank Dr. Clement Romano, who possesses a lot of knowledge in optical fibers and fiber lasers. I greatly benefited. In addition, I want to thank Julian Schneider, Dominik Lorenz, and Dieter Panitzek for the time in the lab; and fruitful discussions on the topics of fiber lasers, splicing, and OPOs.

I also want to take the opportunity to thank Artur Schander and the mechanical workshop of the Fraunhofer IOSB. Without their excellent and highly precise work in the production of mechanics, the work in the laboratory would not have been possible.

A successful start at IOSB in Ettlingen would not have been possible without the active assistance of other departments (both scientific and administrative). I want to express my thanks for their support, especially to members of the optronics working group. Besides providing access to technical equipment in the chemistry laboratory and the OpticStudio simulation software, they lent me optics and devices that we urgently needed but did not possess at the time. Here, I would like to extend my gratitude to Bastian Schwarz, who showed me everything necessary at IOSB in the beginning and introduced me to the IOSB sports activities as a much-needed break from long hours in the lab. To keep this acknowledgement brief, I cannot individually thank everyone, but I would like to express a general thank you to all.

In addition, I would like to thank the doctoral students and staff members of the former group of Prof. Trommer who welcomed me at the university. Despite my infrequent presence at KIT, they always provided me with the best support. I want to mention Armin Teltschik, Andrea Bindschädel, and the mechanical workshop team as representatives of those I would like to thank.

Lastly, I want to express my gratitude to my family and friends. Without these anchors, the immensely intense and demanding period would have been much harder for me to endure. I especially want to thank my parents, Gabriele and Rainer Forster, who have supported me not only during my doctoral thesis but throughout my entire life. I am deeply grateful to my girlfriend, Marlene Haider, who stood by my side during these past years, despite the greater distance between us.

# Contents

<b>Zusammenfassung</b> . . . . .	<b>i</b>
<b>Abstract</b> . . . . .	<b>v</b>
<b>Acknowledgements</b> . . . . .	<b>ix</b>
<b>List of Abbreviations</b> . . . . .	<b>xv</b>
<b>1 Introduction</b> . . . . .	<b>1</b>
<b>2 Theoretical Background</b> . . . . .	<b>7</b>
2.1 Fiber Lasers . . . . .	8
2.1.1 Light Guidance in Optical Fibers . . . . .	8
2.1.2 Laser Principle . . . . .	13
2.1.3 Rare-Earth Dopants Thulium and Holmium in Silica Glass Fibers . . . . .	20
2.1.4 Q-Switching Theory . . . . .	26
2.2 Nonlinear Frequency Conversion . . . . .	31
2.2.1 Nonlinear Polarization . . . . .	31
2.2.2 $\chi^{(2)}$ -Nonlinearities and Optical Parametric Generation . . . . .	32
2.2.3 Birefringent Phase Matching . . . . .	37
2.2.4 Quasi-Phase-Matching . . . . .	38
2.2.5 Optical Parametric Oscillator . . . . .	40

<b>3</b>	<b>Laser Setup and Optimization for High-Power Laser Operation</b>	<b>43</b>
3.1	Fiber Architecture and Setup Scheme	45
3.1.1	Fiber Architecture	45
3.1.2	Setup Scheme	47
3.2	Fiber End Face Preparation	48
3.2.1	Theory of Fiber End Caps	48
3.2.2	Splicing of Fiber End Caps	51
3.2.3	End Cap Optimization	55
3.3	Pump and Signal - Fiber Coupling	58
3.3.1	Coupling Issues due to Chromatic Abberations	58
3.3.2	Impacts of Non-Correct Fiber Coupling	61
3.3.3	Methods for Improved Fiber Coupling	63
<b>4</b>	<b>Continuous-Wave Laser Operation</b>	<b>67</b>
4.1	Broadly Tunable Laser Source	67
4.1.1	Laser-Setup	68
4.1.2	Experimental Results	70
4.1.3	Discussion	77
4.2	Stable Power Scaling for Fixed Wavelengths	78
4.2.1	Review of Relevant State-of-the-Art Lasers	78
4.2.2	Laser-Setup	80
4.2.3	First experimental results below 2090 nm	83
4.2.4	Experimental Results at 2100 nm	86
4.2.5	Experimental Results at 2200 nm	89
4.2.6	All-fiber Laser Realization at 2120 nm	92
4.2.7	Discussion	95
<b>5</b>	<b>Q-Switched Laser Operation</b>	<b>97</b>
5.1	State-of-the-Art Nanosecond Pulsed Systems	98
5.2	Setup for Q-Switched Laser Operation	102
5.3	Q-Switching Results at 2050 nm	104
5.4	Q-Switching Results at 2090 nm	107
5.5	Q-Switching Results at 2130 nm	112
5.6	Q-Switching Results at 2200 nm	115
5.7	Conclusion	117

<b>6 Nonlinear Frequency Conversion by a Q-Switched</b>	
<b>THTF-laser-pumped ZGP OPO</b>	<b>119</b>
6.1 Zinc Germanium Phosphide - ZGP	119
6.2 Overview of 2 $\mu\text{m}$ -Fiber-Pumped ZGP OPOs	123
6.3 Pump Source and OPO Setup	126
6.4 Pump Source Performance	129
6.5 OPO Results	131
6.6 Summary and Conclusion	137
<b>7 Conclusion and Outlook</b>	<b>139</b>
7.1 Conclusion	139
7.2 Outlook	141
<b>Bibliography</b>	<b>143</b>
<b>List of Publications</b>	<b>159</b>





# List of Abbreviations

<b>AOM</b>	acousto-optic modulator
<b>ASE</b>	amplified spontaneous emission
<b>CSP</b>	cadmium silicon phosphide
<b>CR</b>	cross-relaxation
<b>CW</b>	continuous-wave
<b>DCF</b>	double-clad fiber
<b>DFG</b>	difference frequency generation
<b>DG</b>	diffraction grating
<b>EDF</b>	Er <sup>3+</sup> -doped fiber
<b>ETU</b>	energy transfer upconversion
<b>FBG</b>	fiber Bragg grating
<b>FTES</b>	fiber to end cap splice
<b>FWHM</b>	full width at half maximum
<b>HDF</b>	Ho <sup>3+</sup> -doped fiber
<b>HR</b>	high reflector
<b>IC</b>	input coupler
<b>LCF</b>	large core fiber
<b>LMA</b>	large mode area
<b>LR</b>	low reflector
<b>MCF</b>	multi-clad fiber
<b>MWIR</b>	mid-wave infrared
<b>MI</b>	modulation instabilities

<b>MMF</b>	multi-mode fiber
<b>MOPA</b>	master oscillator power amplifier
<b>NA</b>	numerical aperture
<b>OC</b>	output coupler
<b>OP-GaAs</b>	orientation-patterned gallium arsenide
<b>OP-GaP</b>	orientation-patterned gallium phosphide
<b>OPG</b>	optical parametric generation
<b>OPO</b>	optical parametric oscillator
<b>QPM</b>	quasi-phase-matching
<b>PANDA</b>	polarization-maintaining and absorption reducing
<b>PCF</b>	photonic crystal fiber
<b>PMF</b>	polarization-maintaining fiber
<b>RR</b>	repetition rate
<b>SPM</b>	self-phase modulation
<b>SMF</b>	single-mode fiber
<b>TCF</b>	triple-clad fiber
<b>TDF</b>	Tm <sup>3+</sup> -doped fiber
<b>TIR</b>	total internal reflection
<b>THF</b>	Tm <sup>3+</sup> :Ho <sup>3+</sup> -codoped fiber
<b>THTF</b>	Tm <sup>3+</sup> :Ho <sup>3+</sup> -codoped triple-clad fiber
<b>VBG</b>	volume Bragg grating
<b>YDF</b>	Yb <sup>3+</sup> -doped fiber
<b>ZGP</b>	zinc germanium phosphide

# 1 Introduction

Since the first experimental realization of a flashlight-pumped ruby laser by Theodore Maiman in 1960 [1], the history of the laser has become a success story. Next to such solid-state lasers, various laser types have been developed. Among others, fiber lasers and amplifiers have become indispensable tools in today's society, taking on essential tasks in various applications. Optical radiation of high spectral and spatial brightness, excellent beam quality in a high-power regime, and efficient cooling properties due to a large surface-to-volume ratio are some of the driving considerations to use fiber lasers [2–4]. These outstanding properties and the possibility of realizing rugged and compact all-fiber laser systems make them highly beneficial laser sources [5]. The main laser active gain media classes are rare-earth ions [6], which are doped into the core of the optical fiber. Since their first realization in the 1990s, various fiber lasers based on rare-earth ions have been developed, offering a broad spectrum of possible operating wavelengths [7].

Some of the most investigated rare-earth-doped fiber lasers are ytterbium ( $\text{Yb}^{3+}$ )-doped lasers emitting at 1  $\mu\text{m}$ . The high output powers, which rely on a high slope efficiency and the possibility of in-band diode pumping [6, 8], make them ideal sources for industrial cutting and welding of metals [9]. Besides ytterbium, erbium ( $\text{Er}^{3+}$ )-doped lasers and amplifiers play an essential role in today's everyday life [6, 10]. Among others, the emission wavelength of 1.5  $\mu\text{m}$  builds the backbone for the optical communication branch due to a transmission maximum in optical silica fibers. In contrast to  $\text{Yb}^{3+}$ -doped fibers (YDFs), no suitable high-power diode lasers are available. Therefore, as one option, YDF lasers are used as pump sources. As an alternative to this tandem pumping scheme, a codoped architecture of a  $\text{Yb}^{3+}$ -sensitized  $\text{Er}^{3+}$ -doped fiber (EDF) has shown simple, compact, and efficient lasers [11]. An energy transfer between the two rare-earth ions enables an indirect excitation of the erbium ion lasing level. Both aforementioned wavelength regions, 1  $\mu\text{m}$  and 1.5  $\mu\text{m}$ , are well investigated with an existing wide selection of commercially available optics and components.

A third wavelength region with laser output powers of several hundreds of watts is currently established at  $2\ \mu\text{m}$  [12]. Thereby thulium ( $\text{Tm}^{3+}$ )-doped fiber lasers are the driving force [13]. Due to high-power diode lasers at  $79\text{X}\ \text{nm}$  combined with an advantageous cross-relaxation process, kW-level single-mode output has already been demonstrated [14–16]. Strong  $2\ \mu\text{m}$  absorption features of water and plastics make them an ideal source for a variety of medical applications (prostate ablation, destruction of kidney and bladder stones) and additive-free material processing [17, 18].

Especially, continuous-wave (CW) and pulsed laser sources emitting at a wavelength of  $2.09\ \mu\text{m}$  and above gain more and more interest. The existence of a broad atmospheric transmission window [19] (depicted in Fig. 1.1) in combination with a more retina-safe nature of wavelengths  $> 1.4\ \mu\text{m}$  [20] makes these wavelengths perfectly suitable for applications like remote sensing and free-space optical communication. Moreover, nanosecond pulsed laser sources emitting  $\geq 2.09\ \mu\text{m}$  are excellent pump sources for nonlinear frequency conversion into the mid-IR, e.g., by optical parametric oscillators (OPOs) based on nonlinear materials like zinc germanium phosphide (ZGP) [21] or orientation-patterned gallium arsenide (OP-GaAs) [22]. The absence of suitable direct laser sources makes generating high-power mid-IR radiation challenging.

OPO spectrum on both sides of the degenerated signal and idler wavelength of  $4.2\ \mu\text{m}$   
 $\text{Tm}^{3+}:\text{Ho}^{3+}$  emission spectrum

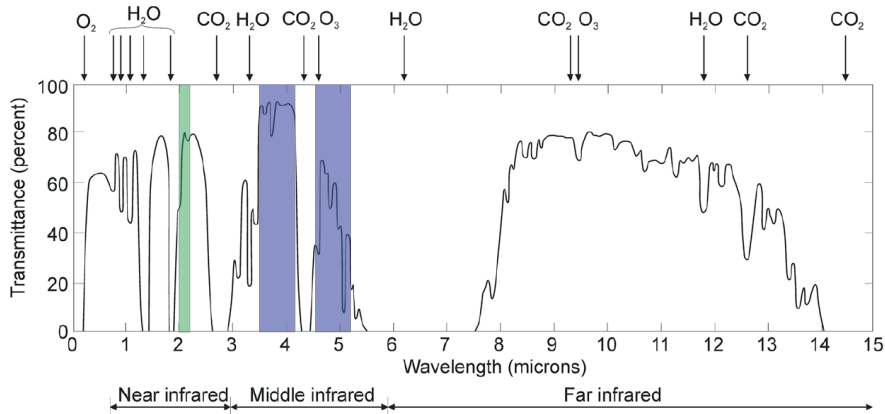


Figure 1.1: Atmospheric transmission in percentage plotted versus the wavelength. The typical wavelength range of  $\text{Tm}^{3+}:\text{Ho}^{3+}$ -codoped fiber (THF) lasers (marked in green) and  $2\ \mu\text{m}$ -pumped mid-IR optical parametric oscillators (marked in blue) are included. The graph is taken from [23] and is modified.

However, nonlinear frequency conversion offers a suitable solution to address the spectral range from 3 to 5  $\mu\text{m}$ . Typical utilized nonlinear crystals show strong absorption features up to  $\sim 2 \mu\text{m}$  [24]. Therefore, pump radiation with a slightly longer wavelength than 2  $\mu\text{m}$  minimizes the absorption, thereby reduces the thermal effects and allows a successful average power scaling. In addition, pump wavelengths at around 2.1  $\mu\text{m}$  intrinsically generate mid-IR signal and idler wavelengths above and below a strong absorption feature of the  $\text{CO}_2$  molecule at 4.2  $\mu\text{m}$ , which helps to avoid operating the OPO at this detrimental wavelength. The absorption coefficients of ZGP and OP-GaAs are shown in Fig. 1.2, and the OPO's mid-IR emission spectrum is highlighted in blue in Fig. 1.1.

$\text{Tm}^{3+}$ -doped fiber (TDF) lasers are unsuitable for operating at these relatively long wavelengths due to strongly decreasing emission cross sections [25], which leads to a small gain [13, 26]. This small gain, in combination with a tremendously high gain at wavelengths between 1.9  $\mu\text{m}$  and 2.0  $\mu\text{m}$ , makes it challenging to achieve a stable laser operation at longer wavelengths since shorter wavelength operation can hardly be suppressed.

Besides thulium, holmium ( $\text{Ho}^{3+}$ ) ions show strong emission cross sections at 2  $\mu\text{m}$  and especially in the targeted wavelength region  $\geq 2.09 \mu\text{m}$  [27, 28]. In contrast to TDF lasers, there are no suitable high-power diode lasers for pumping  $\text{Ho}^{3+}$ -doped fiber (HDF) lasers. Therefore, TDF lasers are typically used to in-band pump HDF lasers [27].

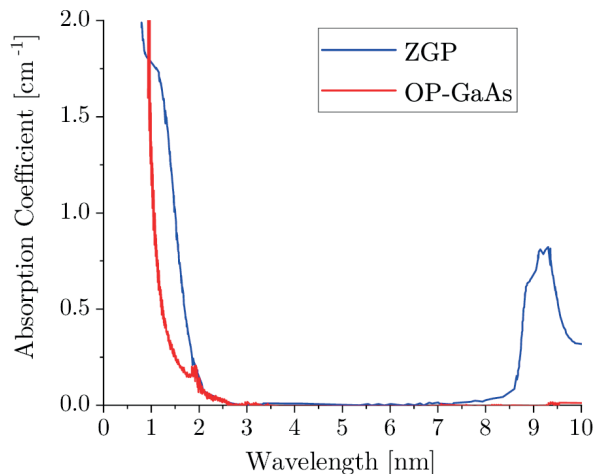


Figure 1.2: Absorption coefficients of the nonlinear media ZGP and OP-GaAs. The graph shows that long-wavelength 2  $\mu\text{m}$  radiation can help decrease the absorption inside the crystals and prevent detrimental thermal effects for power scaling. The absorption data is taken from [24].

This leads to more complex setups. Despite this circumstance, HDF lasers are promising sources with theoretical slope efficiencies  $> 90\%$ . In reality, these lasers only achieve efficiencies up to 50 to 60% for systems with higher output power and with a maximum of 400 W [29, 30]. This inefficient laser operation is attributed to ion-clustering of holmium ions leading to pair-induced quenching [31, 32]. At high holmium concentrations, which are needed for an efficient laser operation, the holmium ions are prone to cluster in the core of the active fiber. A too short distance between the ions leads to an effective de-excitation of the upper laser level. This effect hinders the power scaling of HDF lasers and has been effectively preventing the use and research on this type of fiber on a large scale.

As for the  $\text{Er}^{3+}:\text{Yb}^{3+}$ -doped fibers, HDFs can be sensitized with thulium ions to enable an indirect 79X nm diode-pumping via an energy transfer from thulium to holmium [33]. The codoped fiber can be crucial for a compact setup with reduced complexity while showing reasonable efficiencies. However, THFs are barely used, produced, sold, and even investigated. Especially for power scaling in the wavelength region  $\geq 2.09\ \mu\text{m}$ , where THFs should be designed to operate, they are almost entirely omitted. Earlier publications have shown that optimizing the codoped fiber for an efficient cross-relaxation (CR) increases another detrimental ion-ion interaction [34]. This process, called energy transfer upconversion (ETU), leads to a lifetime quenching of the upper laser levels of thulium and holmium and an increase of the thermal load inside the fiber core. Also, when an ideal CR and energy transfer are considered, the thermal load combines the one from the separate thulium and holmium systems. This discourages the use of THFs. However, recent investigations have shown that efficiencies of up to 56% are possible at a wavelength of 2.1  $\mu\text{m}$  [35], most likely related to improvements in the manufacturing process of optical fibers. Considering the currently limited performance of HDF lasers, establishing such efficiencies in a high power THF laser setup can make THF lasers a serious competitor.

This thesis aims to investigate THF lasers for a laser operation in CW and nanosecond pulsed regime with a particular focus on emission wavelengths  $\geq 2.09\ \mu\text{m}$ . Output power, average output power, and pulse energy scaling are of primary interest while achieving excellent optical characteristics like good beam quality and a narrow emission spectrum. The primary references to compare with are state-of-the-art THF lasers and holmium systems. This gives an overview of the opportunities and the best strategies for power scaling laser radiation  $\geq 2.09\ \mu\text{m}$ . Special focus is put on the realization of complexity-reduced and compact free-space setups. Based on the findings of this thesis, the next step will be to develop more integrated laser setups.

An optimized Q-switched THF laser is used to pump an OPO based on the nonlinear material ZGP and improve current systems in terms of mid-IR output power. This can be seen as quantifying the setup improvements and the realized pulsed laser itself. The structure of the thesis is as follows:

The theoretical background is introduced at the beginning of the thesis to get a basic understanding of essential physics and concepts. The first part of Chapter 2 explains the laser principle for CW and Q-switched operation. In addition, important fiber concepts like waveguiding and different fiber geometries are discussed. The second part introduces the fundamentals of nonlinear optics and OPOs with a special focus on phase matching as an essential concept and technique for an efficient nonlinear process.

The free-space laser setup under investigation evolved from an earlier one, which was only used so far in a low-power regime. Chapter 3 treats the critical investigations and improvements, which have been done, related to the setup to ensure a stable power scaling.

First experimental results in CW operation, summarized in Chapter 4, investigate the possibility of laser operation up to an emission wavelength of 2.2  $\mu\text{m}$  and even beyond. Tunable and fixed emission wavelength laser setups are realized.

Chapter 5 contains the results for the Q-switched operation of the THF laser setup. The influence of fiber length and additional different cavity parameters are investigated.

The knowledge gained on the Q-switched fiber lasers is used to realize an optimized pulsed laser for nonlinear frequency conversion. This optimized pulsed laser source is used to pump a ZGP OPO. The results are presented in Chapter 6.

Chapter 7 summarizes the findings and results of this thesis and gives an outlook on further improvements and investigations.





## 2 Theoretical Background

This chapter intends to lay the theoretical fundamentals to understand the experimental work performed within this thesis and to give some elementary basics for rare-earth-doped fiber lasers and nonlinear frequency conversion via optical parametric oscillation. The theory part is not intended to give an extensive derivation and summary but to give a general idea of different concepts. Primary literature covering each aspect is referenced at the according parts within the chapter. The beginning of Section 2.1 focuses on describing optical fibers. Afterward, the laser principle is described, followed by the characteristics of the active laser media thulium and holmium. Both can build the basis for laser operation at around  $2\ \mu\text{m}$ . The fiber theory section is completed by the concept of Q-switching used to generate pulsed laser radiation in the nanosecond regime. At the beginning of Section 2.2, the origin of the nonlinear polarization as a source term for new frequency components is explained. After that, second-order nonlinearities are described with a particular focus on optical parametric generation (OPG) as the fundamental process for optical parametric oscillation. Then, the general concept of phase matching is discussed, showing its importance for an efficient frequency conversion. In the end, OPOs are introduced as nonlinear frequency converters.

## 2.1 Fiber Lasers

### 2.1.1 Light Guidance in Optical Fibers

Fundamental to the importance of optical fibers in today's society and for fiber lasers is their guiding property for optical radiation. It can be distinguished between conventional "index-guiding" [36] and guiding based on the photonic band-gap effect [37]. In this work, index-guiding fibers are used, and therefore, the theoretical background on photonic band-gap fibers is not included.

In the most simple case, optical guidance takes place in a glass rod with refractive index  $n_1$ , which is surrounded by air, having a lower refractive index  $n_{air}$ . However, this configuration is neither mechanically nor optically stable due to environmental influences altering the optical properties. Therefore, an optical fiber consists of a core with refractive index  $n_{co}$ , which is surrounded by a cladding of refractive index  $n_{cl}$ . Typically, both layers consist of glass. A polymer coating covers the cladding to increase the mechanical stability. Depending on the size of the core and cladding, the wavelength of the propagating light, and the refractive index difference  $\Delta n = n_{co} - n_{cl}$ , the fibers can be subdivided, among other criteria, into single- or few-mode fibers and multi-mode fibers. The waveguiding properties of these two optical fiber types are described by different regimes, which are explained in the following two sections. [36]

#### 2.1.1.1 Ray Optics Approach for Multi-Mode Fibers

In the case of a true multi-mode fiber (MMF), hundreds of modes propagate through the fiber. The wavelength of the guided light is much smaller than the core diameter ( $\lambda \ll 2r_{co}$ ). Therefore, the light guidance in these optical fibers can be described using geometrical optics and the principle of total internal reflection (TIR). Within this regime, the modes are simplified as rays, representing the normal vector of the electric field's phase front. Snell's law of refraction

$$n_{co} \sin(\alpha_{co,1}) = n_{cl} \sin(\alpha_{cl}) \quad (2.1)$$

describes the behavior of light rays propagating toward an interface of two transmissive dielectric materials with different optical densities. This principle can be applied to the interface of fiber core and fiber cladding.

In the case of  $n_{co} > n_{cl}$ , light rays within the core, which fulfill the criterion of TIR, remain in the core and are no longer refracted into the cladding ( $\alpha_{cl} = 90^\circ$ ). This applies to rays, which propagate through the core with an angle of  $\alpha_{co,1} \geq \alpha_{tot} = \arcsin(n_{cl}/n_{co})$ . Figure 2.1 shows a simple scheme of a multi-mode fiber with a typical step-index profile. It illustrates a light ray passing through the fiber core and the resulting acceptance cone, which contains all rays outside the fiber that the fiber core can guide. A typical fiber parameter, which can be directly derived from the angle of TIR, is the numerical aperture (NA)

$$NA = n_{co} \sin(\alpha_{co}) = n_{air} \sin(\alpha_{air}) = \sqrt{n_{co}^2 - n_{cl}^2} \quad (2.2)$$

of the fiber ( $\alpha_{co,1} + \alpha_{co} = 90^\circ$ ). The NA describes the largest angle  $\theta_{air}$ , which can be launched into the fiber and still will be guided by TIR. Typical values for the NA of multi-mode radiation used in this thesis are 0.22 and 0.46, resulting in an acceptance angle within the air ( $n_{air} \sim 1$ ) of  $12.7^\circ$  and  $27.4^\circ$ , respectively. The 3-dimensional equivalent of the acceptance angle is the acceptance cone. For good light incoupling into the fiber, the acceptance cone must not be overfilled to avoid radiation loss. The NA, representing the index difference between core and cladding, is one of the essential parameters in fiber design, defining the optical characteristics of the fiber. [38, 39]

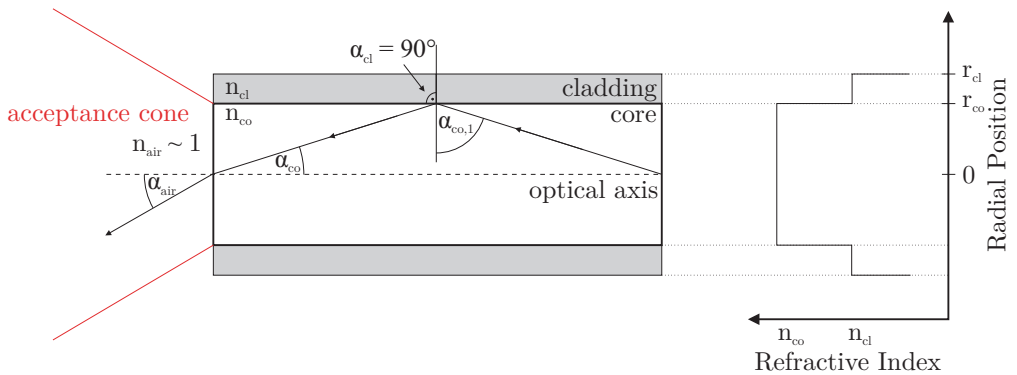


Figure 2.1: Schematic of a MMF, which illustrates the theory of light guiding using ray optics.

### 2.1.1.2 Exact Fiber Solutions for Single-Mode and Few-Mode Fibers

For a single-mode fiber (SMF) or a few-mode fiber,  $\lambda \ll 2r_{co}$  does no longer hold, and the wavelength of propagation is within the order of the core dimensions ( $\lambda \approx 2r_{co}$ ). A schematic of a SMF is depicted in Fig. 2.2. Maxwell's equations need to be solved explicitly to describe the light guidance within this regime. The theory treated within Section 2.1.1.2 is based on [40, 41]. The problem is reduced to find the solution to the Helmholtz equation for a cylindrical dielectric waveguide. Taking advantage of the axial symmetry of the problem, the scalar Helmholtz equation can be expressed in cylindrical coordinates (radius  $\rho$ , angular coordinate  $\phi$ , and axial position  $z$ ):

$$\Delta\Psi = \left( \frac{1}{\rho} \partial_\rho (\rho \partial_\rho) + \frac{1}{\rho^2} \partial_\phi^2 + \partial_z^2 \right) \Psi = -n^2(\omega) k_0^2 \Psi \quad (2.3)$$

$\Psi$  is representative for each field component  $E_i$  and  $H_i$  with  $i \in \{\rho, \phi, z\}$ . Knowing two electric field components, e.g.,  $E_z$  and  $H_z$ , the other four can be composed. In order to solve this partial differential equation, the method of separation of variables can be utilized by using the ansatz  $\Psi = R(\rho)\Phi(\phi)Z(z)$ . This leads to two linear ordinary differential equations of second order

$$\beta^2 Z(z) = -\partial_z^2 Z \quad (2.4)$$

$$\nu^2 \Phi = -\partial_\phi^2 \Phi \quad (2.5)$$

and a well-known differential equation for Bessel functions

$$\frac{1}{\rho} \partial_\rho (\rho \partial_\rho) R + \left( n^2(\omega) k_0^2 - \beta^2 - \frac{\nu^2}{\rho^2} \right) R = 0. \quad (2.6)$$

$\nu$  is an integer number and  $\beta$  is the modal propagation constant. The differential equation needs to be solved for the core ( $n = n_{co}$ ) and the cladding ( $n = n_{cl}$ ) separately. The solutions need to fulfill the boundary conditions at the core-cladding interface. This leads to an eigenvalue equation for the propagation constant  $\beta$ , determining all optical characteristics of the propagating mode. Analyzing this eigenvalue equation shows that only discrete values  $\beta_{\nu m}$  exist, where  $m$  is an integer for the number of roots of the Bessel function. The exact solution to this differential equation yields the transverse electric  $TE_{\nu m}$  and transverse magnetic  $TM_{\nu m}$  modes and the hybrid modes  $HE_{\nu m}$  and  $EH_{\nu m}$ .

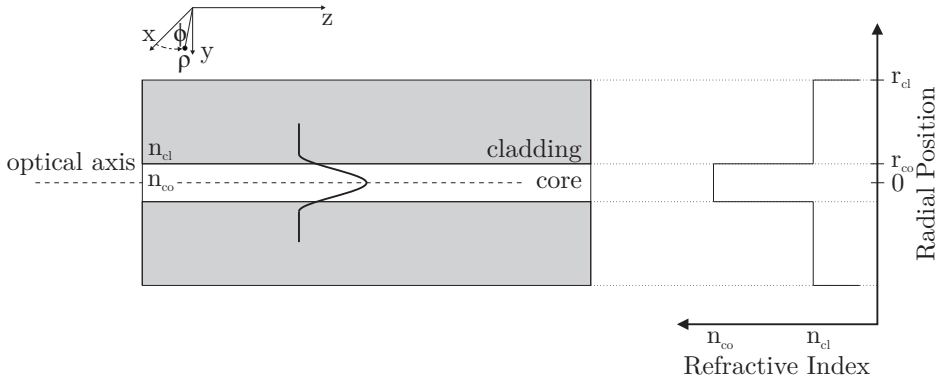


Figure 2.2: Schematic of a SMF, which illustrates the theory of light guiding using wave optics.

The eigenvalue equation can be simplified by assuming a weak guiding with  $n_{co} \approx n_{cl}$ . These solutions are linearly polarized modes, so-called  $LP_{\nu m}$ . Each of these modes is doubly degenerate due to two orthogonal linear polarization. Usually, these modes are considered in good approximation, dealing with single- or few-mode optical fibers. Figure 2.3 shows three modes for different  $\nu$  and  $m$ . The fundamental mode with  $\nu = 0$  and  $m = 1$  looks similar to a Gaussian beam. [40, 41]

An important parameter for the fiber design of single- and few-mode fibers is the number of modes guided in the core. Therefore, the normalized frequency  $V$  can be introduced as a waveguide parameter. For a normalized frequency  $V$  smaller than 2.405, only the fundamental mode  $LP_{01}$  is supported by the waveguide. [40, 41]

$$V = \frac{2\pi r_{co}}{\lambda} \sqrt{n_{co} - n_{cl}} \leq 2.405. \quad (2.7)$$

The fundamental mode does not exhibit a perfect beam quality due to a slight deviation compared to a Gaussian beam [42] but shows an excellent beam quality for practical uses.

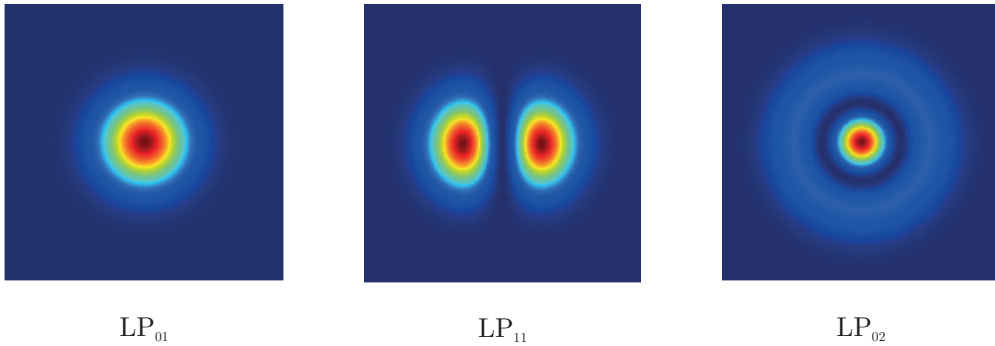


Figure 2.3: Intensity distributions for various linearly polarized (LP) modes as eigenvalue solutions of an optical fiber in a weakly guiding regime.

### 2.1.1.3 Relevant Fiber Types - I (Passive Fibers)

Within this thesis,  $\text{Tm}^{3+}:\text{Ho}^{3+}$ -codoped polarization-maintaining triple-clad silica fibers are investigated, which combine many different fiber concepts resulting in a unique  $\text{Tm}^{3+}:\text{Ho}^{3+}$ -fiber geometry. These fiber concepts are introduced in two steps. Figure 2.4 shows the comparison of three different concepts implemented for passive fibers but not exclusively for passive fibers. The two fundamental fiber concepts **SMF** and **MMF** are already introduced in the previous sections.

Based on Eq. (2.7), SMFs are designed to support only one mode and deliver high-quality laser radiation, which means high spatial brightness. MMFs can be used for a more flexible coupling of signal into a fiber and for transporting high-power, highly multi-mode laser radiation. In this thesis, the pump radiation is delivered by MMFs from the diodes to the place of use in the setup. Another important fiber concept is a **polarization-maintaining fiber (PMF)** [43]. Various applications require linearly polarized light and the opportunity to deliver this light within a fiber without altering the polarization state. Typically, an LP mode is doubly degenerated due to two orthogonal linear polarization states. These two modes have the same effective propagation constant. Even small macro-bendings of the fiber can lead to significant crosstalk between these modes and coupling from one mode to the other. To obtain a fiber conserving the linear polarization of the light, a birefringence is introduced into the fiber, e.g., by incorporating so-called stress rods into the cladding. Typically, they are made of boron-based glass and have a lower refractive index than the cladding to prevent a guiding effect inside the stress rods.

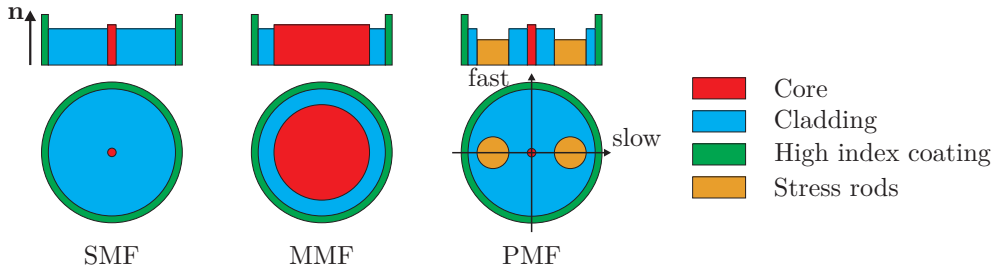


Figure 2.4: A comparative schematic of three fundamental concepts and geometries in fiber optics. Single-mode and multi-mode fibers describe two basic fiber regimes, delivering high- and low-brightness radiation. Polarization-maintaining fibers can deliver linearly polarized light by utilizing stress-induced birefringence, e.g., caused by incorporated stress rods.

Modes, which are polarized parallel to the stress rods, experience a higher effective refractive index compared to modes, which are polarized orthogonally to the stress rods. Therefore, the axis going through the stress rods is called the slow polarization axis, and the orthogonal one is called the fast polarization axis. Only linear polarization launched parallel to one of the two main axes will be preserved. In the case of rod-type stress-rods, as displayed in Fig. 2.4, the PMF is called a polarization-maintaining and absorption reducing (PANDA)-type fiber [44].

## 2.1.2 Laser Principle

Optical fibers build a good basis for high-power laser operation exhibiting a good beam quality, which is based on the combination of an efficient cooling due to a relatively large surface-to-volume ratio and its waveguiding effect [3, 4]. This subsection presents the fundamentals of CW laser operation. The content is inspired by [45–48] and can be advised for further information.

### 2.1.2.1 Light Amplification

The acronym **LASER** stands for **L**ight **A**mplification by **S**timulated **E**mission of **R**adiation and is named after the light-matter interaction responsible for the unique characteristics of its output emission [49].

Stimulated emission is one of three interaction mechanisms between light and matter, which has to be considered inside an active laser gain medium (in the case of this thesis, a rare-earth ion). In addition, absorption and spontaneous emission play a significant role. Figure 2.5 displays the energy scheme for the quantum mechanical processes spontaneous emission, stimulated emission, and absorption [38]. When the energy of a photon  $h\nu$  matches with the energy difference  $\Delta E$  between a lower populated energy level  $E_1$  and a higher unpopulated energy level  $E_2$  of an ion, an electron can be lifted into the upper energy level, whereas the photon will be annihilated. The ion remains in a metastable condition. This process is called absorption. Spontaneous emission describes the decay of an electron from an excited state  $E_2$  back into the ground state within a characteristic lifetime. A photon with the energy  $\Delta E$  is emitted during this statistical process. The direction and phase of the photon are arbitrary. Furthermore, when an electron is in an excited state, a resonant process can take place when a photon with matching energy induces the emission of a second photon, which is called stimulated emission. When the electron decays back into the ground state, a photon with the same optical characteristics as the initial photon is emitted. Therefore, light amplification can take place effectively, and light with well-defined properties is generated. [38]

The effective gain  $G(z,\lambda)$  for propagating through a laser-active medium is described by the spectral intensity  $I(z,\lambda)$  at position  $z$  within the medium divided by the incident spectral intensity  $I(0,\lambda)$  [45]:

$$G(z,\lambda) = \frac{I(z,\lambda)}{I(0,\lambda)} = e^{(\sigma_e(\lambda)N_2 - \sigma_a(\lambda)N_1)z}. \quad (2.8)$$

$N_1$  and  $N_2$  are the population densities in the energy level 1 and 2, respectively.  $\sigma_e(\lambda)$  is the wavelength-dependent emission cross section and  $\sigma_a(\lambda)$  is the wavelength-dependent absorption cross section.

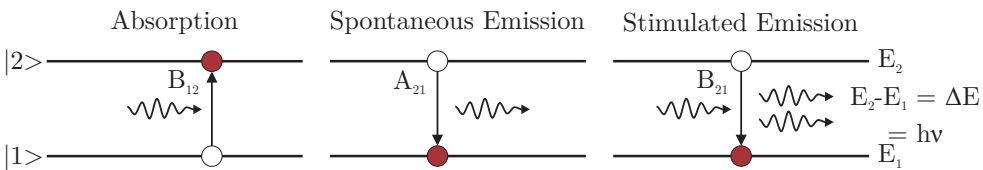


Figure 2.5: Fundamental interactions of light and matter described in a two-level system.



### 2.1.2.2 Population Inversion

For amplification of optical radiation,  $G > 1$  is required, leading to an effective population inversion

$$N_2 > \frac{\sigma_a(\lambda)}{\sigma_e(\lambda)} N_1. \quad (2.9)$$

For a single laser line in a strict two-level system, where the absorption cross section equals the emission cross section, the requirement can be simplified to create more ions in the excited state than in the ground state,  $N_2 > N_1$ .

In thermal equilibrium, where the Boltzmann distribution gives the population density relation between the two energy levels  $N_2/N_1 = \exp(-(h\nu)/(k_B T))$ , an inversion cannot be created. Moreover, it can be shown that for a strict two-level system, which is displayed in Fig. 2.5, no population inversion can be achieved. Stimulated emission and (stimulated) absorption are opposing processes, and in the best case, transparency can be reached. In addition, this symmetry is broken by spontaneous emission, so not even 50% excited ions can be reached. Therefore, more complex systems have to be used for modeling active laser media. However, the description of these gain media can be reduced to models of a three-level laser system, a four-level laser system, or a quasi-three-level laser system. [45]

For rare-earth-doped fiber lasers, the splitting of the laser levels into small subdivided energy levels (called manifolds) and their thermal population distribution lead to non-identical emission and absorption cross sections for the transition between two laser levels. Depending on the targeted emission wavelength within one transition between two manifolds, which can be addressed by different strategies (pump schemes, doping concentrations, fiber, and cavity architecture), the laser systems can be more of a three-level or four-level nature. Further information on the gain medium can be found in Section 2.1.3. [10]

### 2.1.2.3 Feedback for Laser Oscillation

With the knowledge gained so far, already first laser concepts can be discussed. Based on the processes and concepts of stimulated emission, amplification, and effective population inversion, a first idea of a laser can be realized. The basic structure of the single-oscillator fiber laser comprises three essential components, a laser-active gain medium, a pump source, and a resonator [48]. Figure 2.6 shows a simple fiber-related setup, only containing the fundamental parts.

First and most important, a laser-active medium is required to amplify the radiation by stimulated emission. The active gain medium is incorporated into the core of an optical fiber. Second, as already seen, a method is needed to create a population inversion. This mechanism is called pumping. Typically, optical radiation is used for fiber lasers to excite electrons from the ground state into the upper laser level. Third, after radiation amplification is possible, feedback is introduced to the gain medium to start the laser oscillation. The feedback is also termed a laser resonator or a laser cavity and has two mirrors, one at each end of the fiber. One mirror is called the high reflector (HR) and has a reflectance of close to 100%. The other mirror is used to outcouple the laser radiation and is, therefore, partially reflective. For fiber lasers, based on a high single-pass gain, output coupler (OC) reflectances from 3 to 10% are used. [45] Figure 2.6 can be used to calculate the amplification inside the fiber, which is needed to start the laser oscillation.

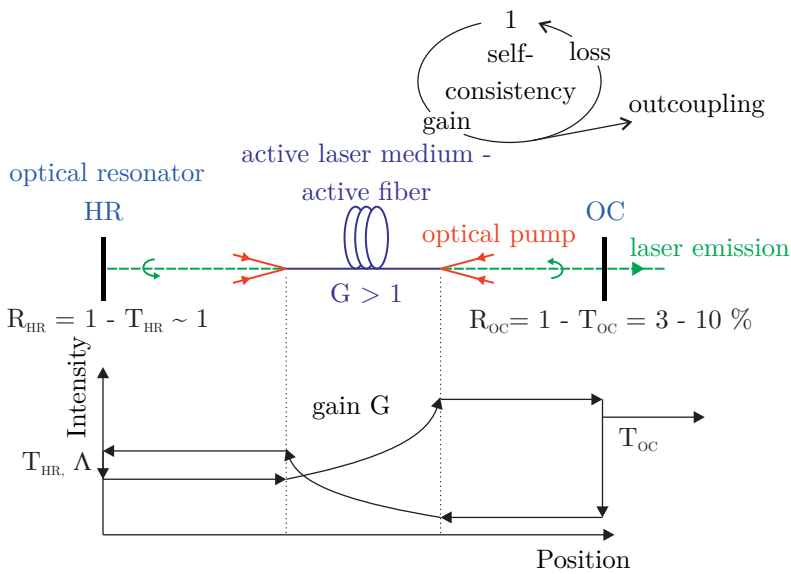


Figure 2.6: Fundamental concept for the realization of a single-oscillator fiber laser with essential components: a laser-active gain medium, an optical pumping mechanism, and a laser resonator. Self-consistency is required to reach the laser threshold and maintain the laser oscillation.

This threshold gain can be derived by requiring self-consistency for the internal laser intensity within one round-trip [45]:

$$R_{OC}G(1 - \Lambda_R)R_{HR}G \stackrel{!}{=} 1 \Rightarrow G = \frac{1}{\sqrt{R_{OC}(1 - \Lambda_R)R_{HR}}} \quad (2.10)$$

$\Lambda_R$  contains all residual losses for the signal, except for the transmission losses of the cavity mirrors.

#### 2.1.2.4 Continuous-Wave Laser Operation

This section contains important formulas for laser operation. They are taken from [45]. The precise derivation can also be found there.

Including Eq. (2.10) into the amplification (Eq. (2.8)) and lasing process extends the requirements for laser operation. The revised population density ratio reads as follows:

$$\frac{\langle N_2 \rangle}{\langle N_1 \rangle} = \frac{\sigma_a(\lambda_s)\langle N \rangle L + \ln G}{\sigma_e(\lambda_s)\langle N \rangle L - \ln G}. \quad (2.11)$$

$\langle \cdot \rangle$  describes the axial average since the photon field, the population densities, and hence the gain vary along the laser axis. Just a gain medium with an amplification  $G > 1$  (effective population inversion (Eq. (2.9))) is not enough for starting a laser operation, but the gain also has to compensate for the losses and the outcoupling. Increasing the outcoupling of the fiber laser results in an increase in threshold gain. In consequence, a higher population density ratio is required.

In the next step, the photon field density  $\Phi$  and the inversion  $\Delta N = N_2 - N_1$  must be calculated explicitly to get further information about the laser process. This set of equations can be used to describe the CW and the Q-switched laser operation later on. To dense the writing, new auxiliary variables  $\sigma_{\pm}(\lambda) = \sigma_a(\lambda) \pm \sigma_e(\lambda)$  are introduced. The set of coupled equations reads as [45]:

$$\partial_t \langle \Delta N \rangle = 2 \frac{\lambda_p}{hc} I_p \frac{\eta_{abs}}{L} + c(\sigma_-(\lambda_s)\langle \Phi N \rangle - \sigma_+(\lambda_s)\langle \Phi \Delta N \rangle) - \frac{\langle N \rangle + \langle \Delta N \rangle}{\tau}, \quad (2.12)$$

$$\partial_t \langle \Phi \rangle = \frac{c}{2} (\sigma_+(\lambda_s)\langle \Phi \Delta N \rangle - \sigma_-(\lambda_s)\langle \Phi N \rangle) - \frac{\langle \Phi \rangle}{\tau_c}. \quad (2.13)$$

Important parameters are the pump absorption efficiency  $\eta_{abs}(\langle\Delta N\rangle, \langle N\rangle)$  and the cavity photon lifetime  $\tau_c = nL/(c \cdot \ln G)$ .

To determine the laser behavior in dependence of the pump power, the Eqs. (2.12) and (2.13) are solved for the inversion  $\langle\Delta N\rangle$  and the laser output power  $P_s \propto \Phi$  in stationary operation ( $\partial_t\langle\Delta N\rangle = 0$  and  $\partial_t\langle\Phi\rangle = 0$ ). This leads to two sets of solutions, one set of solutions below the threshold pump power  $P_{th}$  (intensity  $I_{th}$ ) and one set of solutions above. For the solutions below threshold hold [45]:

$$\langle\Delta N\rangle = 2 \frac{\lambda_p}{hc} I_p \frac{\eta_{abs}}{L} - \langle N\rangle, \quad (2.14)$$

$$\langle\Phi\rangle = 0. \quad (2.15)$$

The average inversion and the laser output power in dependence on the pump power are depicted in Fig. 2.7. Below the threshold, the signal photon field density is constant and zero if one neglects fluorescence emission. The inversion is described by a transcendental equation since the absorption efficiency depends on the inversion itself. With increasing pump power, the inversion increases continuously, beginning with  $-\langle N\rangle$  when no pump power is applied. The inversion increases to the threshold condition, where the laser starts to oscillate. From here on, the inversion is clamped to a fixed value. Every additional pump power is not stored in the system in terms of excited electrons but converted to laser output power with a certain efficiency.

When the pump intensity reaches the threshold intensity, the second set of solutions for Eq. (2.12) and Eq. (2.13) becomes stable. These solutions read as follows [45]:

$$\langle\Delta N\rangle = \frac{2 \ln G}{\sigma_+(\lambda_s)L} + \frac{\sigma_-(\lambda_s)}{\sigma_+(\lambda_s)} \langle N\rangle, \quad (2.16)$$

$$\langle\Phi\rangle = \frac{\lambda_p}{hc^2} \frac{\eta_{abs}}{\ln G} (I_p - I_{th}). \quad (2.17)$$

As already mentioned, the inversion remains constant above the threshold. The photon field increases linearly with increasing pump intensity. The threshold intensity  $I_{th}$  and the corresponding saturation intensity  $I_{sat}^p$  are determined by the following equations [45]:

$$I_{th} = \frac{I_{sat}^p}{\eta_{abs}} (\ln G + \sigma_a(\lambda_s) \langle N\rangle L), \quad (2.18)$$

$$I_{sat}^p = \frac{hc}{\lambda_p \sigma_+(\lambda_s) \tau}. \quad (2.19)$$

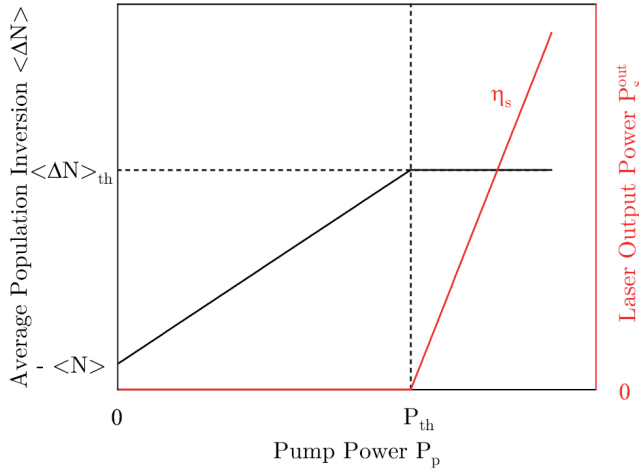


Figure 2.7: By solving the set of coupled equations regarding the population inversion  $\langle \Delta N \rangle$  and the photon field density  $\Phi$ , the population inversion  $\langle \Delta N \rangle$  and the laser output power  $P_s^{out}$  can be calculated in dependence of the pump power  $P_p$ . There are two sets of solutions, one below and one above threshold power  $P_{th}$ .

Equation (2.17) can be modified to be visualized in a way that typical power curves of laser oscillators are displayed. Here, the output power is written in dependence on the pump power [45]:

$$P_s^{out} = \underbrace{\frac{\lambda_p - \ln R_{OC}}{\lambda_s} \eta_{abs}}_{\text{slope efficiency } \eta_s} (P_p - P_{th}). \quad (2.20)$$

The pre-factor of Eq. (2.20) is called the slope efficiency  $\eta_s(R_{OC}, G, \eta_{abs})$ . For Eq. (2.20), the slope efficiency is limited by the quantum efficiency  $\eta_q = \lambda_p/\lambda_s$ . To establish an efficient laser operation and a power scalable laser system, the aim is to maximize the slope efficiency. The optimization process is not entirely trivial since a decrease in the reflectance of the output coupler leads to an increase in the gain and a modification of the absorption efficiency. However, the output coupler reflectance can be chosen as small for systems with high single-pass gain, like fiber lasers. This also helps to decrease the signal's intra-cavity intensity and avoids critical damage. However, a laser system tends to be much more complex. Ion-ion interactions can influence the actual slope efficiency both in a negative and in a positive way. A closer discussion of the ion-ion interactions will be given in the following section, which focuses on the active laser media under investigation.

### 2.1.3 Rare-Earth Dopants Thulium and Holmium in Silica Glass Fibers

Developing or buying a laser source comes with the idea of creating and using laser emission at a specific wavelength or within a specific wavelength range. In the case of solid-state lasers, this is equivalent to choosing a suitable laser active medium, providing the corresponding spectroscopic characteristics, and allowing for efficient stimulated emission. Most common gain media used in solid-state laser physics are transition-metal-doped laser gain media ( $\text{Ti}^{3+}$ ,  $\text{Cr}^{2+,3+,4+}$ , ...) and rare-earth-doped laser gain media ( $\text{Nd}^{3+}$ ,  $\text{Yt}^{3+}$ , ...), which this thesis focuses on.

The characteristic optical properties of rare-earth-doped materials result from their unique atomic structure, leading to long metastable state lifetimes, narrow absorption and emission linewidths, and insensitivity to the host materials. The rare-earth metal (or more precisely, the lanthanide) electronic configuration can be written as  $[\text{Xe}]4f^N6s^2$  and is based on the electronic configuration of Xenon with a completely filled 6s shell. Since it is the most stable state, trivalent ions  $\text{X}^{3+}$  are typically incorporated into the host material (crystals or glass). An imperfect screening by the electrons in the 4f orbital leads to an increase in effective nuclear charge when increasing the atomic number. This effect is called lanthanide contraction. The electrons of the 4f shell are well shielded from the host material by enclosing 5s and 5p orbitals. Therefore, the inherent energy level structure from the atomic forces of the rare-earth ion is only weakly disturbed by the crystal field of the host medium. As a result, the energy levels of rare-earth ions are weakly splitting into many sublevels. These Stark manifolds are thermally populated. The optical transitions in the rare-earth ions take place within the 4f shell. These transitions are normally dipole-forbidden, eased by a small influence of the host material. [50]

For crystal lasers, a strong shielding of the electric field of the crystal is responsible for an atomic-like emission spectrum. In contrast to crystals, rare-earth-doped fibers exhibit a broad and smooth emission spectrum. This broad linewidth is based on several line-broadening effects. Both homogeneous and inhomogeneous line-broadening play an essential role in glass hosts. The main contribution to homogeneous broadening in a silica glass host is lifetime broadening, resulting mainly from phonon-induced quenching. A strong inhomogeneous broadening comes from the amorphous glass structure. [7, 10]

These line-broadening effects introduce a variety of opportunities for fiber lasers, especially their broad tunability. For an emission in the 2  $\mu\text{m}$  region, the rare-earth ions thulium and holmium can be used as active laser media to cover a bandwidth of almost 500 nm.

When incorporated into silica, thulium can lase at wavelengths ranging from 1700 to 2050 nm, whereas holmium mainly covers the emission range from 2050 to 2200 nm. However, the luminescence of both ions is much broader, but especially the emission edges are difficult to address at laser operation.

### 2.1.3.1 Thulium-Doped Silica Fiber

Figure 2.8 shows the energy scheme based on the trivalent rare-earth ion thulium incorporated into silica glass [13, 26]. In literature, different labeling of the energy levels can be observed due to mixed energy states. Within this thesis, the energy states are labeled according to a strong and dominant LS coupling. The favored lasing transition, with an emission from 1600 to 2200 nm, is the stimulated emission from the metastable  $^3F_4$  manifold into the ground-level manifold  $^3H_6$ . The according emission and absorption cross sections of this transition are depicted in Fig. 2.9 [25]. Efficient lasing and high-power operation are typically achieved in the wavelength range from 1800 to 2050 nm.

Different pumping schemes [13, 26, 51], like in-band pumping [52, 53] or pumping by 1  $\mu\text{m}$  laser sources [54], have been implemented in research during the last 35 years since the demonstration of the first TDF laser [55].

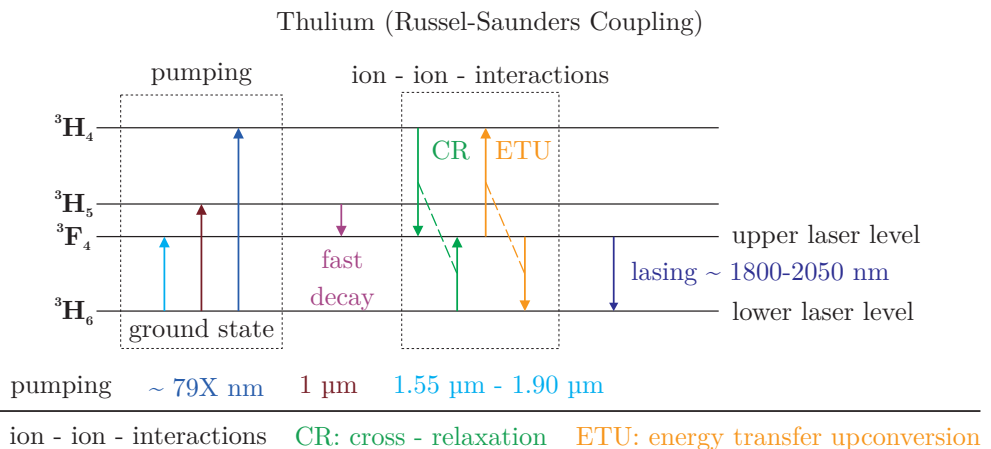


Figure 2.8: Energy level scheme of thulium in LS-coupling notation. TDFs are typically 79X nm diode-pumped for power scaling exploiting an advantageous CR process.

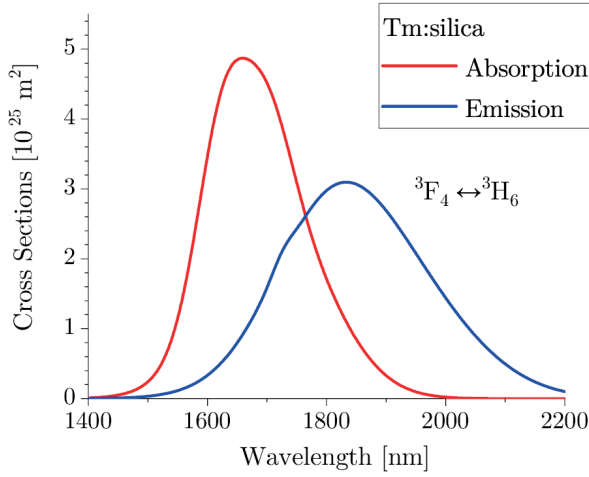


Figure 2.9: Absorption and emission cross sections of the upper laser level  ${}^3F_4$  and lower laser level  ${}^3H_6$  transition of thulium.

The present choice for power scaling at emission wavelengths above  $1.9\ \mu\text{m}$  is the pumping scheme by using powerful, high-brightness diode lasers based on the semiconductor material AlGaAs emitting at  $79X\ \text{nm}$ , populating the  ${}^3H_4$ -energy level.

Due to an advantageous ion-ion interaction called CR [56], an electron is transiting into the upper laser level  ${}^3F_4$  by simultaneously exciting an electron from the ground state into the upper laser level ( ${}^3H_6, {}^3H_4 \rightarrow {}^3F_4, {}^3F_4$ ). Despite having only a Stokes/quantum efficiency of  $\sim 40\%$ , the CR doubles the quantum yield leading to a theoretical efficiency of  $\sim 80\%$ . This efficiency, in combination with the ongoing improvement of high-power diode lasers, makes this pumping scheme highly attractive.

However, to nearly achieve these high efficiencies, high  $\text{Tm}^{3+}$ -ion concentrations must be incorporated into the fiber core [57]. As a result, a large amount of aluminum has to be incorporated to act as a network modifier and increase the upper state lifetime. The aluminum reduces the ion clustering of the laser active ions [58, 59] and additionally lowers the local phonon energy surrounding the rare-earth ion.

Ion clustering features a detrimental ETU process, which is on one side depopulating the upper laser level and on the other side creating heat due to multi-phonon de-excitation. A thulium to aluminum ratio of 1:10 has been shown to enable highly efficient lasing [56] and so far, efficiencies up to  $> 70\%$  have been shown [59].



### 2.1.3.2 Holmium-Doped Silica Fiber

Incorporating holmium as a laser-active medium into a silica fiber enables an efficient laser operation beyond  $2.05\ \mu\text{m}$  up to  $2.2\ \mu\text{m}$  with a luminescence from roughly  $1.8$  to  $2.2\ \mu\text{m}$  [27]. The laser transition responsible for this emission is the transition from the  ${}^5\text{I}_7$  energy level to the  ${}^5\text{I}_8$  energy level.

The energy diagram based on the trivalent rare-earth ion holmium ( $\text{Ho}^{3+}$ ) is depicted in Fig. 2.10. Figure 2.11 shows the corresponding emission and absorption cross sections for the energy level transition of interest ( ${}^5\text{I}_7 \leftrightarrow {}^5\text{I}_8$ ) [28]. Similar to TDF lasers, different pumping schemes have been employed for HDF lasers, whereas in this case, there are no suitable high-power and high-brightness diode lasers matching one of the possible pump schemes. Besides a small fraction utilizing pump sources with an emission wavelength of  $1.15\ \mu\text{m}$ ,  $\text{Ho}^{3+}$ -doped active media are typically in-band pumped by TDF lasers emitting at around  $1.95\ \mu\text{m}$  [60]. By using this resonant pumping scheme, the theoretical quantum efficiencies are  $> 90\%$ . Again, due to the high concentrations of active ions, the  $\text{Ho}^{3+}$  ions tend to cluster and feature a detrimental ETU process ( ${}^5\text{I}_7, {}^5\text{I}_7 \rightarrow {}^5\text{I}_5, {}^5\text{I}_8$ ) [31, 32]. Identical to TDFs, the clustering induced  ${}^5\text{I}_7$  energy level quenching can be reduced by adding additional aluminum into the core [61].

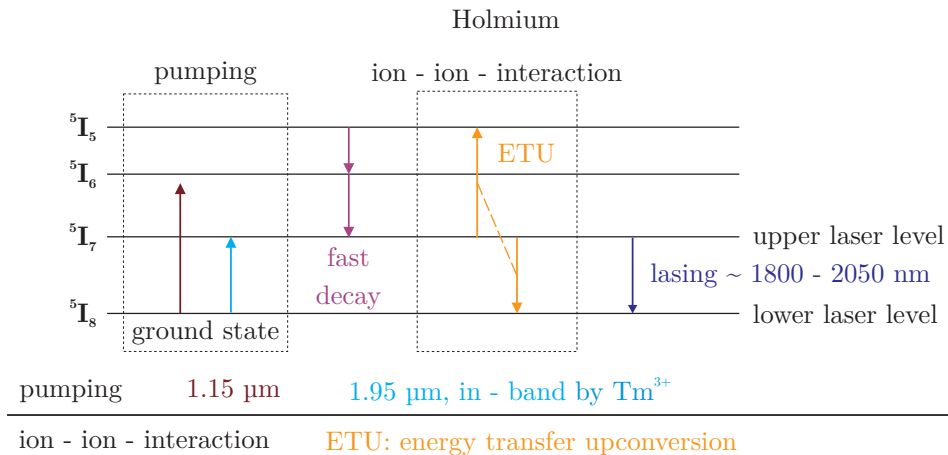


Figure 2.10: Energy level scheme of holmium. HDF lasers are typically in-band pumped by TDF lasers, showing a theoretical quantum efficiency of  $> 90\%$ .

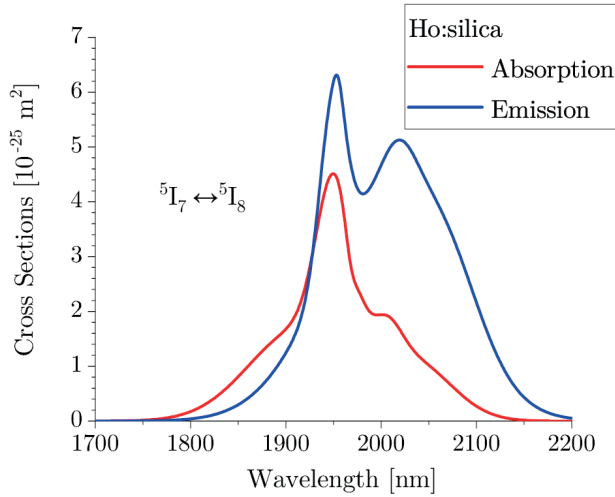


Figure 2.11: Absorption and emission cross sections of the upper laser level  $^5I_7$  and lower laser level  $^5I_8$  transition of holmium.

### 2.1.3.3 Tm:Ho-Codoped Silica Fiber

High-power and high-brightness diode lasers build the fundamental basis for the power scaling of fiber lasers. Due to the lack of these sources for most of the laser-active ions, sensitizers can be used as codopants to absorb the pump radiation and transfer the energy afterward to the targeted upper laser level. Therefore, codoping HDFs with  $Tm^{3+}$ -ions enables an advantageous pump scheme with suitable diode lasers [33] and a simplified setup by avoiding building a TDF lasers as intermediate pump stages. A critical pre-condition, like for the in-band pumping schemes, is an overlap of the absorption cross section of the targeted laser transition and the according emission cross section of the sensitizer ion [62]. The energy diagram of a THF laser is depicted in Fig. 2.12. The  $Tm^{3+}$ -ions absorb the pump radiation of 79X nm diode lasers and populate the  $^3F_4$  upper laser level by exploiting the CR process. Then, the energy can be transferred to the upper laser level  $^5I_7$  of holmium. The holmium ions are now responsible for lasing at 2.1  $\mu m$  and beyond. Recent studies on the doping concentrations show efficient lasing employing a  $Al^{3+}:Tm^{3+}:Ho^{3+}$ -ratio of 100:10:1 [35].

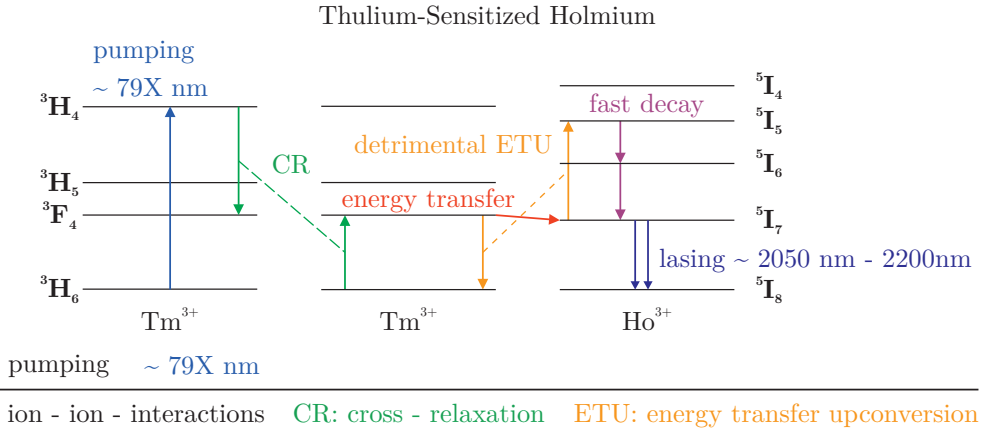


Figure 2.12: Energy level scheme of thulium-sensitized holmium-doped fiber lasers.  $\text{Tm}^{3+}:\text{Ho}^{3+}$ -codoped fiber lasers are pumped by 79X nm diodes, where the thulium ions can absorb this radiation. Thulium's standard CR process, followed by an energy transfer mechanism, is effectively populating the upper laser level of holmium, enabling lasing at wavelengths beyond 2  $\mu\text{m}$ .

### 2.1.3.4 Relevant Fiber Types - II (Active Fibers)

After introducing the concept of (fiber) lasers and the active media thulium and holmium, the list of fiber types, introduced in Section 2.1.1, can be extended.

High thulium and aluminum concentrations, required for efficient laser operation, result in a high refractive index of the core and a high refractive index difference to the pure silica cladding. According to Eq. (2.7), the core size needs to decrease to maintain an actual single-mode fiber, leading to higher core intensities accompanied by a lower threshold for fiber damage and nonlinearities. To avoid decreasing the fiber core, the active fiber core is instead surrounded by a several-micron-thick layer of doped material. This additional cladding is called **pedestal** [63] and is displayed on the left-hand side of Fig. 2.13. This pedestal restores a low core NA and a pure single-mode behavior.

Moreover, the core size is not only maintained but intentionally increased allowing even larger nonlinear and power damage threshold. These so-called **large mode area (LMA)** fibers [64] have a typical core diameter of 15 to 25  $\mu\text{m}$ . The core NA is decreased to keep these fibers single-mode according to Eq. (2.7). Since it is not always possible to achieve single-mode behavior and a small core NA features high losses while bending the fiber, LMA fibers can be designed to be slightly multi-mode.

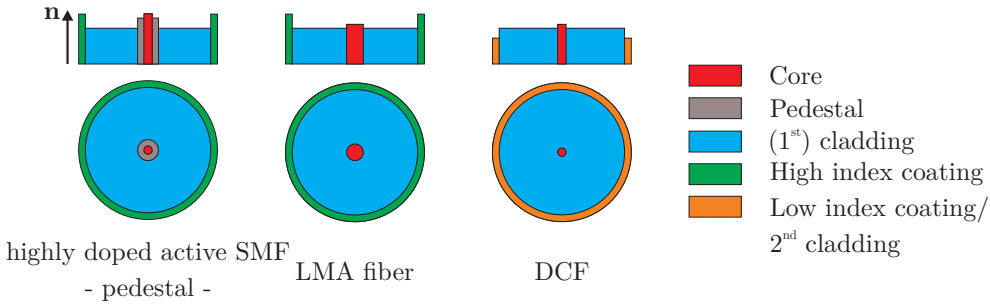


Figure 2.13: Comparative schematic of fiber concepts for active fibers. Pedestals, LMA-fibers, and the DCF-geometry are essential for power scaling of fiber lasers while maintaining single-mode operation as well as a large damage and nonlinear threshold.

Nevertheless, a single-mode operation can be achieved by coiling the fiber and introducing additional loss to higher-order modes. Another concept essential for power scaling fiber lasers is the **double-clad fiber (DCF)** geometry [65, 66], which is depicted on the right-hand side of Fig. 2.13. High-power pump sources like diode lasers are only power scalable with the drawback of low spatial brightness, resulting in a challenging or impossible coupling into the core of an active fiber. By using a low-index polymer instead of a high-index polymer, the first cladding becomes guiding for the pump radiation, and powerful low-brightness, multi-mode pump sources can be used for pumping these fibers, easing power scaling of the pump sources and incoupling of the pump radiation into the active fiber. For this kind of fiber, it is essential to suppress skew rays, which are eigenmodes of the cladding geometry and do not cross the active core region. By breaking the rotational symmetry of the fiber, using an octagonal cladding, a D-shaped cladding, or stress-rods of a PANDA-type fiber, the pump light is sufficiently scrambled.

To conclude, different fiber concepts and geometries have been developed and established over time. The concepts that have been introduced are typically not applied individually but are strategically combined.

## 2.1.4 Q-Switching Theory

For some applications, it is required to repetitively generate much higher output powers for a short time scale than what is feasible in continuous-wave operation. In this case, a pulsed version of a laser can generate high peak intensities despite having moderate average laser output power.

For generating high pulse energies, methods like gain-switching, Q-switching, and mode-locking can be used. Q-switching is the perfect choice for generating pulse durations in the nanosecond regime. The theoretical part of Q-switching is adapted from [45, 67]. The Q-factor or quality factor  $Q$  of the cavity defines the capability of an optical system to store energy and is defined by

$$Q = 2\pi \frac{E_{\text{stored}}}{E_{\text{dis}}}. \quad (2.21)$$

$E_{\text{stored}}$  is the energy stored in the system, and  $E_{\text{dis}}$  is the dissipated energy during one (dipole-) oscillation of the electric field. By modulating the intra-cavity losses  $\Lambda_i$  and, therefore, the Q-factor, energy can be stored/accumulated in the gain medium. A certain amount of the stored energy is then released within a single short pulse.

The schematic of Q-switching is depicted in Fig. 2.14 and will be explained in more detail in the following.

To understand the process of Q-switching quantitatively, Section 2.1.2 provides the required theory and formulas. However, to derive crucial parameters for Q-switched laser operation and their dependencies, the process has to be investigated more carefully.

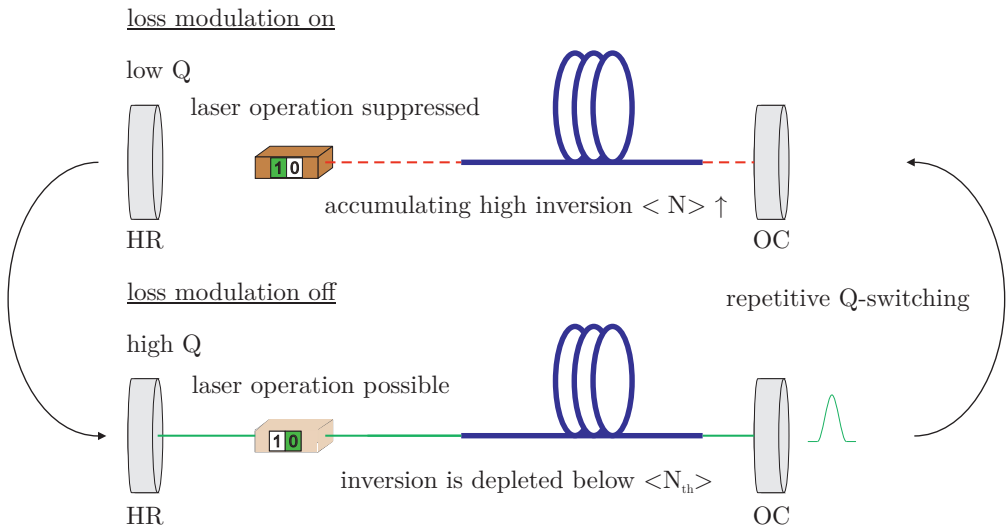


Figure 2.14: The upper part shows a 'closed' cavity, where a switched-on loss modulator lowers the Q-factor of the cavity via intra-cavity losses and suppresses lasing. An inversion accumulates far above the threshold inversion. When the loss modulator is switched off, the former Q-factor of the cavity is restored with a low threshold inversion. A large pulse builds up. After the pulse, the loss modulator is switched on again, repeating this cycle.

In the beginning, a loss modulator (e.g., an acousto-optic modulator (AOM)) is switched on and blocks the cavity. By introducing this additional intra-cavity loss, the Q-factor of the cavity is lowered dramatically. According to Eq. (2.10), the required single-pass gain  $G$  and, simultaneously, the required inversion  $\Delta N$  for reaching the lasing threshold increase.

However, there are certain limits to the possibly creatable inversion. On the one hand, the fluorescence is counteracting the pumping phase  $T_p$  of the active laser medium leading to a limited growth of the pump efficiency. The pump duration  $T_p$  is considered identical to the time when the loss modulator blocks the cavity. At some point, the inversion saturates, and further pumping is counteracted by spontaneous emission. On the other hand, the high single-pass gain for fiber lasers supports the oscillation of parasitic modes, and enhanced amplified spontaneous emission (ASE) leads to a clamping of the inversion. Therefore, the cavity must be designed to prevent these processes and allow an efficient inversion build-up. When the loss modulator is switched off, the normal Q-factor of the cavity is restored and the inversion at this time is termed the initial inversion  $\langle \Delta N \rangle_i$ . The present inversion and, therefore, the gain are much higher than their threshold counterparts.

The photon field density  $\Phi$  is built up from vacuum noise, and in a first approximation, the inversion is treated as constant to derive the pulse build-up time  $T_b$  [45]:

$$T_b \approx (22.5 \pm 5) \frac{\tau_c}{r - 1}. \quad (2.22)$$

$T_b$  is the time needed to build a photon field density  $\Phi$  equivalent to the normal CW operation of the laser system. Until the laser output power is reached for continuous-wave operation, the inversion is not considerably decreased and assumed as constant. After the pulse build-up time, the photon field density is strongly rising according to the high gain and is, therefore, effectively depleting the inversion. The pump parameter  $r$  is defined as

$$r := \frac{\langle \Delta N \rangle'_i}{\langle \Delta N \rangle'_{th}} \approx \frac{P_p}{P_{th}} \quad (2.23)$$

and is roughly equivalent to the ratio of the actual pump power and the threshold pump power. It can be seen immediately that the larger the inversion while blocking the cavity, the faster the pulse builds up when returning to a high Q-factor.

The auxiliary variable  $\langle \Delta N \rangle'_i$  and  $\langle \Delta N \rangle'_f$  are defined as:

$$\langle \Delta N \rangle'_k = \langle \Delta N \rangle_k - \frac{\sigma_-(\lambda_s)}{\sigma_+(\lambda_s)} \langle N \rangle \quad (2.24)$$

with  $k \in \{i, f, th\}$ . The photon field density  $\Phi$  increases while net amplification is possible within the gain medium. This is the case till the threshold inversion  $\langle \Delta N \rangle_{th}$  and, therefore, the peak of the pulse are reached. Afterward, the photon field density decreases again. The final inversion  $\langle \Delta N \rangle'_f$  after the pulse is smaller than the threshold inversion since a huge photon field is heavily depleting the upper laser level. The main equation, which describes the Q-switching process, the Q-switch master equation [45], is

$$\frac{\langle \Delta N \rangle'_f}{\langle \Delta N \rangle'_i} = 1 - \frac{1}{r} \ln \frac{\langle \Delta N \rangle'_i}{\langle \Delta N \rangle'_f}. \quad (2.25)$$

The only important parameters to describe the Q-switching process are the initial inversion  $\langle \Delta N \rangle_i$  and the final inversion  $\langle \Delta N \rangle_f$ , where the laser system has to be optimized for.

For repetitive Q-switching, the active laser material is pumped continuously. After the pulse is completely released, the low Q-factor is restored by switching the loss modulator on again. Without restoring the low Q-factor, the oscillator would pass into continuous-wave laser operation.

The inversion and the photon field oscillate around their continuous-wave values until reaching a steady state. This has to be considered by choosing the right time intervals for blocking and opening the laser cavity.

One important parameter is pulse duration  $t_p$  [45], which is also dependent on  $r$  and converges toward the cavity photon lifetime for strong pumping.

$$t_p \approx \frac{r\eta_e(r)}{r-1-\ln r} \tau_c \xrightarrow{r \gg 1} \tau_c \quad (2.26)$$

Figure 2.15 shows the evolution of the cavity losses, population inversion, and the photon field during one Q-switch cycle. Calculating the cavity photon lifetime, e.g., for a fiber length of 5 m, an OC reflectance of 3%, and additional cavity losses of 3% leads to 13.7 ns confirming the operation in a nanosecond regime. Looking at the equations mentioned so far, some simple rules for efficient Q-switching can be derived. The key message is that a large above-threshold inversion must be established while the cavity is in a low Q-factor state. For achieving this goal, a well-designed cavity suppressing parasitic lasing is an effective tool.

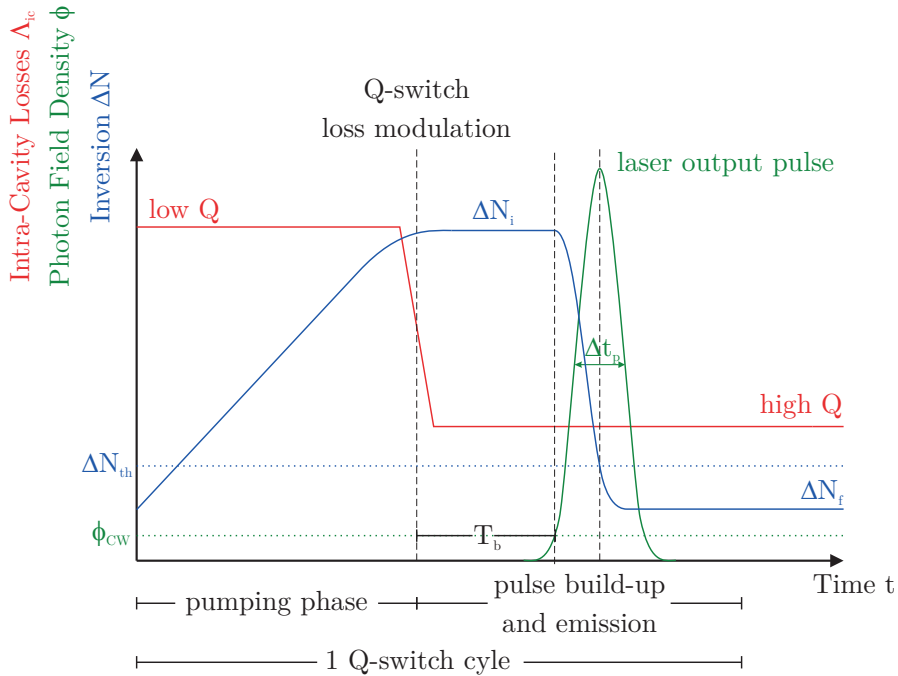


Figure 2.15: Representative diagram for the evolution of the internal losses  $\Lambda_i$ , the inversion  $\Delta N$  and the photon field density  $\Phi$  during one Q-switch cycle.

There are different ways a Q-switching experiment can be performed in the laboratory. One possibility is to work with a constant pump power  $P_{\text{pump}}$  and to decrease the pulse repetition frequency successively. The off-time of the loss modulator is determined by the sum of the pulse build-up time and the pulse duration. The cavity is blocked for the rest of the cycle, and an inversion  $\langle \Delta N \rangle_i$  builds up. By reducing the repetition frequency, the time for one cycle is increased. This time is used to build up a higher inversion than for previous repetition rates. This intuitively leads to higher pulse energies and a shorter pulse build-up time. Assuming a constant average laser output power, the pulse energy scales inversely with the pulse repetition rate for a continuous pump power. The repetition frequency can be decreased until the pumping phase is long enough to reach the threshold inversion for the oscillation of a parasitic mode. This is mainly the limiting case in fiber lasers since the single-pass gain is substantially high that even small reflections can cause parasitic lasing.



The maximum pulse energy  $k_s$  is a characteristic of the laser setup under investigation and is calculated by [67]:

$$P_{\text{pump}}^{\text{max}} = \frac{k_s \nu_{\text{rep}}}{\eta_s}. \quad (2.27)$$

$P_{\text{pump}}^{\text{max}}$  is the maximum pump power without the occurrence of parasitic lasing for a specific repetition rate (RR). Increasing the pump power and simultaneously the RR, the same maximum pulse energy  $k_s$  will be reached before limiting effects intervene. For Q-switching, it is essential to remember that the pulse duration, pulse shape, and pulse energy are inherent properties of the process and are related.

## 2.2 Nonlinear Frequency Conversion

This section intends to lay the basic idea of nonlinear frequency conversion and OPOs. It is not intended or needed to give a thorough elaboration of nonlinear optics. The reader referred to corresponding literature like [68–71]. Nevertheless, basic concepts such as nonlinear polarization, effects of phase mismatch, and phase matching techniques need to be discussed. Having in mind the importance of good phase matching, the need for the development of a pump laser with outstanding optical characteristics, as well as the need for the development of high-quality nonlinear materials, is highlighted. In the beginning, the origin of the nonlinear frequency conversion needs to be clarified.

### 2.2.1 Nonlinear Polarization

This section contains important steps toward the coupled wave equation of second-order interactions. They are taken from [72] and can be referred to for more details. So far, the electric field  $\vec{E}$  is assumed to contribute linearly to the polarization  $\vec{P}$  for a time-invariant material. The electrical displacement  $\vec{D}$  reads as [72]:

$$\vec{D}(\vec{r}, t) = \epsilon_0 \vec{E}(\vec{r}, t) + \vec{P}(\vec{r}, t) = \epsilon_0 \vec{E}(\vec{r}, t) + \vec{P}_l(\vec{r}, t) \quad (2.28)$$

$$= \epsilon_0 \vec{E}(\vec{r}, t) + \int_{\tau} \iiint_{\vec{r}'} \chi(\vec{r}', \tau) \vec{E}(\vec{r}', t - \tau) d\vec{r}' d\tau. \quad (2.29)$$

The electric permittivity of vacuum  $\epsilon_0$  is  $8.854\,19 \cdot 10^{-12}$  A s/(V m).  $\chi$  is a (3x3)-matrix and refers to the first-order (linear) susceptibility. The term nonlinear in nonlinear optics means that the response of a material to an applied optical field depends nonlinearly on the field strength. In general, the expression of the nonlinear polarization  $P_{nl}$  is expanded to a Volterra series and tends to become quite confusing. For the sake of simplicity and readability, a few assumptions are made to treat the description of nonlinear optics in a simpler way, which is enough to understand the relevant theme of this thesis.

In the regime of weak nonlinearities, the polarization of lossless, time-invariant, isotropic, homogeneous media, which is local in space, can be expanded in a power series [72]:

$$P(z,t) = P_l(z,t) + P_{nl}(z,t) \quad (2.30)$$

$$= \underbrace{\epsilon_0 \chi E(z,t)}_{\text{linear part}} + \underbrace{\epsilon_0 \chi^{(2)} E^2(z,t) + \epsilon_0 \chi^{(3)} E^3(z,t) + \dots}_{\text{nonlinear part}} \quad (2.31)$$

$\chi^{(n)}$  refers to the n-th order nonlinear susceptibility.  $\vec{E}$  and  $\vec{P}$  are propagating in z-direction and are either polarized in x-direction or y-direction, leading to a one-dimensional problem.

Typically, the first non-vanishing nonlinear expansion term is investigated regarding nonlinear processes. Simple symmetry considerations for the material under investigation can be used to reduce the expansion terms significantly. For materials with inversion symmetry, the nonlinear susceptibilities of even order vanish. For example, the first nonlinear contribution in amorphous materials like glasses is from the third order. By introducing the adapted nonlinear polarization, the revised wave equation for propagation in nonlinear material is given by [72]:

$$\partial_z^2 E(z,t) - \frac{n^2}{c^2} \partial_t^2 E(z,t) = \mu_0 \partial_t^2 P_{nl}(z,t). \quad (2.32)$$

Compared to the wave equation for linear media (Eq. (2.3)), the differential equation has a driving force on the right-hand side of the equation. This means that the nonlinear polarization acts as a source for new frequency components of the electric field.

## 2.2.2 $\chi^{(2)}$ -Nonlinearities and Optical Parametric Generation

Within this section, the focus is set on  $\chi^{(2)}$ -nonlinearities and OPG, which are both fundamental for understanding OPOs. These  $\chi^{(2)}$ -processes are also referred to as three-wave mixing, since the nonlinear medium couples three waves.

The electrical field is composed of a superposition of two plane waves with frequency components  $\omega_1$  and  $\omega_2$ , field amplitudes  $E_1$  and  $E_2$ , and wave vectors  $k_1$  and  $k_2$ :

$$E(z,t) = \frac{1}{2} \left( (E_1 e^{i(\omega_1 t - k_1 z)} + E_2 e^{i(\omega_2 t - k_2 z)}) + c.c. \right). \quad (2.33)$$

The second-order polarization  $P_{nl}^{(2)}$  can be written as:

$$P_{nl}^{(2)} = \frac{1}{4} \epsilon_0 \chi^{(2)} \left( \underbrace{E_1^2 e^{2i(\omega_1 t - k_1 z)} + E_2^2 e^{2i(\omega_2 t - k_2 z)}}_{\text{Second Harmonic Generation}} + \underbrace{2E_1 E_2 e^{i((\omega_1 + \omega_2)t - (k_1 + k_2)z)}}_{\text{Sum Frequency Generation}} \right. \\ \left. + \underbrace{2E_1 E_2 e^{i((\omega_1 - \omega_2)t - (k_1 - k_2)z)}}_{\text{Difference Frequency Generation}} + \underbrace{2|E_1|^2 + 2|E_2|^2}_{\text{Optical Rectification}} + c.c. \right). \quad (2.34)$$

Equation (2.34) shows the different second-order nonlinear processes which can occur. The oscillating parts of the nonlinear polarization are called second harmonic generation, sum frequency generation, and difference frequency generation. These polarization terms are the origin of new electrical fields with twice the frequency of the input electrical fields, the sum of the frequencies of the input electrical fields, or the difference of the frequencies of the input fields. Since two frequency components are converted into other frequencies, it is also referred to as nonlinear frequency conversion. In addition, optical rectification adds a constant value to the nonlinear polarization. [72]

In fact, all of these nonlinear processes take place within a nonlinear non-centrosymmetric medium. However, in general, no efficient amplification takes place. To take advantage of one of these processes, the so-called phase-matching condition needs to be fulfilled. This phase matching condition determines which of the nonlinear process takes place.

To build an OPO, the process of OPG is used. This process is formally equivalent to difference frequency generation (DFG). In the case of DFG, the signal, which is intended to be amplified, is seeded into the nonlinear crystal together with an intense pump wave. In contrast, for OPG, only the pump radiation is sent into the crystal. The pump photon with energy  $\hbar\omega_p$  is converted into two photons, a signal photon with energy  $\hbar\omega_s$  and an idler photon with energy  $\hbar\omega_i$ . An energy diagram is shown in Fig. 2.16, and the energy conservation reads as

$$\hbar\omega_p = \hbar\omega_s + \hbar\omega_i. \quad (2.35)$$

For further investigations, the nonlinear polarization and the electrical field are inserted into the nonlinear wave Eq. (2.32).

The differential equation of second order can be simplified by assuming a slowly varying envelope, leading to 3 coupled first-order equations for parametric second-order interaction [69]:

$$\partial_z E_p(z, t, \omega_p) = i \frac{\omega_p}{cn(\omega_p)} d_{eff} E_s(z, t, \omega_s) E_i(z, t, \omega_i) e^{-i\Delta k z}, \quad (2.36)$$

$$\partial_z E_s(z, t, \omega_s) = i \frac{\omega_s}{cn(\omega_s)} d_{eff} E_p(z, t, \omega_p) E_s^*(z, t, \omega_s) e^{i\Delta k z}, \quad (2.37)$$

$$\partial_z E_i(z, t, \omega_i) = i \frac{\omega_i}{cn(\omega_i)} d_{eff} E_p(z, t, \omega_p) E_i^*(z, t, \omega_i) e^{i\Delta k z}. \quad (2.38)$$

$d_{eff}$  is the effective nonlinear coefficient. This set of coupled equations describes the  $\chi^{(2)}$ -mechanisms. The all-determining parameter is the phase mismatch between the pump wave and the waves of signal and idler

$$\Delta k = k_p - k_s - k_i = \frac{1}{c} (n(\omega_p)\omega_p - n(\omega_s)\omega_s - n(\omega_i)\omega_i). \quad (2.39)$$

The initial process for starting OPG is called spontaneous parametric down-conversion, parametric fluorescence, or parametric noise [69]. The zero-point fluctuations radiate in all directions and frequencies while fulfilling energy conservation.

Therefore, OPG can be seen as DFG with one initiating photon present at the entrance of the crystal. Such an amplification from quantum noise while propagating through the crystal is only possible when phase matching is guaranteed. A schematic representation of OPG is displayed in Fig. 2.16.

Assuming no pump depletion, no idler input field, and a non-vanishing signal input, a parametric gain for the signal

$$G = \frac{P(L)}{P(0)} - 1 = (\Gamma L)^2 \frac{\sinh^2 \left( \sqrt{(\Gamma L)^2 - (\Delta k L / 2)^2} \right)}{(\Gamma L)^2 - (\Delta k L / 2)^2}, \quad (2.40)$$

$$\text{with } \Gamma = 4\pi d_{eff} \sqrt{\frac{I_p(0)}{2\epsilon_0 n_p n_s n_i c \lambda_s \lambda_i}} \quad (2.41)$$

can be deduced by solving the coupled Eq. (2.38) [69].

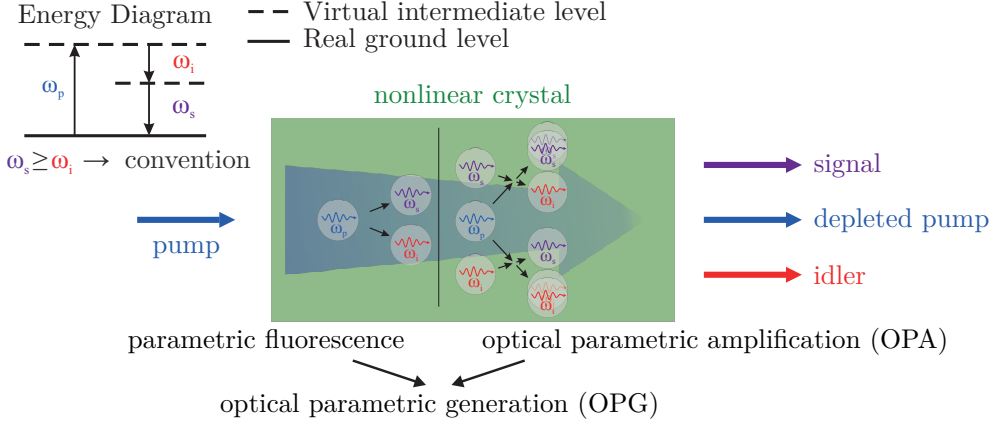


Figure 2.16: The schematic shows the process of OPG. Intense pump radiation builds up the signal and the idler waves when phase matching is ensured. The process is initialized by parametric fluorescence.

It is important to note that the gain coefficient  $\Gamma$  is dependent on the input field intensity of the pump. Therefore, to optimize and improve the nonlinear gain, high pump intensities must be used and a sufficient phase matching must be reached. For an illustrative discussion of the effect of phase mismatch, the parametric gain is considered in a low gain regime ( $\Gamma L \ll \Delta k L / 2$ ). It can be distinguished between perfect phase matching  $\Delta k = 0$  and a phase mismatch  $\Delta k \neq 0$ . At the end of the nonlinear crystal with length  $L$ , the intensity of the signal wave can be expressed as follow:

$$\Delta k = 0 : I_s \propto d_{eff}^2 L^2, \quad (2.42)$$

$$\Delta k \neq 0 : I_s \propto d_{eff}^2 L^2 \text{sinc}^2 \left( \frac{\Delta k L}{2} \right). \quad (2.43)$$

Out of these equations, the importance of phase matching can be emphasized. The signal intensity increases quadratically along the propagation distance for perfect phase matching, which is depicted on the left-hand side of Fig. 2.17 (green curve). Without a constantly proper phase relation between the three fields, the intensity of the signal wave has a sinusoidal behavior. In this case, the conversion is efficient for short propagation distances, but with increasing propagation, the phase mismatch accumulates, and the fields oscillate out of phase. This leads to a back conversion and a decrease in the intensity of the idler. With an increase of  $\Delta k$ , the period and amplitude of the sinusoidal behavior decrease.

This shows the importance of the phase matching condition in order to efficiently operate the OPO. The right-hand side of Fig. 2.17 shows the square of the sinc function in dependence on its argument. After the propagation distance  $L$ , the efficiency of the nonlinear process can be calculated for a specific phase mismatch. Ideally,  $\Delta k = 0$  is targeted for an optimum frequency conversion. However, this is sometimes difficult to achieve even for one pump frequency component. Therefore, it is advisable to stay within the acceptance bandwidth, which is the full width at half maximum (FWHM) of the  $\text{sinc}^2$  function, being considered as an efficient nonlinear process [73, 74].

It even turns out that in most of the cases, phase matching is not possible at all in isotropic nonlinear media. As long as the material dispersion of the nonlinear medium is a continuous and monotonic function, which is the case between two resonances, Eq. (2.39) and Eq. (2.35) cannot be satisfied at the same time. Therefore, no efficient accumulation of a nonlinear process can occur. Nevertheless, two effective ways to achieve phase matching will be explained in the following. [68]

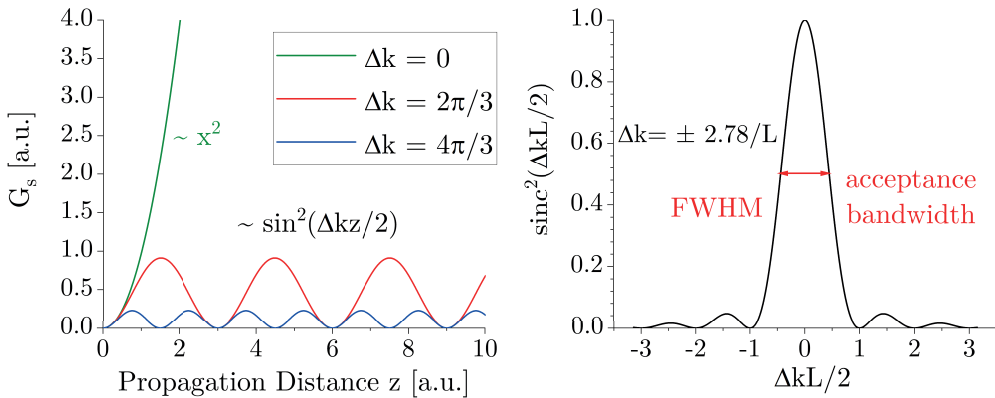


Figure 2.17: Left: Signal gain in dependence on the propagation distance for different phase mismatch values. Only the case of no phase mismatch leads to a continuous signal increase. Otherwise, the gain is oscillating. Right: The square of the sinc-function represents the efficiency of the parametric process in dependence on a phase mismatch.

### 2.2.3 Birefringent Phase Matching

One opportunity to achieve phase matching and enable efficient frequency conversion is using birefringent materials, exploiting different refractive indices for different polarizations [68]. It can be distinguished between the relatively simple uniaxial crystals and the more complex biaxial crystals. Within a birefringent material, the optical axis describes a propagation direction where the refractive index is the same for every wave independent of the polarization. There are one and two optical axes for a uniaxial and a biaxial crystal, respectively.

This thesis focuses on uniaxial crystals, more precisely on positive ( $n_e > n_o$ ) uniaxial nonlinear materials. The wave polarization, which lies in the plane spanned by the propagation direction and the optical axis, is called the extraordinary wave *e*. The polarization of the wave, which is orthogonal to this plane, is called the ordinary wave *o*. The ordinary wave always experiences the ordinary refractive index  $n_o$ , whereas the refractive index of the extraordinary wave  $n_e(\theta)$  depends on the angle between the optical axis and the propagation direction. The left-hand side of Fig. 2.18 shows the index ellipsoid and its *xz*-cut. The equation for the optical indicatrix [68], which allows calculating the corresponding refractive index for the extraordinary wave, is

$$\frac{1}{n_e^2(\theta)} = \frac{\cos^2(\theta)}{n_o^2} + \frac{\sin^2(\theta)}{n_e^2}. \quad (2.44)$$

For one propagation direction of the pump wave inside the crystal, there are only one or two sets of matching signal and idler waves. The crystal has to be rotated to reach other sets of signal and idler wavelengths. By rotating the crystal, the phase-matching condition is fulfilled for another set of wavelengths. This technique is also called angle tuning and its schematic representation is displayed on the right-hand side of Fig. 2.18.

In general, three waves with two polarizations lead to 8 permutations of  $p_1 \rightarrow s_m i_n$ . *l*, *m*, and *n* represent the two polarizations *o* and *e*. As already discussed, the same polarization for all three waves is impossible. Therefore, two possibilities remain for type I phase matching (*o*-*ee*,*e*-*oo*) and four for type II phase matching (*o*-*eo*/*oe*, *e*-*eo*/*oe*). Type I phase matching refers to the same polarization for the two "red" waves, and type II phase matching refers to the opposite polarization for the two "red" waves. The term "red" specifies a wave with a longer wavelength. Due to the nature of the refractive index dispersion of a positive uniaxial medium, the pump wave must have an ordinary polarization to fulfill the phase-matching condition given by Eq. (2.39) [68]. Therefore, type I phase matching requires ***o*→*ee*** and type II phase matching requires ***o*→*eo/oe*** [73].

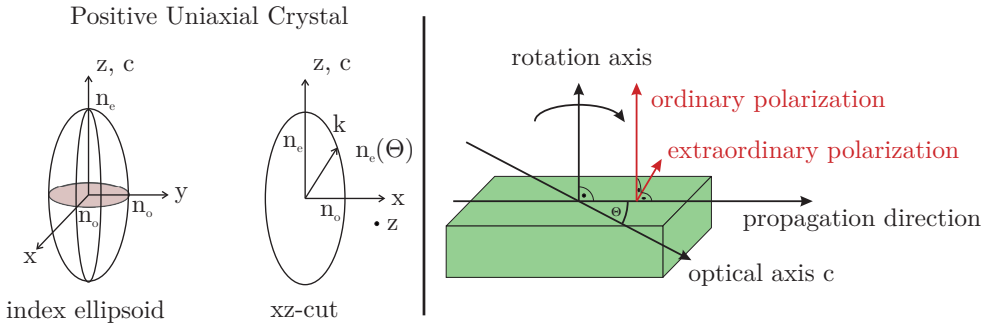


Figure 2.18: Left: The refractive index ellipsoid for a positive uniaxial crystal and its  $xz$ -cut can be used for calculating essential parameters like the extraordinary refractive index and the walk-off angle. Right: The schematic displays the process of angle tuning for critical phase matching in a uniaxial crystal.

Tuning the angle of the crystal has quite a strong influence on the phase matching condition. Therefore, this phase matching technique is called critical phase matching and has drawbacks like a walk-off between ordinary and extraordinary waves. The pump, the signal, and the idler wave have a finite beam size, and while propagating through the crystal, the overlap decreases, leading to a less efficient nonlinear process. [68]

## 2.2.4 Quasi-Phase-Matching

Birefringent phase matching is widely used, however, only limited applicable. On the one hand, birefringent phase matching is only possible with a sufficiently strong birefringence far from a material resonance. In addition, angle tuning reduces the efficiency of the nonlinear conversion since most materials exhibit the strongest effective nonlinear coefficient  $d_{eff}$  when propagating along a principal axis. On the other hand, there are a lot of nonlinear crystals with high nonlinear coefficients, but due to a missing birefringence cannot be phase matched by this approach. [68] Another opportunity to achieve phase matching even for isotropic materials is quasi-phase-matching (QPM). Exploiting QPM, the different waves can propagate along a principle axis without any spatial walk-off, and even non-birefringent materials can be used. As shown in Fig. 2.17, having a small phase mismatch between the oscillating waves leads to an oscillating conversion and back conversion process. When the fields exhibit a phase mismatch of  $\pi$ , the nonlinear conversion will stop, and a back conversion will take place for further propagation. The idea behind QPM is to stop the nonlinear conversion process here and "cut" the domain [75].



The subsequent nonlinear material is replaced by an inverted material in a way that the effective nonlinear coefficient changes its sign. An additional phase shift of  $\pi$  is introduced. Therefore, instead of a back conversion, the nonlinear conversion continues. QPM is utilizing periodic structures with inversed nonlinear coefficients to achieve a continuous energy flow from the pump wave to signal and idler. The left-hand side of Fig. 2.19 shows a nonlinear crystal, which is periodically altering the sign of the effective nonlinear coefficient, indicated by red and beige colored domains. The grating period  $\Lambda$  comprises equally large parts of both materials. Figure 2.19 shows the gain of the signal in dependence of the propagation distance  $x$  and visualizes the effect of QPM. When the three-wave mixing process has acquired a phase mismatch of  $\pi$ , the new domain is introduced. This curve is depicted in red. Sometimes it is challenging to manufacture such small periods. In such a case, it is also possible to switch the domain after an acquired phase difference of  $m\pi$  ( $m = 1, 3, 5, \dots$ ). The process is called  $m$ -order QPM. The phase matching condition represented by Eq. (2.39) can be adapted for the case of QPM [73]:

$$\Delta k = k_p - k_s - k_i - k_m = \frac{1}{c} (n(\omega_p)\omega_p - n(\omega_s)\omega_s - n(\omega_i)\omega_i) - \frac{2\pi m}{\Lambda} \quad (2.45)$$

As seen on the right-hand side of Fig. 2.19, the most efficient process is the first-order QPM. The graph indicates a lower conversion efficiency of QPM compared to birefringent phase matching.

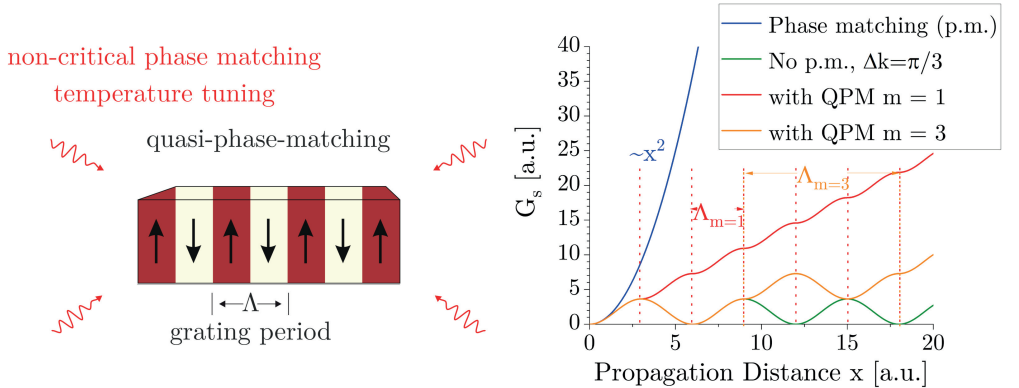


Figure 2.19: Left: Schematic of a quasi-phase-matchable nonlinear medium. Alternating domains are inducing a phase shift of  $\pi$  to suppress or skip the back conversion but restart the conversion process. Right: Signal gain as a function of the propagation distance showing the effect of QPM.

This is deceptive since with QPM, the propagation direction within a principal axis can be chosen. The propagation along a principal axis prevents spatial walk-off and allows exploiting the crystal's strongest nonlinear coefficient. [68, 73, 76]

## 2.2.5 Optical Parametric Oscillator

As Eq. (2.41) states, the single-pass parametric gain depends on the input intensity of the pump wave. Due to the typically low (peak) intensities of nanosecond pulses created by Q-switching, the single pass gain is relatively small. Therefore, there is no significant parametric generation of signal and idler when building up from quantum noise. In this case, the same principle as for lasers can be used. By introducing feedback to the nonlinear crystal, identically to a laser resonator, signal and idler wave can be generated more efficiently. [74]

Figure 2.20 shows a linear OPO scheme. The cavity consists of an incoupling mirror, a nonlinear crystal, and an OC mirror. The incoupling mirror is transparent for the pump radiation, whereas the OC mirror can either be transmissive or reflective. Signal and idler waves are generated and amplified only if phase matching is established. Thus, there is only gain for both propagation directions inside the cavity of signal and idler when the pump is retroreflected by the OC mirror. However, a retroreflection of the pump is avoided quite often since this back reflection can influence, disturb, or damage the laser pump source itself. The linear cavity is the most simple and widely used setup.

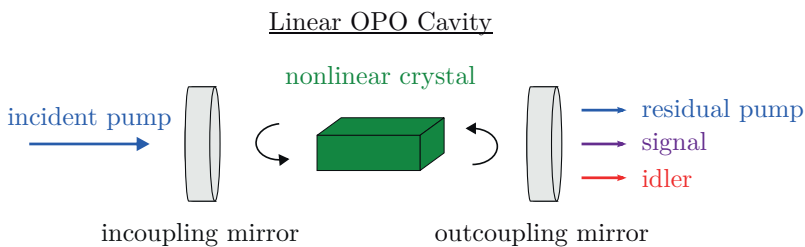


Figure 2.20: Schematic of an OPO, which consists of an incoupling mirror, the nonlinear crystal, and an outcoupling mirror. The cavity is built in a simple linear manner. Depending on the required conditions, the mirrors can have varying functionality. There are single and doubly resonant cavities for signal and idler with retroreflecting and non-retroreflecting OC mirrors for the pump radiation.

It can be distinguished between a singly resonant cavity, where only one of the generated waves (signal or idler) is oscillating, or a doubly resonant cavity, where both signal and idler are oscillating in the cavity [69]. Besides the presented linear configuration, ring cavities with increased complexity exist with three [77] or four mirrors [78] exhibiting advantages like the possibility of no inherent retroreflection by mirror optics or the nonlinear crystal. In addition, there are out-of-plane OPO cavities like RISTRA [79] and FIRE [80], showing an increased complexity. However, an excellent beam quality can be achieved due to an image rotation, even for larger OPO output powers.

The threshold condition for the OPO is derived identically to the one for laser operation [40]. The self-consistency must hold for signal and idler separately. For laser sources with low peak intensities, the threshold for starting the parametric oscillation is difficult to reach. Consequently, the pump radiation is strongly focussed on the crystal to enhance the intensity.



# 3 Laser Setup and Optimization for High-Power Laser Operation

This chapter addresses important aspects of power scaling, which apply in general but especially to the kind of setup used within this work. The difficulties and challenges of power scaling a free-space single-oscillator are described. During this thesis, it has become clear that power scaling of a laser system is not only increasing the pump power by installing more powerful laser diodes. Besides increasing laser output power and pulse energy, appropriate optical characteristics of the laser must be obtained or maintained compared to low-power setups, which increases the complexity of the system.

The following list gives a short overview of some fundamental aspects:

- **Choice of the fiber setup and the active fiber:**

First, the fiber setup and the fibers must be chosen according to the application requirements and the desired laser output characteristics. What laser output powers are targeted, does the laser rely on clad- or core-pumping, is a linearly polarized output required, or are fiber nonlinearities expected? These questions need to be answered in advance and directly influence the setup and the fiber selection for the setup. A brief scheme of the fiber laser setup under investigation within this thesis and the novel fiber design developed for high-power laser operation at emission wavelengths above 2.1  $\mu\text{m}$  are described in Section 3.1.

- **Availability of high-power pump sources:**

An element of great importance, which is closely linked to the setup, is a suitable pump source. It is well known that the opportunity of power scaling fiber lasers is closely linked to the availability of high-power pump sources, still exhibiting reasonable brightness.

Semiconductor laser diodes with multi-mode output have proven to perfectly fulfill these requirements while maintaining a relatively good electro-optical efficiency, weight and size, and output power delivered by a small NA fiber [81–84]. High-power versions of these diodes are only available for limited emission wavelengths, restricting the pumping schemes and the usability of some active ions.

- **Material absorption, damage thresholds, and adequate cooling:**

Increasing laser systems' output power or intensity entails several requirements about material choice, material purity, (surface) damage threshold, and more. Even low absorption in components can seriously impact the laser performance when operated at high output powers. The accumulated absorption can lead to thermal effects like thermal lensing, end face bulging, or even critical failure due to insufficient cooling. Thus, careful selection of fiber components through characterization and testing is necessary. However, not all components are available on the market. Among others, fiber end caps are crucial components for high-power fiber lasers, enabling safe in- and outcoupling of laser radiation. Section 3.2 deals with the theory, the processing, and the improvements of fiber end caps.

- **Ensuring good component performance:**

The installed optical components must work appropriately according to their purpose to ensure good laser performance. However, with ongoing power scaling, it is much more challenging to implement the fundamental ABCs of optics. For example, by increasing the output power of the pump diode lasers, which is a necessary step for power scaling, the numerical aperture and/or the core diameter of the pump delivery fiber has to be increased. This is a problem for the efficiency of pump combiners in all-in fiber laser setups but also creates problems for free-space laser setups. The in- and outcoupling of the laser radiation (signal and pump radiation) into a fiber and the effects of low coupling are discussed in Section 3.3. It has turned out that the difficulties in correctly coupling the laser radiation with the fiber also translate into an inefficient operation of optical components, like AOM, cavity mirror, and gratings. Different methods are investigated to ensure good coupling efficiencies.

All of the aspects mentioned above are taken into account in this chapter. Special focus is put on the fiber design itself, fiber end caps, and fiber optic coupling, which are discussed in the following in detail. The findings, methods, and improvements, which are presented, lay the basis for the experimental results in the upcoming chapters.

## 3.1 Fiber Architecture and Setup Scheme

### 3.1.1 Fiber Architecture

HDF lasers have shown to emit very efficiently above  $2\ \mu\text{m}$ . Incorporated into silica-glass fibers, trivalent holmium ions show a broad emission spectrum from  $2\ \mu\text{m}$  to beyond  $2.1\ \mu\text{m}$  [28]. For an efficient operation at these wavelengths, HDFs are usually in-band pumped by TDFs [27]. In order to minimize laser system complexity, THF lasers are preferred, as they can be directly diode-pumped at around  $79\text{X}\ \text{nm}$ , exploiting a direct ion-ion energy transfer between thulium and holmium ions [85]. Due to the resulting compactness, this fiber type is highly promising and is investigated in this thesis.

However, generating high output power in THF lasers is challenging as the heat load of the active fiber is significantly higher compared to singly HDFs. Therefore, the fiber polymer sees a lot of heat, which can lead to the degradation and browning of the polymer. Typically, in a double-clad fiber, the polymer is used as a second cladding and has not only mechanical but also guiding properties. This means the polymer is in direct contact with the pump radiation. Under normal conditions, the polymer is not absorptive for the  $79\text{X}\ \text{nm}$  radiation, but due to appearing brown and dark areas, the pump radiation will be absorbed. This leads to additional polymer degradation and, in return, again to an increased absorption, climaxing in a run-away effect and critical fiber damage. An exemplary picture of polymer darkening is shown in Fig. 3.1. To avoid this kind of fiber damage, a  $\text{Tm}^{3+}:\text{Ho}^{3+}$ -codoped triple-clad fiber (THTF) has been designed with an additional cladding consisting of glass. This second cladding shields the polymer from intense pump radiation and even allows small polymer degradation due to insufficient cooling without critical fiber failure. In addition, bad fiber injection of the signal and scattering at fiber-to-fiber splices increase the probability of critical fiber damage since the polymer is highly absorptive for the  $2\ \mu\text{m}$  signal. As a side effect, the second glass cladding also shields the polymer from unwanted  $2\ \mu\text{m}$  radiation propagating in the first cladding. A representative of the triple-clad fibers (TCFs) is depicted in Fig. 3.2. The TCFs comprise multiple fiber concepts, which are presented and described in Chapter 2. The fibers are designed as an LMA fiber to decrease fiber nonlinearities, especially in pulsed operation. Due to the high doping concentrations with  $\text{Tm}^{3+}$ ,  $\text{Ho}^{3+}$ , and  $\text{Al}^{3+}$ , the fiber is equipped with a pedestal to realize the guiding of only a few modes. The fiber is also a PANDA-type fiber to enable a linearly polarized laser output, essential for pumping a nonlinear crystal.

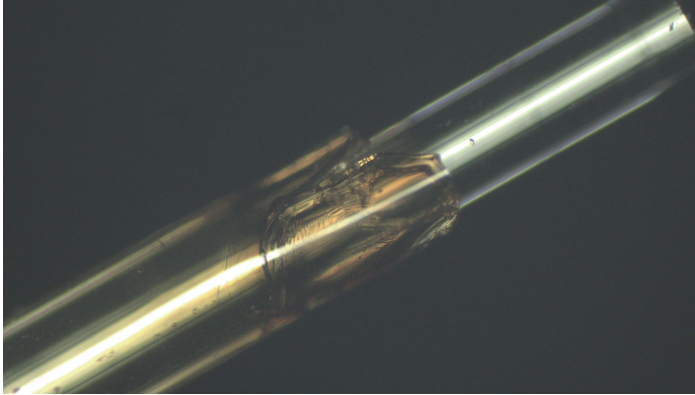


Figure 3.1: Symbolic picture of polymer darkening. The standard fiber polymer coating can only stand a certain temperature for long-term laser operation. With increasing laser operation time, the fiber polymer starts to get brownish.

One of the two TCFs under investigation has a  $20\ \mu\text{m}$  core diameter, a first silica cladding with a diameter of  $300\ \mu\text{m}$ , and a cladding NA of 0.22. This is a core-to-cladding ratio of 1:15. The core is surrounded by a pedestal, ensuring a small NA of 0.09. Assuming a pure step-index fiber, this leads to a V-number of 2.643 at a wavelength of  $2.1\ \mu\text{m}$  and shows that the fiber is slightly multi-mode. The second cladding consists of fluorinated glass and has a diameter of  $330\ \mu\text{m}$  and an NA of  $> 0.46$ . The second cladding is surrounded by a low-index polymer coating (third cladding) with a diameter of  $490\ \mu\text{m}$ .

A second fiber is investigated to ensure a closer to single-mode behavior. The fiber manufacturer has drawn a similar fiber from the preform but with a smaller core diameter of  $18\ \mu\text{m}$ . The whole fiber architecture, which consists of glass, is therefore multiplied by a factor of  $9/10$ , leading to an  $18/270/297\ \mu\text{m}$  fiber. The polymer diameter remains unchanged. This fiber is depicted in Fig. 3.2. By drawing the fiber to a smaller extent, the V-number is reduced to 2.424, being close to a single-mode operation. The  $20\ \mu\text{m}$  core fiber should show a small advantage in terms of nonlinearities and possible achievable pulse energies due to a slightly larger mode field diameter but also higher probabilities for guiding modes other than the  $LP_{01}$ .



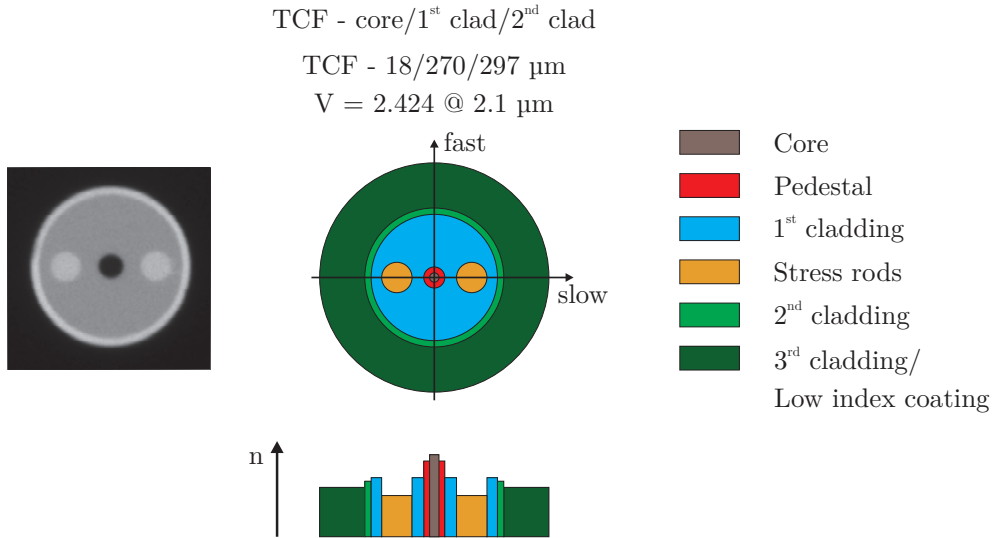


Figure 3.2: Two THF are under investigation, based on a triple-clad PANDA-type fiber geometry. As a representative, the LMA fiber with an 18  $\mu\text{m}$  core size is depicted. The left-hand side shows an end view of the TCF, and the right-hand side shows the according schematic.

### 3.1.2 Setup Scheme

The TCFs are the central element of the fiber laser and are integrated into a free-space single-oscillator fiber laser setup. This kind of setup is per se not a setup for high-power laser operation since increasing laser power and the consequent heating of components leads to a necessary continuous re-aligning process of mirrors and lenses. For pure power scaling, a more integrated, all-fiber version must be considered if the according components would be available. However, the setup under investigation is a typical fiber bench used for characterizing new types of fibers, like the THTF. Due to the simplicity of the setup, the most accurate values for slope efficiencies and potential pulse energies can be generated. A basic laser setup is sketched in Fig. 3.3. This setup scheme describes only the essential parts of the setup, which are investigated within this chapter to get the laser ready for power scaling. 79X nm pump diode lasers are used to pump the active THF. This radiation is collimated, redirected by dichroic mirrors, and coupled into the fiber. For collimation and coupling, identical lenses are used, having roughly an effective focal length of 15 mm. End caps are spliced onto the fiber to ensure the integrity of the fiber ends for high-power, high-energy operation.

The fiber is temperature controlled by a tempered water basin. This setup scheme is fundamental to all free-space fiber lasers realized in this thesis. The optics, which are left out in this scheme and come into contact with the laser signal, are responsible for controlling the laser operation. The setup needs to be finalized in every upcoming chapter since different optical components are used and interchanged.

One advantage of the setup is the possibility of realizing different laser operation modes as randomly polarized/linearly polarized, wavelength-fixed/tunable, and CW/pulsed by simply changing one or two components. This huge flexibility in changing different components makes this setup an ideal research setup.

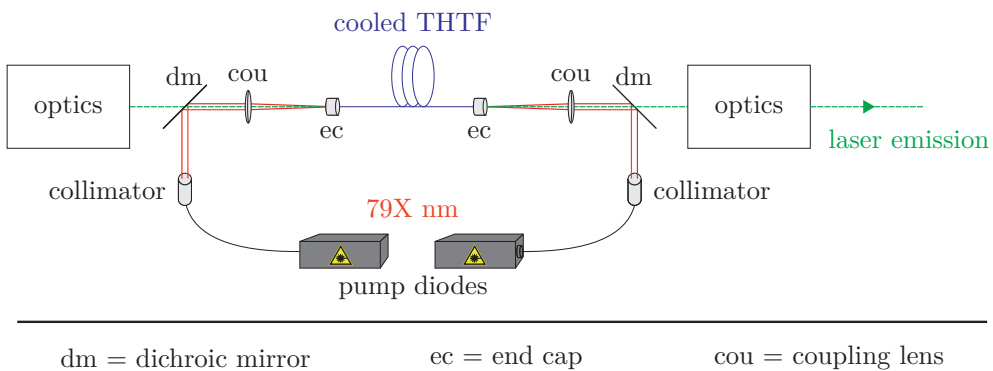


Figure 3.3: Fundamental laser setup for every free-space single-oscillator used within this thesis. The optics not comprised in this scheme are specified at the beginning of each chapter since they determine the exact laser operation.

## 3.2 Fiber End Face Preparation

### 3.2.1 Theory of Fiber End Caps

Fiber end face assembly plays an increasingly important role in fiber laser optics, and especially fiber end caps are indispensable components enabling high-power and high-energy laser output as well as extremely low back-reflection into the fiber core [86, 87]. Fiber end caps come in various shapes, optimized for the specific intended application.

As a result of increasing fiber laser power and pulse energies confined in single or few-mode fibers, immense intensities and fluences are propagating through the waveguide. Whereas the bulk material's laser-induced damage threshold is typically not reached within transparent media, the laser-induced damage threshold for the fiber end faces can be reduced dramatically [88, 89]. Submicroscopic cracks on dielectric surfaces cannot be avoided and are even present in well-controlled laboratory environments, decreasing the surface damage threshold compared to bulk material by a factor of 2 [90]. In case of additional contamination and a dirty environment, the damage threshold can decrease by several orders of magnitude. In addition, the high (average) laser output power densities can lead to scorching of the fiber ends. Surface imperfections and a dirty environment can act as a spark, igniting irreversible fiber end face damage. A bulk piece of glass is typically fixed onto the fiber end to overcome this problem [91]. This so-called end cap allows the beam to expand within the bulk glass and decisively reduce the intensity, leading to a non-critical value at the end cap to air interface.

End caps are used in master oscillator power amplifier (MOPA) systems to decouple the intense signal out of the fiber and reduce the risk of fiber end face damage. The left part in Fig. 3.4 shows a simple standard assembly, where a fiber is spliced onto a coreless fiber (a diameter-matched piece of glass) [92, 93]. The signal can expand within the coreless fiber leading to a decrease in intensity. In this configuration, the signal radiation can propagate a few millimeters without being clipped by the outer surface. Exact values depend on the diameter of the fiber and the NA of the signal, which is guided in the core. The left-hand side of Fig. 3.5 shows the beam diameter and the peak intensity of a Gaussian beam ( $P=1$  kW) while propagating inside of an end cap. The end cap is 2 mm long, and the fiber mode field diameter is  $20\ \mu\text{m}$ . The beam expands to  $180\ \mu\text{m}$  within the end cap. This leads to a drop in intensity by a factor of 81.

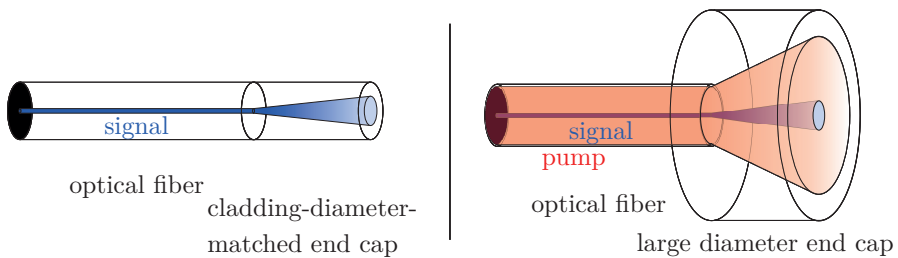


Figure 3.4: Simple standard end cap versions for avoiding critical surface damage. Left: Outcoupling of signal radiation (low NA and small mode field diameter) out of a cladding-diameter-matched fiber endcap. Right: Coupling of signal and coupling of pump radiation (high NA and large mode field diameter) with a large diameter end cap.

For high-power free-space single-oscillators and special pumping configurations of master oscillator power amplifier (MOPA) systems, the pump radiation also needs to pass the end cap. Due to the larger NA and a larger mode field diameter of the pump radiation, a cladding-diameter-matched end cap is no longer applicable. In this case, a large diameter end cap is used (Fig. 3.4 right part). This strong asymmetry in bulk material size, which needs to be joined, can harm the optical laser characteristics, as discussed later. Besides the increase of the fiber end face damage threshold, fiber end caps are also powerful components in the low power regime concerning a low feedback fiber termination [87].

A straight fiber end cleave works like a 3 % reflector for the light propagating in the fiber due to the Fresnel reflections at the fiber interface from glass to air. Therefore, a straight fiber end is typically used as an output coupler for fiber lasers. Conversely, a fiber is typically cleaved at  $8^\circ$  to suppress this reflection. In this case, the Fresnel reflections are not dramatically decreased. However, the angled cleave creates a mode field mismatch of the forward propagating and reflected signal, decreasing the back reflection up to 60 dB [94]. Fiber end caps can create similar back reflection. In contrast to the cleaved angle fiber termination, the reflection at the glass-to-air interface is completely propagating back to the fiber. However, due to the expanding beam, only a small fraction of light is coupled back into the fiber core. In addition, the end caps are typically AR-coated at the glass-to-air interface to reduce the portion of reflected radiation even further. Last but not least, due to the large scale and the large end face of the end cap, manipulating and cleaning are additional benefits of up-scaling the end cap.

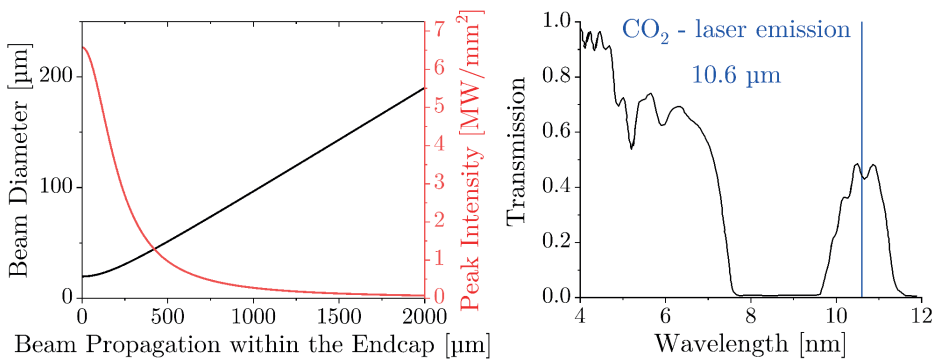


Figure 3.5: Left: Expanding beam diameter and corresponding peak intensity of a Gaussian beam with respect to the propagation distance within an end cap. Right: Transmission spectrum of a 26  $\mu\text{m}$  fused silica sample. Data from [95].

To sum up, a reasonable fiber end termination is a powerful component for realizing high-power and high-energy fiber amplifiers and fiber lasers, effectively suppressing ASE and parasitic lasing, and improving the tunability and pulse energy scaling in Q-switched laser operation.

### 3.2.2 Splicing of Fiber End Caps

Joining two fibers or a fiber to an end cap is referred to as splicing. In the ideal case, a splice is a permanent, low-loss, high-strength welded joint between two optical components [96]. For splicing fibers and end caps, the components need to heat up to a temperature of 1800 to 2000 °C depending on the glass, doping material, and doping concentration. Different types of heat sources are currently used in splicing machines, like an electric arc discharge, an oxy-hydrogen flame, a tungsten or carbon filament heater, or a CO<sub>2</sub> laser. Among these sources, heating by electric arc discharge is one of the most common methods and is well-implemented in standard machines.

However, heating by electrical discharge also shows significant disadvantages regarding adequate heating of large fiber components. Therefore, over the last years, CO<sub>2</sub> laser splicing has been used for large diameter fibers with its advantages of heating fibers and components directly by radiation, contamination-free processing, and broad flexibility in forming and directing the laser beam. The right-hand side of Fig. 3.5 shows the transmission of optical radiation in the wavelength range of 4 to 12 μm through a 26 μm thick piece of fused silica [95]. The CO<sub>2</sub> laser emission wavelength of 10.6 μm is emphasized in blue. The strong absorption of around 50 % within 26 μm indicates a strong surface heating. This intense surface heating is even enhanced when the absorbed radiation of the splicer heats the glass since the extinction coefficient is strongly dependent on the temperature. Increasing the temperature of glass from room temperature up to 1800 °C is decreasing the penetration depth from 34 μm down to 4 μm [95]. The bulk material itself is then heated by conduction.

For splicing end caps, a commercially available CO<sub>2</sub> laser splicer is used, holding the fiber and end cap in a vertical manner. A ring-shaped geometry of the laser radiation is used to heat the joining area of the fiber and the end cap homogeneously. Figure 3.6 visualizes the initial pre-implemented fiber to end cap splicing procedure of the splicing machine.

## Splicing Description

The foundation of a successful splice is a good preparation in terms of well-cleaned components and a flat and damage-free fiber cleave ( $< 0.5^\circ$ ). The splicing procedure itself is based on common instructions for fiber-to-fiber splices [96], slightly adapted for splicing fiber end caps [91]:

**Step 1:** Fiber and end cap are brought into contact at the correct height for pre-heating the end cap. Due to the large amount of energy needed to sufficiently pre-heat the end cap, critical damage can occur where the cone hits the surface. This needs to be taken into account.

**Step 2:** The fiber is completely removed from the end cap, ensuring no fiber damage due to the pre-heating. The thermal radiation from the heating area of the end cap and the reflections of the  $\text{CO}_2$  radiation are strong enough to immediately heat the fiber to such an extent forming a ball lens when the fiber is too close to the end cap.

**Step 3:** The end cap is pre-heated. Despite the very local energy deposition, a large volume of the end cap is heated up due to thermal conduction. Reaching an acceptable local splicing temperature at the actual splicing area requires roughly 4 to 5 times the energy needed for fiber-to-fiber splicing.

**Step 4:** The fiber is brought again into contact with the end cap. The laser power needs to be lowered again to an amount being not harmful to the fiber due to Fresnel reflection.

**Step 5:** The fiber and end cap, more precisely the splicing area, are now moved down into the tip of the radiation cone.

**Step 6:** As a last step, the so-called hot-push is performed. Being both at the splicing temperature, the fiber is pushed several micrometers into the end cap, resulting in a strong connection.

The exact splicing parameters depend on the required application of the fiber end cap. In principle, it can be distinguished between two kinds of splices. Using a minimum amount of energy to form the joint is referred to as *cold splicing* [15]. In this case, the optical properties are preserved. However, the splice lacks mechanical stability. In addition, there is an almost step-index behavior of the refractive index of the core to the refractive index of the end cap glass, which leads to Fresnel reflection of about -45 dB [15]. To decrease the reflection at the interface and smear out the step-index behavior, a larger amount of energy can be used to join the fiber and end cap. This so-called *hot splice* is creating a strong diffusion. While the mechanical stability is improved, the optical properties are impaired.

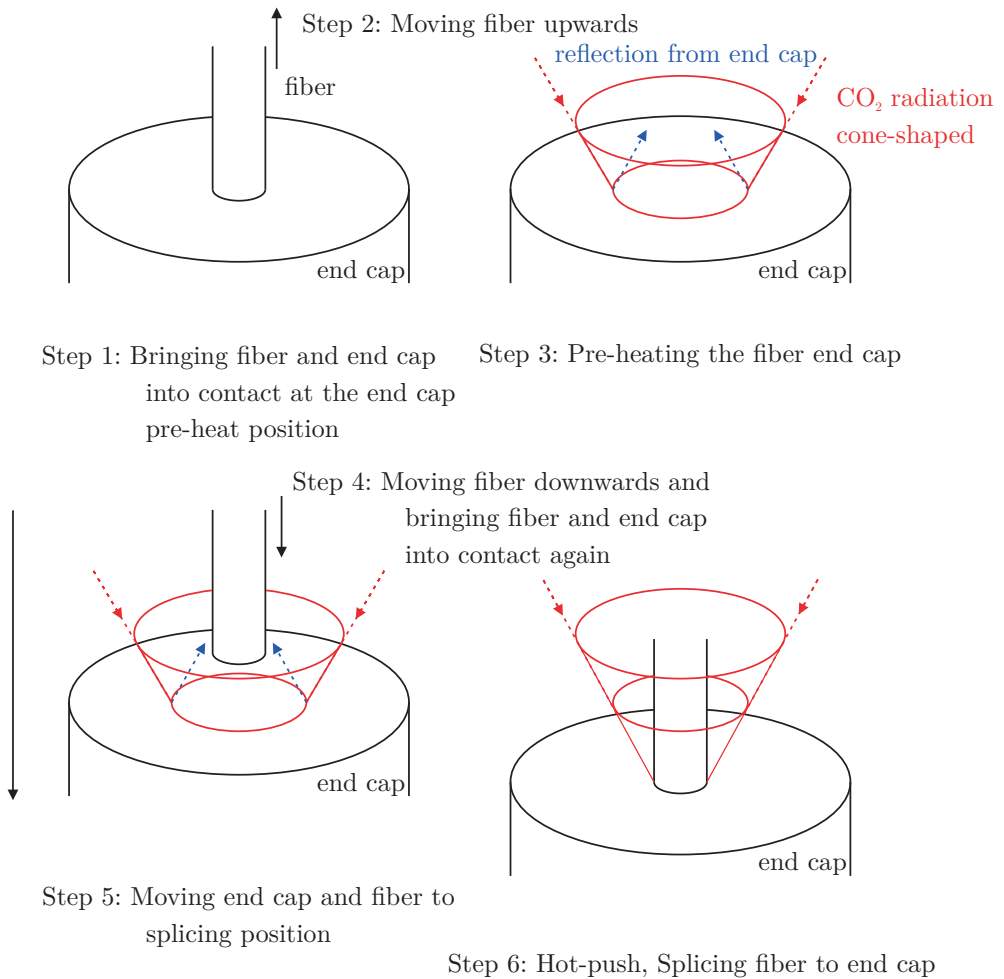


Figure 3.6: Illustration of a fiber to end cap splice pre-implemented in the splicing machine. Within six steps, a fiber can be spliced to an end cap. A vertical CO<sub>2</sub> splicing machine is used, providing a radiation cone.

### Drawbacks and Problems:

The described splicing procedure works perfectly for splicing MMFs [97] or passive fibers directly on the end cap. However, when it comes to splicing active LMA fibers on a large end cap, a few drawbacks of this kind of splicing are dramatically decreasing the splicing quality. The importance of well-optimized fiber-to-fiber splices is well known and already reported by several authors [98–100].

Strong diffusion, mainly for the heavily doped active fiber core, leads to impaired optical laser characteristics. Figure 3.7 shows a well-optimized splice of an active fiber to a large diameter end cap and the resulting beam profile. The side inspection shows no deformation of the fiber, and a small weld at the outer fiber to the end cap border indicates a good splice in terms of mechanical strength. However, investigating and illuminating the splice from the bottom indicates strong diffusion at the end of the active fiber side. For example, the non-guiding stress rods show strong diffusion effects at the outer surfaces and therefore feature scattering of the illumination light. Scattering at the fiber splicing area leads to coupling into higher order and pedestal modes, worsening beam quality. The figure depicting the beam profile shows strong scattering and crescent power distributions around the Gaussian modal profile. A strong deformation of the refractive index profile of the fiber at the splice interface can also lead to a distortion of the phase front, reduced interaction efficiency with free-space components, and bad re-incoupling into the fiber. The core diffusion seriously impacts end-capped fiber single-oscillators, where the signal is coupled multiple times through the splice.

One drawback of the splicing method described in 3.2.2 is the insufficient pre-heating of the fiber, which is almost cold when it comes into contact with the active fiber. Another disadvantage is the large amount of energy that is used during the hot-push. Both are a direct consequence of the large size of the end cap.

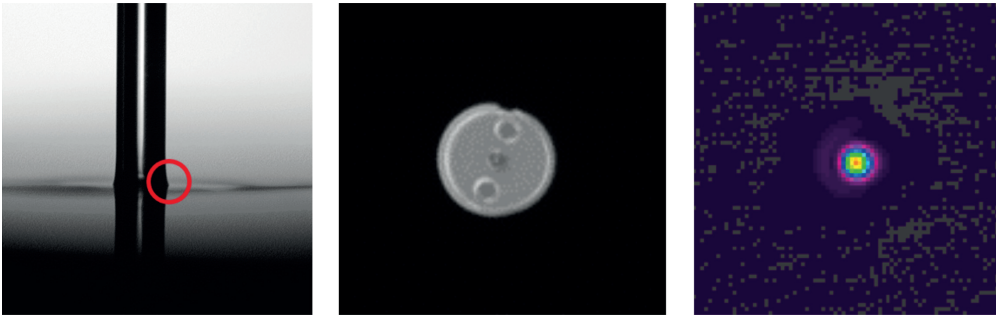


Figure 3.7: Analysis of an optimized splice between an active fiber and a large volume end cap. The side view on the left-hand side indicates a well-optimized splice with no deformation of the active fiber. Illuminating the end face of the fiber through the end cap indicates a large amount of diffusion. The right-hand side shows the diffusion effects on the laser beam quality with a lot of power features around the Gaussian-like beam.



### 3.2.3 End Cap Optimization

In this thesis, different options are tested to improve the fiber to end cap splicing and reduce the strong diffusion effect while maintaining mechanical stability. The first investigated option is decoupling the power-sensitive splice of the active fiber from the high-power splice with the end cap. Secondly, a method is investigated to reshape the end cap, resulting in improved and non-critical splicing parameters. Before designing one of these end cap configurations, the beam propagation within the end cap after leaving the fiber must be determined. This allows conclusions on possible fiber end terminations without clipping the radiation. A Gaussian beam is assumed if only the signal can be considered. Based on a step-index single-mode fiber, the mode field radius of the signal can be calculated according to Marcuse [101, 102]:

$$\frac{\omega_0}{a} = 0.65 + \frac{1.619}{V^{3/2}} + \frac{2.879}{V^6}. \quad (3.1)$$

Inserting the fiber core radius  $a$  and the normalized frequency  $V$  of the single-mode fiber into this empirical formula, the mode field radius can be used as a starting point for the Gaussian beam waist  $\omega_0$  for Gaussian beam propagation [103]:

$$\omega(z) = \omega_0 \sqrt{1 + \left( \frac{z \lambda M^2}{\pi \omega_0^2 n_{ec}} \right)^2}. \quad (3.2)$$

The beam radius  $\omega$  is the  $1/e^2$ -intensity radius of the field. The subscript  $ec$  refers to the values of the end cap. These formulas can be used to calculate the most suitable length of a diameter-matched end cap.

When the pump radiation needs to be included as well, a geometrical optics approach is used:

$$r_{pump}(z) = r_{clad} + \tan(\theta_{ec}) \cdot z = r_{clad} + \tan\left(\arcsin\left(\frac{NA_{clad}}{n_{ec}}\right)\right) \cdot z \quad (3.3)$$

This equation can be derived from Fig. 2.1. In contrast to a Gaussian beam, the NA of MMFs refers to a far-field angular intensity reduction of 5 %.

### Fiber assembly

One method to reduce heavy diffusion at the end of the active fiber is decoupling the power-intensive splice of the end cap with the splice of the active fiber as shown for pure signal coupling [93]. A MMF or a pure silica rod with a larger diameter than the outer cladding of the active fiber can be spliced in between. The diameter and length of the intermediate piece are chosen to avoid clipping the pump radiation. Therefore, Eq. (3.3) is utilized to monitor the beam propagation of the pump radiation. The first splice of the active fiber to the intermediate piece is relatively uncritical. Nevertheless, the splice must be optimized well to withstand damage by cleaving the intermediate piece in a second step. In the end, both fibers are spliced to the end cap. Since the active fiber is not directly located at the splicing spot, higher energies can be used to form a joint between the intermediate piece and the end cap. As a result, the active fiber sees a reduced amount of diffusion. A scheme of this fiber assembly is displayed in Fig. 3.8.

### End Cap Reshaping

The fiber assembly method results in good optical properties. However, it does not only need a lot of steps and time to perform this alternative solution but also requires much time to optimize beforehand. A less time-consuming method is to use a reshaped end cap to guarantee a minimum amount of glass at the splicing area. This principle is depicted in Fig. 3.9.

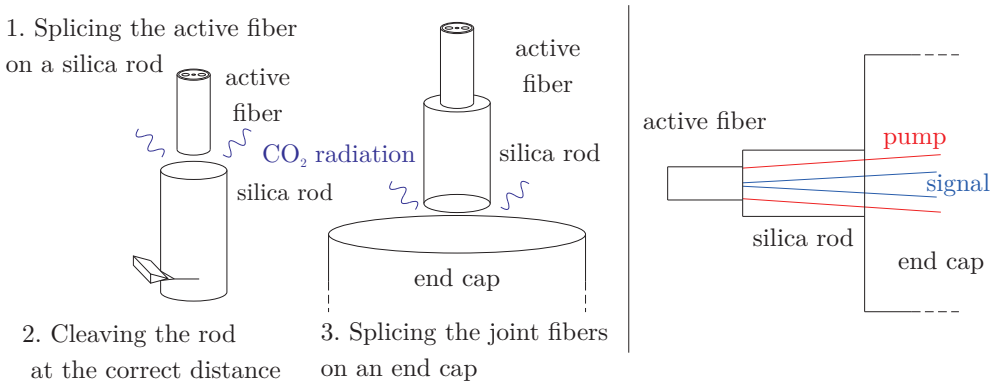


Figure 3.8: Scheme of an alternative fiber to end cap splice by splicing a silica rod in between. The active fiber can be spliced to this piece of glass without diffusion. Afterward, the rod is spliced to a large volume end cap.

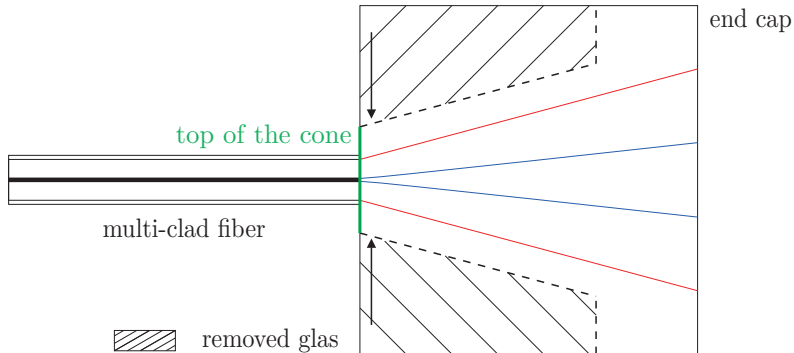


Figure 3.9: Schematic of a fiber end cap, which is optimized to provide a minimum amount of glass at the splicing area but still ensures that all the radiation is inside the end cap.

Again, Eq. (3.3) is utilized to find the propagation of the beam inside the end cap, and all unnecessary glass, especially next to the splicing area, is removed. One advantage is the small penetration depth of the  $\text{CO}_2$  radiation of the splicer. Here, the tip of the cone can be heated very efficiently. Compared to the full-volume end cap, the heat conduction inside the glass is almost reduced from three- to one-dimensional and prevents the heat sink effect of the end cap.

### Improvements and Discussion

In summary, two methods have been developed to improve an active fiber to large end cap splice. Disturbing diffusion effects are minimized by either splicing an intermediate piece of glass or reshaping the endcap. The left-hand side of Fig. 3.10 shows the fiber spliced to an end cap, observed through the end cap. The stress rod parts close to the border of the second cladding show a minimum amount of diffusion, which is indicated by a slightly bright crescent. Compared to Fig. 3.7, the inner parts of the fiber do not show noticeable diffusion effects. This is proven by analyzing the laser output transverse intensity distribution. No scattering effects or crescent power distribution around the main Gaussian-like beam profile are visible.

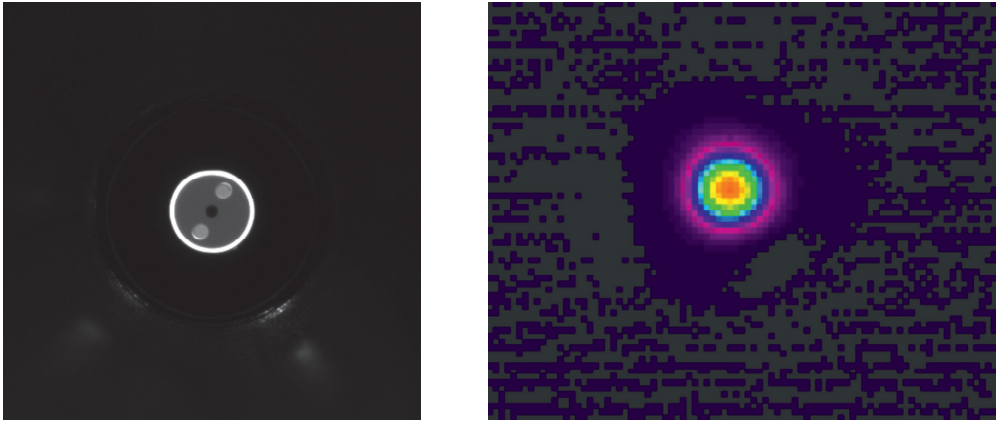


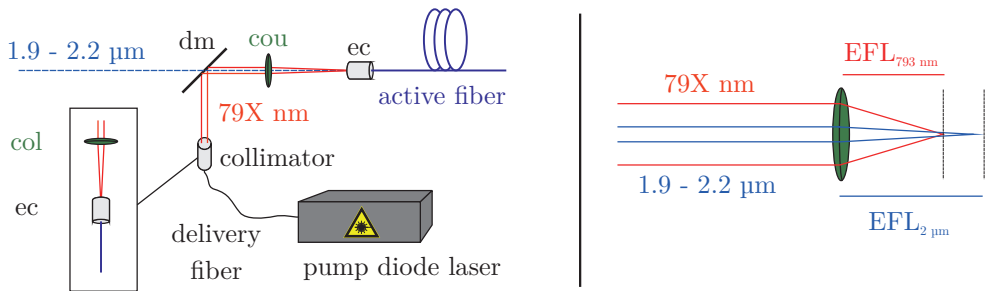
Figure 3.10: Left-hand side shows a fiber end face after splicing with either fiber assembly or end cap reshaping. Diffusion at the fiber end face is reduced to a minimum. The right-hand side shows the laser output beam with an improved endcap design.

### 3.3 Pump and Signal - Fiber Coupling

#### 3.3.1 Coupling Issues due to Chromatic Abberations

When developing a high-power laser setup, the pump power needs to be increased. In terms of THF lasers, this is equivalent to integrating more powerful diode lasers emitting at 79X nm. Typically, increasing the output power of the diode lasers comes with an increase of the NA and/or the core size  $\varnothing_{\text{core}}$  of the delivery fiber.

The left-hand side of Fig. 3.11 shows the setup part under investigation. The coupling scheme shown is one of the simplest but also one of the most compact setups that can be used in a free-space single-oscillator. The pump radiation out of a delivery fiber is collimated by a lens at a certain distance, according to the NA of the lens and the fiber. Then, the 79X nm radiation is redirected by a dichroic mirror, highly reflective for the 79X nm radiation. In the last step, the pump is focused on the first cladding of a multi-clad fiber (MCF), e.g., the THTF with a core/1<sup>st</sup> cladding/2<sup>nd</sup> cladding diameter of 18/270/279  $\mu\text{m}$  or 20/300/330  $\mu\text{m}$ . In addition, the signal, which is transmitted through the dichroic mirror, has to be coupled mode-matched into the core of the active fiber using the same coupling lens as for the pump radiation.



low-power setup:  $NA = 0.22$ ,  $\varnothing_{\text{Core}} = 105 \mu\text{m}$

high-power setup:  $NA = 0.22/0.46$ ,  $\varnothing_{\text{Core}} = 200 \mu\text{m}$

ec = end cap

dm = dichroic mirror

col = collimation lens

cou = coupling lens

Figure 3.11: The left-hand side shows the part of the setup under investigation. Increasing pump power is often connected with more difficulties in coupling this radiation in the active fiber. One problem, the chromatic dispersion, is visualized on the right-hand side of this figure.

One difficulty is the simultaneous efficient coupling of pump and laser radiation into the active fiber since insufficient coupling has a major influence on the laser performance, as will be discussed later.

Starting from a low-power laser setup with around 30 W of pump power per diode laser, having an NA of 0.22 and a core diameter  $\varnothing_{\text{core}}$  of 105  $\mu\text{m}$  for the delivery fiber, the simultaneous coupling of signal and pump radiation via the coupling lens is no problem. Switching towards more pump power, the diameter of the pump delivery fiber is increased to 200  $\mu\text{m}$ , and insufficient coupling can be observed by a drop of efficiency related to the launched pump power and substantial leakage of pump radiation at the end of the fiber. The pump radiation undergoes a one-to-one imaging from the delivery fiber on the active fiber and, therefore, should couple perfectly into the first cladding of the TCF.

The major problem for the bad incoupling of the pump radiation, or in general the reason for the impossible simultaneous incoupling of signal and pump radiation, is the material dispersion of the coupling lens. This so-called chromatic aberration [104] is exaggeratedly displayed on the right-hand side of Fig. 3.11. The focal distance of the pump radiation (79X nm) is much shorter than for the signal radiation (1.9 to 2.2  $\mu\text{m}$ ).

This means that if the coupling lens is placed at a distance from the active fiber which equals the focal length of the signal radiation, the pump radiation already went through its focal point and is diverging again.

Figure 3.12 shows dispersion-related focal distance shifts, which are determined by the software OpticStudio from Zemax [105]. The relative distance is defined from the back of the lens to the focal spot. This relative distance for the pump radiation of 79X nm is  $\sim 15.3$  mm and 14.02 to 14.18 mm for signal wavelengths from 1900 to 2200 nm. The lens is advertised with a focal length of 15 mm. There is already a large difference in focal length from 1900 to 2200 nm, indicating a lower relevance on the laser operation for purely  $\text{Tm}^{3+}$ -doped free-space single-oscillators emitting mainly around  $2.0\ \mu\text{m}$  compared to THF lasers dedicated to emit beyond  $2.1\ \mu\text{m}$ . This difference in focal length is no problem for a low-power setup. Due to the one-to-one imaging of the small diameter delivery fiber, the pump radiation can diverge again and still match the first cladding of the active fiber.

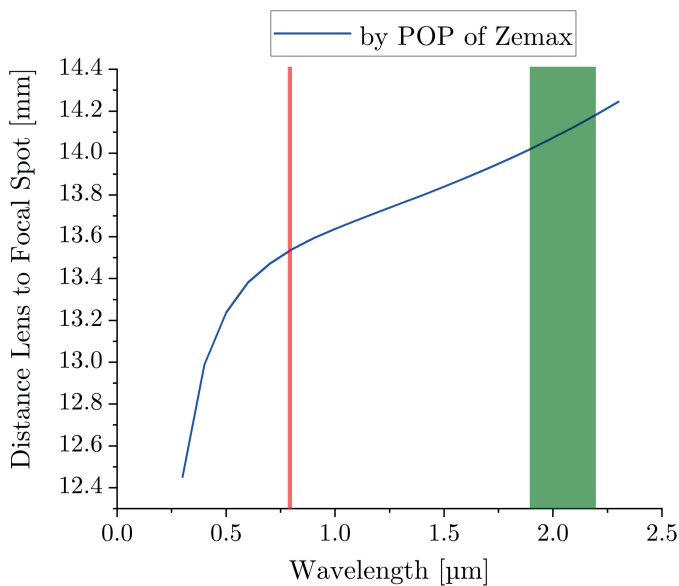


Figure 3.12: Distance from a coupling lens to the focal spot as a function of the wavelength of the beam. There is a strong mismatch between the pump (red window) and signal (green window) radiation as a result of the chromatic dispersion of the lens material.

However, for a higher-power setup, where the core diameter of the pump delivery fiber is almost the size of the first cladding of the active fiber, actions have to be taken to compensate for this mismatch in focal length. The detrimental effects of this difference in focal lengths are discussed briefly in the following section, followed by two methods to simultaneously achieve good incoupling for pump and signal radiation.

### 3.3.2 Impacts of Non-Correct Fiber Coupling

When the laser system visualized in Fig. 3.3 is not compensated for the chromatic dispersion in the coupling lens, the laser performance is negatively impacted. To discuss these influences a bit more in detail, the impact of not ideal signal and not ideal pump coupling are discussed separately.

Placing the coupling lens correctly for the signal radiation, the optical characteristics of the fiber laser are not impacted. However, the efficiency of the laser is dramatically lowered since only a fraction of the available pump power is incoupled. This situation is simulated in the non-sequential mode of OpticStudio to get an idea of the amount of pump radiation that is not coupled to the fiber.

First, the 79X nm pump radiation is modeled. As discussed in Chapter 2, MMFs and multi-mode radiation are accurately described by ray optics. Therefore, the non-sequential mode is well-suited to investigate the pump coupling into a fiber. A field of diodes emitting within an angle of  $12^\circ$  is used as a primary light source. This radiation is directly launched into an optical fiber, similar to the one used in the experiment, with a core NA of 0.22. Then, the fiber is bent and twisted several times to reach a good scrambling and a realistic intensity distribution. At the end of the fiber, the rays are refracted at the fiber/glass to air interface and propagate towards a collimation lens.

The same collimating lens as in the lab, having roughly an effective focal length of 15 mm, is modeled. The collimated ray bundle propagates towards a coupling lens identical to the collimation lens, bridging a free-space distance of 100 mm. Behind the coupling lens, a fiber is placed, which resembles the active fibers under investigation. The distance from the lens to the active fiber  $d_{LF}$ , a relative distance to the actual focal length, is wavelength dependent and is taken from Fig. 3.12. Table 3.1 shows the distance  $d_{LF}$  for various signal wavelengths and the corresponding coupling efficiency of the pump radiation into the active fiber.

Table 3.1: This table shows the distances  $d_{FL}$  from the coupling lens to the focal spot in dependence of the signal wavelength. The coupling efficiency of the pump radiation into the active fiber is displayed for the correct active fiber position related to various signal wavelengths. Under investigation are the coupling into the 1<sup>st</sup> and 2<sup>nd</sup> cladding of the TCFs. (TCF1: 18/270/ $\sim$  300  $\mu\text{m}$  and TCF2: 20/300/330  $\mu\text{m}$ )

Wavelength Signal [nm]	793	1900	1950	2000	2050	2100	2150	2200
Distance $d_{LF}$ [mm]	13.53	14.022	14.048	14.074	14.101	14.128	14.157	14.247
$\varnothing = 270 \mu\text{m}$	100 %	79 %	77 %	74 %	71 %	69 %	66 %	58 %
$\varnothing = 300 \mu\text{m}$	100 %	87 %	85 %	82 %	80 %	77 %	75 %	67 %
$\varnothing = 330 \mu\text{m}$	100 %	93 %	91 %	89 %	87 %	85 %	82 %	75 %

The table displays the fraction of energy coupled into the 1<sup>st</sup> and 2<sup>nd</sup> cladding of the TCF fibers (270  $\mu\text{m}$ /279  $\mu\text{m}$  and 300  $\mu\text{m}$ /330  $\mu\text{m}$ ). The fraction of rays coupled into the fiber decreases with increasing signal wavelength since the distance  $d_{LF}$  increases. The pump radiation is supposed to couple into the first cladding of the TCF. The determined values show that it is far from a good incoupling. At the target wavelengths from 2.1 to 2.2  $\mu\text{m}$ , less than 70 % are coupled into the first cladding of the 18  $\mu\text{m}$  core TCF.

In a second scenario, the distance between the coupling lens and the fiber is chosen to ensure a good coupling for the pump wavelength. This distance is more variable since a good pump incoupling of the 200  $\mu\text{m}$  delivery fiber onto a slightly larger cladding area does not require placing the active fiber directly in the focus of a one-to-one imaging. Nevertheless, the signal radiation is not coupled well enough by the coupling lens, since the lens is placed too close to the fiber. Starting from the fundamental fiber mode propagating inside the fiber, the approximately Gaussian beam is launched towards the coupling lens. Due to the misplacement of the lens, the signal is not collimated but still diverging. This means that the signal cannot interact correctly with optical components like polarizers, an AOM, or cavity mirrors.

In addition, the signal needs to be coupled back into the fiber. To achieve a good laser performance, there must be a good mode overlap between the back-coupled field and the fundamental mode. Because of the diverging signal, the back-coupled field is not mode-matched. This leads to increased losses but also features the excitation of higher-order or pedestal modes, which deteriorates the beam quality. Therefore, by a misplacement of the coupling lens for the signal, not only the efficiency of the laser is impaired but also the laser beam quality.



During the experiment, the coupling lens is not placed like in one of the discussed scenarios above since the setup is adjusted for the maximum output power. Neither the signal nor the pump radiation is correctly coupled in the active fiber because the lens is placed in an intermediate position. As a result, the optical laser characteristics, the laser efficiency, and the laser stability are impaired. Also, the fiber is prone to get damaged while power scaling the system. All these effects have been observed at the beginning and are briefly presented in the next chapter, together with the results of the improved setup.

### **3.3.3 Methods for Improved Fiber Coupling**

Different methods have been investigated for improving the simultaneous incoupling of the signal and pump radiation. However, the most common methods to compensate for dispersion effects in a coupling lens are dismissed. A typical solution to compensate for dispersion is achromatic lenses. Achromatic lenses consist of a set of two (doublet) or three (triplet) lenses, having different shapes (convex and concave) and consisting of different materials. There are, for example, achromatic triplets for improving the core coupling of tunable, in-band pumped HDF lasers [106]. These cover a wavelength range of around 300 nm. In the case of a 79X nm diode-pumped THF laser, the lens system needs to cover the pump wavelength at 79X nm as well as the wavelengths from 1900 to 2200 nm. In addition, due to high-power operation, gluing of the components would be prohibited, and materials are restricted to highly non-absorptive materials. Therefore, if possible, to design and develop such lenses, creating a corresponding doublet or triplet lens is complex and expensive.

Another method is avoiding the coupling of signal and pump through one lens by decoupling both types of radiations [107]. The dichroic mirror can be placed directly after the fiber, so separate lenses can be used for the signal and pump radiation. Due to an additional component between the lenses, the focal lengths of the lenses must be much larger, resulting in much larger beam diameters. This arrangement would be more complex in terms of adjustment and also reduces the compactness of the system. Therefore, the main task has been to develop simple and compact solutions to compensate for the achromatic dispersion.

### First method: Splicing a multi-mode fiber

One opportunity to couple signal and pump radiation in the active fiber by the same lens is to splice a MMF at the end of the active fiber. This scenario is depicted in Fig. 3.13. The core and the cladding size of the MMF equals the size of the first and second cladding of the TCF, respectively. Also, the core NA of the MMF needs to fit the numerical aperture of the second cladding of the TCF and the NA of the coupling lens. The end of the MMF is placed at the waist of the pump radiation. This multi-mode radiation is immediately guided by the fiber and coupled into the active fiber. The signal radiation is also coupled into the core of the MMF but does not undergo any guiding. This signal is refracted at the glass-to-air interface, focusing on the MMF-TCF interface. The length of the MMF is approximately 0.6 to 1 mm.

The advantage of this configuration is that this splice is not complex and can be easily performed without significant diffusion. In addition, this piece of fiber can already act as an intermediate fiber, easing the fiber end cap splicing, as described in Section 3.2.3. One problem is the availability of this kind of MMFs matching the claddings of the TCF. Therefore, this version is only of theoretical interest but is not realized due to the missing MMF.

### Second method: Non-collimated pump radiation

Another method to improve the incoupling of the pump radiation is to work with a non-collimated pump beam. This scenario is depicted in Fig. 3.14. By placing the collimation lens closer to the fiber end of the pump delivery fiber, the multi-mode pump radiation is not collimated but has a slight divergence. When this pump radiation hits the coupling lens, the focal length is slightly larger than in the case of a plane phase front hitting the coupling lens.

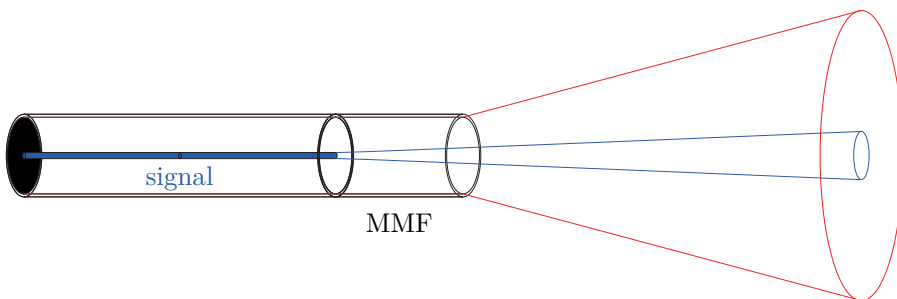


Figure 3.13: In order to compensate for the chromatic dispersion in the coupling lens, a MMF can be spliced in front of the active fiber. This MMF piece bridges the effective focal length difference. The signal and the pump radiation are coupled into the core of the active fiber and the MMF, respectively.

By this method, the focal spot of the 79X nm radiation can be shifted towards the focal spot of the signal. This shift of the focal spot comes with an increase in the waist. The simulation with OpticStudio shows that this method can couple 100% into the first cladding of the TCF in the system under investigation, and this is confirmed in the laboratory. This is an easy and fast method to improve the incoupling of the pump radiation when the signal coupling of the lens is set to its maximum firsthand.

There are also some potential disadvantages of this method. First, there could be a detrimental effect on the efficiency of coatings since there is no longer a plane phase front interaction with the optics like dichroic mirrors and the lenses. Second, the beam diameter increases while propagating from the collimation to the coupling lens. As a result, the beam could hit the aperture of the coupling lens. Nevertheless, working with this method in the laboratory is successful as a stand-alone solution.

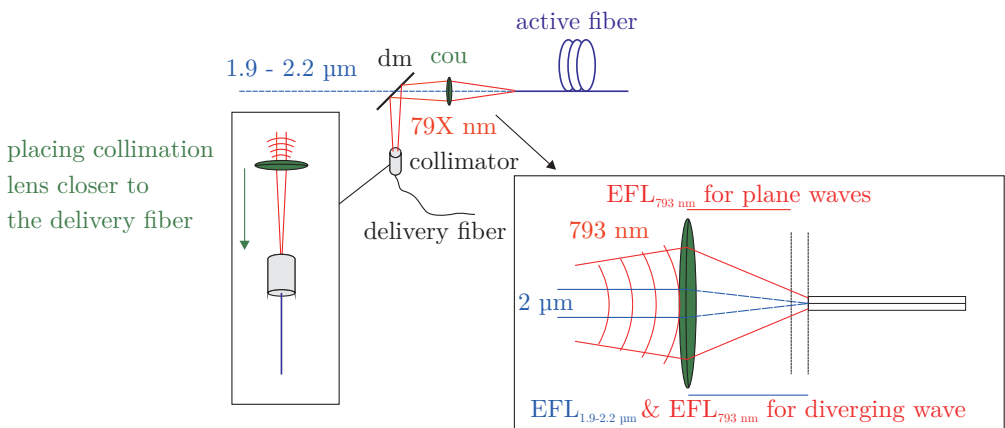


Figure 3.14: By placing the collimation lens of the pump radiation closer to the delivery fiber, a slightly divergent pump radiation is created. Due to this divergence, the focus of 79X nm radiation is shifted towards the focus of the signal. By this method, 100% of the pump radiation is coupled into the 1<sup>st</sup> cladding of the TCF.



## 4 Continuous-Wave Laser Operation

An essential part of this thesis is to establish a stable high-power laser in a CW operation mode using a THF laser. Besides various applications of CW laser radiation, realizing such a fiber laser also builds a fundamental basis for the upcoming pulse energy and average power scaling in pulsed laser operation. This chapter is mainly divided into two parts. First, a tunable laser source is developed as an essential tool to get insight into the gain distribution of the fiber for different setup configurations. The subsequent investigations are based on the information obtained from these tuning curves. The results are presented in Section 4.1. Afterward, the explicit power scaling of various fiber lasers at specific wavelengths is summarized in Section 4.2.

### 4.1 Broadly Tunable Laser Source

Realizing a tunable fiber laser in the 2  $\mu\text{m}$  region is an excellent start to locate possible operating wavelengths for further power scaling. Wavelengths above 2.09  $\mu\text{m}$  are typically not addressed by TDF lasers due to their low gain cross sections and, consequently, low emission. Tunable TDF lasers typically operate from 1900 to 2100 nm [108, 109], where systems with more than 100 W have been already demonstrated [110, 111]. Diffraction gratings (DGs) and volume Bragg gratings (VBGs) are mostly used as tuning elements. For the wavelengths above 2.1  $\mu\text{m}$ , typically HDF lasers are used. The measured tuning curves range from 2050 to 2170 nm [112, 113], exhibiting roughly a 50 to 70 nm shift compared to the TDF lasers.

Recently, Holmen et al. developed an in-band pumped HDF laser with a tuning range from 2025 to 2200 nm [106]. THFs are rarely investigated, even if their potential tuning range due to a combination of  $\text{Tm}^{3+}$  and  $\text{Ho}^{3+}$  emission cross sections could lead to a broad tunability.

Hemming et al. developed a 280 nm widely tunable codoped fiber laser with an emission up to 2150 nm [114]. A more recently developed tunable fiber laser based on a 5 m long THF, implemented in a similar setup to the one used within this chapter, was able to operate over a wavelength range of 2.05 to 2.15  $\mu\text{m}$  [115]. This confirms that the fiber type under investigation can work at holmium-dedicated wavelengths.

The intention is to expand these measurements further and identify the influence of different fiber lengths and OC reflectances. Therefore, in the beginning, multiple tunable laser setups are investigated to locate the gain distribution each setup realization can provide. Based on the outcome of these experiments, a particular setup can be chosen for specific power scaling. Parts of this section are published in [116–118].

### 4.1.1 Laser-Setup

The central part of the laser setup is already described in Section 3.1.2. Figure 4.1 displays an updated version of the completed setup with the additional components to realize a broadly tunable laser. A DG is used as a HR, providing continuously tunable wavelength-selective feedback.

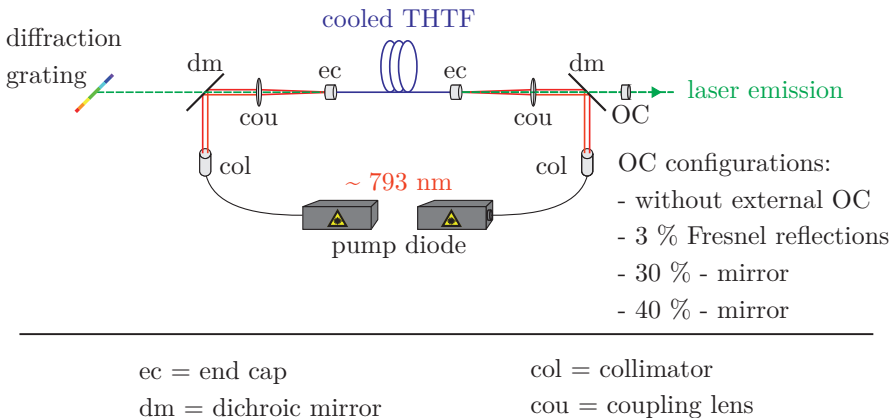


Figure 4.1: A DG is used to realize a tunable laser setup. By varying the fiber length and the reflectance of the OC, the best setup configuration of a high-power CW laser can be found.

The characteristics of the DG are described in Fig. 4.2. The left-hand side shows a schematic of a ruled diffraction grating. The grating equation [119] is also displayed as an inset for the special case in which the incident light and diffracted light are in-plane with the grating normal. The incident angle  $\alpha$  and diffraction angle  $\beta$  depend on the wavelength  $\lambda$ , the diffraction order  $m$ , and the groove density  $G$ , which is the inverse of the groove spacing. The incident and diffraction angles must be matched to use the DG as a retroreflecting mirror. This particular case is called Littrow configuration [119]. The right-hand side of Fig. 4.2 shows the reflected wavelength under the Littrow configuration in dependence on the Littrow angle. The groove density is 450 grooves/mm. By tuning the diffraction grating of about  $10^\circ$ , the wavelength region of interest around  $2\ \mu\text{m}$  can be swept over. The DG has a reflection efficiency of 90% compared to the reflectance of gold when used in the first diffraction order. The grating used is a copper substrate with an aluminum coating. These kinds of metallic components have a non-negligible amount of absorption even when used for reflection. Therefore, the DG is not meant for power or energy scaling. Without actively cooling, the grating suffers from significant heating and the potential risk of critical damage.

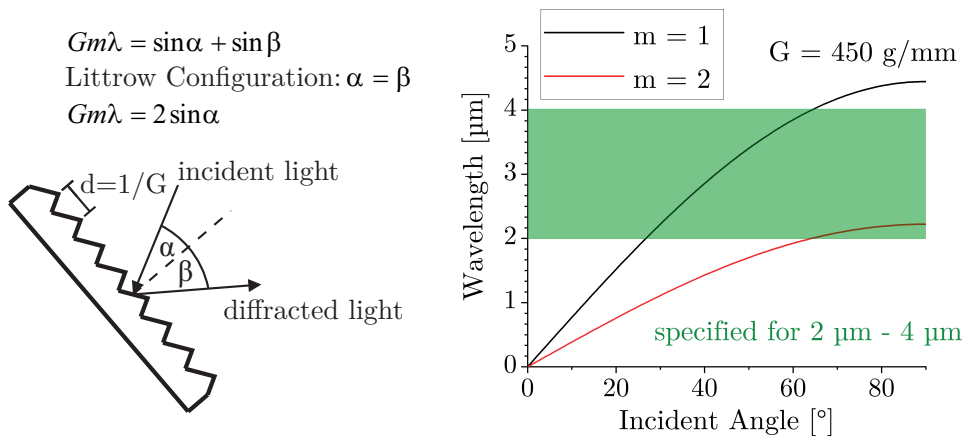


Figure 4.2: The left-hand side shows a schematic of a ruled diffraction grating together with the according grating equation. The right-hand side shows the operation wavelength of the grating in dependence on the operation angle when the grating is used in the Littrow configuration.

The tunability, gain distribution, and stable laser operating range are investigated for different OC reflectances. Two mirrors are used based on a dielectric coating. One mirror reflects 30% and the other one reflects 40%. The Fresnel reflections of an uncoated piece of glass are used to create an OC with a reflectance of 3%. In addition, the bare fiber to end cap splice (FTES) also provided sufficient feedback to use it as an OC. Therefore, this kind of laser configuration without external feedback is also investigated because this configuration can be responsible for parasitic laser operation when an external OC is used.

## 4.1.2 Experimental Results

### Initial results for an unoptimized laser setup:

In the first step, the initial laser results of different tuning curves are shown to visualize the progress achieved by optimizing the laser setup and to show the effects of poor signal and pump coupling as well as bad FTESs. In the hope of better beam quality, we have initially used the 18/270/297  $\mu\text{m}$  fiber. Due to its higher V-number, the 20/300/330  $\mu\text{m}$  fiber should have a stronger higher-order mode content. The initial tunable fiber laser is realized in a polarized state. Typically, generating a polarized laser source deteriorates the laser performance compared to a randomly polarized laser source and, therefore, could also limit the tuning curves. For measuring the initial tuning curves, a fiber length of 4.1 m and 7 m is used in combination with an OC reflectance of 3%.

Figure 4.3 shows the initial tuning experiments, where the laser output power is measured in dependence on the wavelength-selective feedback of the DG for a constant pump power. The fiber laser with an active fiber length of 4.1 m is tunable from 2007 to 2075 nm, having a maximum output power at 2030 nm. By increasing the fiber length to 7 m the tuning range of 68 nm is narrowed to 30 nm. The output power maximum is shifted towards 2070 nm. It is evident that the THF laser is not operating in the wavelength region where it is supposed to be since wavelengths above 2.1  $\mu\text{m}$  are not accessible at all.

Two main reasons could explain the short emission wavelength and the poor tunability. Non-optimized FTES can provide an increased reflectance. This lowers the threshold for parasitic lasing, cutting the edges of the tuning curves. In addition, the disturbed wavefront exiting the fiber and the signal radiation, which is poorly collimated and re-injected in the fiber due to the misplacement of the coupling lens, leads to a bad addressing of the cavity mirrors. Placing an external HR and OC should dramatically lower the required gain and population inversion for laser operation. This leads to a red-shift of the wavelength providing the maximum laser output.



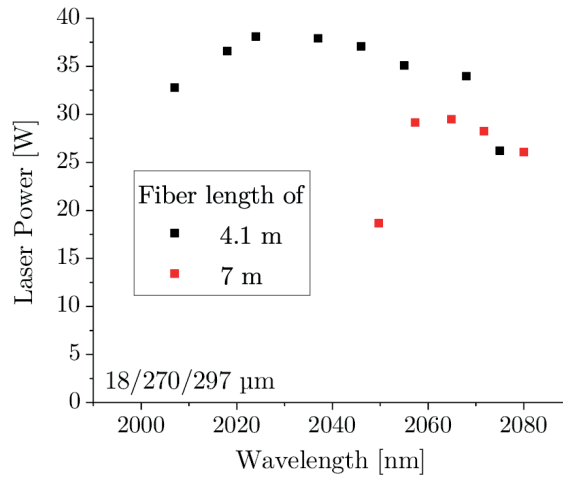


Figure 4.3: Initial tuning curves for an active fiber length of 4.1 m and 7 m.

In a free-running setup, where the fiber laser is built up between the two splices, the 4.1 m fiber and the 7 m fiber emit at a wavelength of 2020 nm and 2050 nm, respectively. The only slight red-shift of the wavelength in the tunable laser configuration with an external cavity compared to the free-running setup indicates that the cavity is not working correctly. Removing the OC does not affect the tuning curve. The connection between population inversion and the corresponding gain curve is discussed more deeply in the next paragraph.

### Tunable laser results for an optimized laser setup:

New tunable measurements are performed after the laser setup has been optimized regarding the critical points mentioned in Section 3.2 and Section 3.3. The 20/300/330  $\mu\text{m}$  fiber is used for these measurements. The determined output spectrum defines the valid laser operations, which are included in the tuning curves. A clean spectrum consists of no parasitic lasing and a negligible ASE content below 1%. Other values are excluded from the tuning curves.

A fiber length of 4.7 m is investigated for the first measurements. The output power of the tunable fiber laser is measured for different OC reflectances and a constant pump power of 100 W. These tuning curves are shown in Fig. 4.4. Without external OC, the laser is tunable from 2020 to 2110 nm with a maximum laser output power of  $\sim 22$  W at 2060 nm. Placing an OC with a reflectance of 3%, the maximum output power raises to 30 W and is located at an emission wavelength of 2080 nm, wavelengths from 1990 to 2160 nm are accessible. The output power decreases further by increasing the reflectance of the OC.

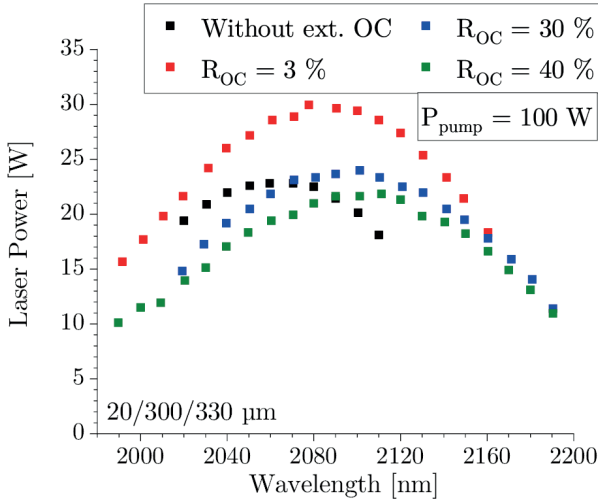


Figure 4.4: Tuning curves for a 4.7 m long active fiber with different OC reflectances. Wavelengths from 1.99  $\mu\text{m}$  up to 2.19  $\mu\text{m}$  are addressed. By increasing the reflectance of the OC, the tuning curve gets broader.

With an OC reflectance of 30 %, the tunable laser is able to operate from 2020 to 2190 nm with a power maximum of 24 W at 2.1  $\mu\text{m}$ . Figure 4.5 displays a set of normalized spectra for an OC reflectance of 30 %. The equidistant distances between the emission wavelengths are about 20 nm. No parasitic lasing or a significant amount of ASE is present. By using an OC with a reflectance of 40 %, the maximum laser output power shifts towards 2.11  $\mu\text{m}$ , exhibiting a tuning range from 1990 to 2190 nm. With this laser configuration, the laser is continuously tunable over 200 nm. A trend is visible that by increasing the reflectance of the OC, the tuning curves become flatter and shift towards longer wavelengths. To explain this behavior, the gain cross sections of  $\text{Ho}^{3+}$ -doped silica can be used. These gain cross sections in dependence of the inversion ratio  $\beta = N_2/N$  (from 0.05 to 0.25) are displayed in Fig. 4.6. The graph displays the wavelengths amplified by a certain amount of population inversion. Since an energy transfer efficiency from  $\text{Tm}^{3+}$  to  $\text{Ho}^{3+}$  of 80 % in state-of-the-art  $\text{Tm}^{3+}:\text{Ho}^{3+}$ -codoped silica fibers is reported [35], the gain cross sections of a pure HDF can be used in a first step even if the codoped fiber is much more complex. Also, in an accurate fiber laser, the inversion and gain cross section are a function of the position along the fiber and are not constant. By increasing the population inversion, the wavelength of maximum gain is blue-shifted and increases in amplitude. The long wavelength limit of the gain curve stays fixed, while the lower limit extends to shorter wavelengths. This is in good agreement with the measured tuning curves.

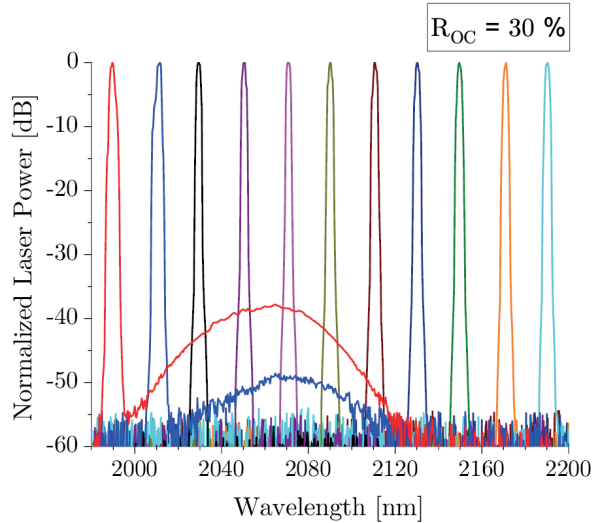


Figure 4.5: Selected emission spectra for the tuning curve with a fiber length of 4.7 m. The laser tuned to shorter emission wavelengths show a small amount of ASE compared to the longer wavelengths. However, all operating points do not show an ASE content > 1 % or any parasitic lasing.

Eq. (2.10) and (2.11) connect the reflectance of the OC to the inversion. The bare FTES has the lowest reflection ( $-45$  dB). Even this amount of feedback is large enough to act as an OC and start the laser oscillation in combination with the DG. This already shows that the reflection at the fiber to end cap interface is a potential risk for parasitic lasing when the laser is operated with an external OC and will limit the tuning range, the pulse energy scaling, and the stable power scaling at the edge of the emission cross sections.

A low OC reflectance needs a high single-pass gain to compensate for these losses and to establish laser operation. This leads to a high inversion inside the active fiber and a high lasing threshold. Due to the high inversion, the fiber laser has a broad and steep gain spectrum. With increasing OC reflectance, the necessary gain for laser operation is decreased together with the required inversion and the laser threshold.

The measured tuning curves do not extend over the whole wavelength range, which is predicted by the theoretical gain cross sections. The tunability is limited by parasitic lasing caused by other possible cavities inside the cavity. An additional cavity, which limits the tuning range, is the FTES from one side of the fiber and the FTES from the opposite fiber side. Other cavities which need to be considered are OC-FTES and FTES-DG. Parasitic lasing will likely rise when the laser is operated far away from the maximum gain.

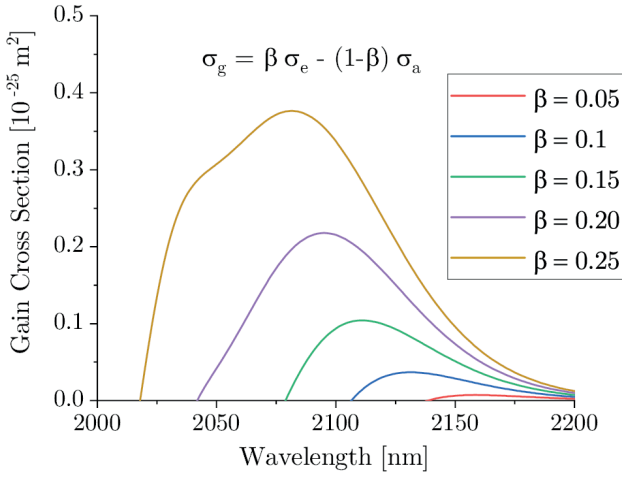


Figure 4.6: Gain cross sections of holmium for inversion ratios  $\beta = N_2/N$  from 0.05 to 0.25. By increasing the inversion, the gain curve gets broader.

For small OC reflectances and larger population inversions, the onsets of parasitic lasing are closer to the gain maximum compared to higher OC reflectances. This explains why the tuning curves become broader by increasing the OC even if the gain cross sections predict otherwise. With these considerations, the shape of the tuning curves can be explained.

The power levels measured in the tuning curves are a combination of the laser threshold and the slope efficiency, which are contrarily affected by the change of the OC reflectance. Operating far away from the lasing threshold, the power levels of the tuning curves are mainly determined by the slope efficiency and, therefore, will usually decrease by decreasing the amount of outcoupling. However, for the laser configuration, where the FTES is used as OC, the threshold is relatively high due to the minimal feedback, leading to a lower power level compared to the 3% OC.

A second experiment uses a fiber length of 6.5 m. Comparing these measurements with the measurements of the 4.7 m long fiber shows small changes. The measurements are depicted in Fig. 4.7. The output power levels of the tuning curves are slightly decreased but also red-shifted by 10 to 20 nm. This leads to higher output powers and a more stable laser operation for longer wavelengths. With an OC reflectance of 40%, the tunable laser is able to emit at 2200 nm. Figure 4.8 shows the spectral laser output for the tuning curve measured with an OC reflectance of 40%. The spectra are again clean in terms of negligible ASE and no parasitic lasing.

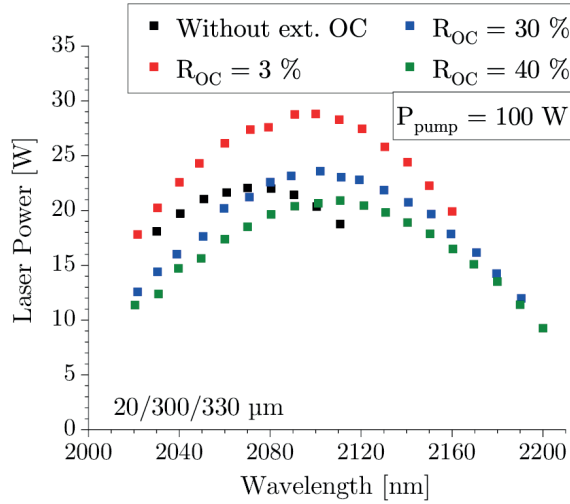


Figure 4.7: Tuning curves for a 6.5 m long active fiber with different OC reflectances. Wavelengths from 2.02  $\mu\text{m}$  up to 2.2  $\mu\text{m}$  are addressed.

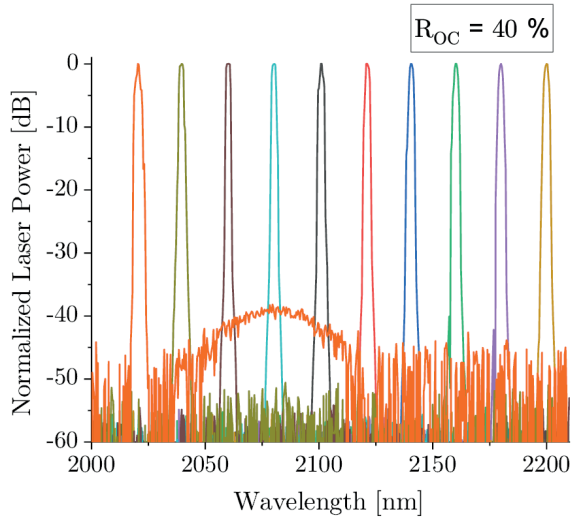


Figure 4.8: Selected emission spectra for the tuning curve with a fiber length of 6.5 m. The laser tuned to shorter emission wavelengths show a small amount of ASE compared to the longer wavelengths. However, all operating points do not show an ASE content > 1% or any parasitic lasing.

Two aspects are the leading cause of this red-shift. The fiber laser must provide the same overall single pass gain as the shorter fiber, leading to a lowered gain/inversion per length ratio and a red-shift according to the gain cross sections in Fig. 4.6. In addition, increasing the fiber length makes the generated signal more prone to be re-absorbed and re-emitted at longer wavelengths. An important parameter, which needs to be considered, is the background loss of a silica fiber. The background losses strongly increase from 2  $\mu\text{m}$  towards longer wavelengths and mainly affect lasing at 2.2  $\mu\text{m}$ . Therefore, increasing the fiber length does not automatically lead to increased laser output power for longer wavelengths. However, at some point, the losses dominate and prevent power scaling. The loss mechanism and their influence are further discussed for the continuous-wave power scaling at 2.2  $\mu\text{m}$  later.

Looking at the emission cross sections of thulium and holmium in Section 2.1.3, they are limited to 2.2  $\mu\text{m}$  like most of the values which can be found in the literature. In the next step, it is investigated if there is still gain for even longer wavelengths. Therefore, the tuning curves, shown in Fig. 4.7, are extended to values containing a larger amount of ASE or parasitic lasing. This will better indicate where a potential laser could operate in terms of longer wavelengths and what could be possible in a THF laser setup optimized for such a specific wavelength. Figure 4.9 shows the extended tuning curves and Fig. 4.10 displays the emission spectrum for a laser operation at an emission wavelength of 2.24  $\mu\text{m}$ .

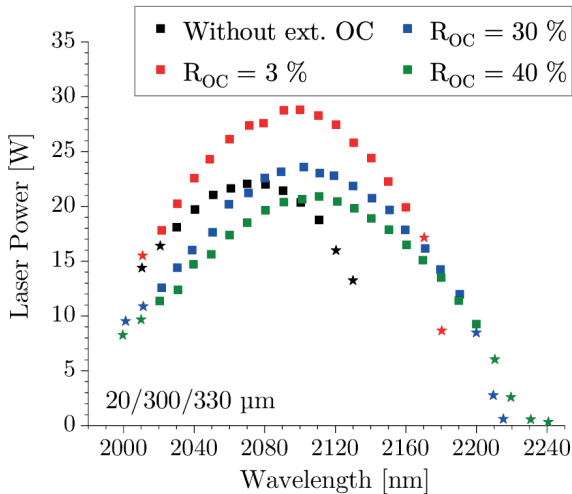


Figure 4.9: Tuning curves for a 6.5 m long active fiber with different OC reflectances. When including operating points showing parasitic lasing and an increased ASE content, wavelengths from 2.0  $\mu\text{m}$  up to 2.24  $\mu\text{m}$  are addressed.

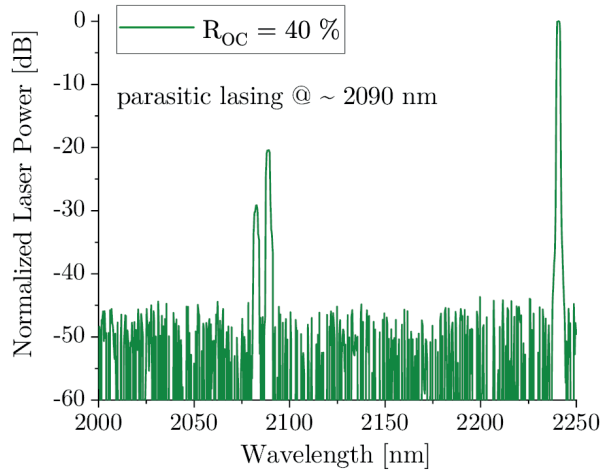


Figure 4.10: Laser emission spectrum for an operating point at 2240 nm. 2240 nm is the longest wavelength achieved by tuning the emission with a DG. The laser emission spectrum is no longer clean but shows parasitic lasing at 2090 nm.

Even if the laser power is below 1 W, it is possible to operate the laser up to 2240 nm. Parasitic lasing occurred at a wavelength of 2090 nm and is featured by the broadband OC with a reflectance of 40 %, which acts like the HR in this case and the FTES located on the DG side acts as the OC. The main output power of this oscillation is coupled out via the FTES and is then diffracted via the DG. This shows that an optimized fiber laser design can access potentially longer wavelengths than 2.2  $\mu\text{m}$ .

### 4.1.3 Discussion

The setup adjustments which have been done show a convincing effect when comparing Fig. 4.3 with Fig. 4.4 and Fig. 4.7. Broad tuning ranges of 200 nm are achieved up to a stable laser emission of 2200 nm. It is demonstrated that these long wavelengths are possible with careful population inversion management by increasing the OC reflectance. Comparing the measured tuning curves with a tunable HDF laser operated in a ring cavity shows similar results. The HDF laser shows a tuning range from 2025 to 2200 nm [106]. Other tunable HDF lasers based on a linear free-space cavity are tunable from 2.04 to 2.17  $\mu\text{m}$  [60, 112].

This indicates that the fiber composition is well optimized for  $\text{Tm}^{3+}$ - and  $\text{Ho}^{3+}$ -ion concentrations, and an efficient energy transfer occurs between the ions. Consequently, the THF laser can emit at wavelengths that are dedicated to HDF lasers.

Moreover, with an optimized setup, even longer wavelengths could be accessed than  $2.2\ \mu\text{m}$ . Three further steps can open up this wavelength region. First, the FTES can be adapted according to the example of Anderson et al. [15]. An angled splice would reduce the back-coupled radiation of the splice from roughly  $-45\ \text{dB}$  to  $-60\ \text{dB}$ . This leads to a strongly increased threshold for parasitic lasing. Second, replacing the DG ( $< 90\%$  reflection) with a VBG (close to  $100\%$  reflection) leads to a stable laser operation at longer wavelengths. In addition, the reflectance of the OCs is so far broadband, leading to high feedback for parasitic oscillation. As a third step, using wavelength selective feedback, like a special coating or a fiber Bragg grating (FBG), the OC can efficiently suppress parasitic lasing further. By these adjustments, an even wider tuning range and laser operation at longer wavelengths than  $2.2\ \mu\text{m}$  would be possible.

A strong, stable laser gain is established above emission wavelengths of  $2.1\ \mu\text{m}$ , which shows good potential for scaling the laser output power. The next step is to realize high-power laser operation from  $2.1$  to  $2.2\ \mu\text{m}$  and show that THF lasers can operate stably and efficiently at wavelengths which are dedicated to HDF lasers.

## 4.2 Stable Power Scaling for Fixed Wavelengths

### 4.2.1 Review of Relevant State-of-the-Art Lasers

High-power laser radiation in the  $2\ \mu\text{m}$  regime opens the field for different applications. A theoretically increased threshold for limiting nonlinear processes, which scales by  $\lambda^2$ , promises an advantageous power scaling. The highest output powers so far are generated in TDF lasers, where  $1\ \text{kW}$  of laser output power is reached [14, 15]. The first  $1\ \text{kW}$  laser was developed in 2010, but no significant improvement in output power has been achieved since then. A few laser systems delivering similar output powers have been developed so far. However, around  $1\ \text{kW}$ , there seems to be a harsh limit due to the onset of mode instabilities [120, 121]. Investigating this phenomenon and its mitigation is an ongoing part of the research. Another topic is shifting the emission wavelength of these high-power CW lasers towards longer wavelengths since the  $1\ \text{kW}$ -level systems are mainly emitting between  $1950$  to  $2050\ \text{nm}$ . Table 4.1 shows an overview of state-of-the-art laser systems for power scaling laser emission at and beyond  $2090\ \text{nm}$ .



Table 4.1: State-of-the-art high-power continuous-wave lasers for an emission in the long-wavelength 2  $\mu\text{m}$  region.

Active Fiber	Wavelength [nm]	Power [W]	Slope Efficiency [%]	Laser Details	Author
$\text{Tm}^{3+}$	2110/2130	450/80	51/50	<ul style="list-style-type: none"> <li>• Two-tone technique</li> <li>• All-fiber</li> <li>• more complex MOPA setup</li> </ul>	Anderson et al.[120, 122]
$\text{Tm}^{3+}:\text{Ho}^{3+}$	2090	195	44.8	<ul style="list-style-type: none"> <li>• all-fiber laser</li> <li>• single-oscillator</li> <li>• <math>M^2 = 1.08</math></li> </ul>	Motard et al.[123]
$\text{Tm}^{3+}:\text{Ho}^{3+}$	2105	83	42	<ul style="list-style-type: none"> <li>• free-space single-oscillator</li> <li>• <math>M^2 = 1.5</math></li> <li>• melting of the fiber ends</li> </ul>	Jackson et al.[124]
$\text{Tm}^{3+}:\text{Ho}^{3+}$	2120	155	35	<ul style="list-style-type: none"> <li>• all-fiber laser</li> <li>• single-oscillator</li> </ul>	Motard et al.[125]
$\text{Ho}^{3+}$	2120	62	60	<ul style="list-style-type: none"> <li>• single-oscillator</li> <li>• <math>M^2 = 1.2</math></li> <li>• pump: 1.958 <math>\mu\text{m}</math> <math>\text{Tm}^{3+}</math></li> </ul>	Beaumont et al.[29]
$\text{Ho}^{3+}$	2120	407	40	<ul style="list-style-type: none"> <li>• monolithic single-oscillator</li> <li>• diffraction-limited beam</li> <li>• pump: 1.95 <math>\mu\text{m}</math> <math>\text{Tm}^{3+}</math></li> </ul>	Hemming et al.[60]
$\text{Ho}^{3+}$	2120-2150	140	59	<ul style="list-style-type: none"> <li>• free-space single-oscillator</li> <li>• pump: 1.95 <math>\mu\text{m}</math> <math>\text{Tm}^{3+}</math></li> </ul>	Hemming et al.[126]
$\text{Ho}^{3+}$	2200	8.9	27	<ul style="list-style-type: none"> <li>• ring cavity, free-space</li> <li>• <math>M^2 = 1.2-1.4</math></li> <li>• pump: 1.958 <math>\mu\text{m}</math> <math>\text{Tm}^{3+}</math></li> </ul>	Holmen et al.[106]

As already explained, power scaling of TDFs is quite challenging for emission wavelengths exceeding 2090 nm. Nevertheless, Anderson et al. were able to scale the laser output within a TDF at an emission wavelength of 2110 nm up to 450 W [15]. This was achieved thanks to laser gain competition inside the active fiber. With the identical approach even 80 W of output power at an emission wavelength of 2130 nm were successfully generated [122]. Both power scaling measurements show a slope efficiency of 50 %.

Besides this exception, typically THF or purely HDF lasers are used. The attempts to establish high-power laser operation with THF lasers are pretty rare and focus on emission wavelengths from 2090 to 2105 nm. Jackson et al. demonstrated a  $\text{Tm}^{3+}:\text{Ho}^{3+}$ -codoped fiber laser at 2105 nm with an output power of 83 W in a free-space laser setup [124]. Further power scaling was limited by melting the fiber ends, highlighting the investigation and utilization of fiber end caps. Motard et al. realized an all-fiber laser at an emission wavelength of 2090 nm and 2120 nm up to 195 W and 155 W, respectively [123, 125].

For HDF lasers 2120 nm is the most investigated emission wavelength since the wavelength matches an atmospheric transmission window with a simultaneous high gain operation. Gouet et al. developed a 90 W laser system with a slope efficiency of 50 % [28] and improved their system later towards a higher slope efficiency of 60 % with an output power of 50 W [29]. Hemming et al. developed a MOPA laser system delivering 265 W and an oscillator with a record output power of 407 W [60]. The slope efficiency w.r.t. absorbed pump power was 45 % and 40 %, respectively. It appears that HDF lasers, which exhibit a theoretically low quantum defect, are not performing as expected. This is a chance for the THF version to compete with similar performance and the advantage of a much simpler setup. Parts of this section are published in [116–118, 127].

## 4.2.2 Laser-Setup

Compared to the tunable laser setup, only small adjustments are necessary to realize a setup capable of scaling the laser output power. Figure 4.11 displays an adapted setup for high-power CW operation. A critical component here is the HR. Initial power scaling measurements are done with a DG. However, due to bad thermal properties, alignment issues, and a low reflectance < 90 %, the DG is replaced. The requirements for a HR in a high-power fiber laser configuration are a high reflectivity for realizing a uni-directional laser, a high damage threshold for withstanding intense laser radiation, and a low absorption to avoid thermal effects.

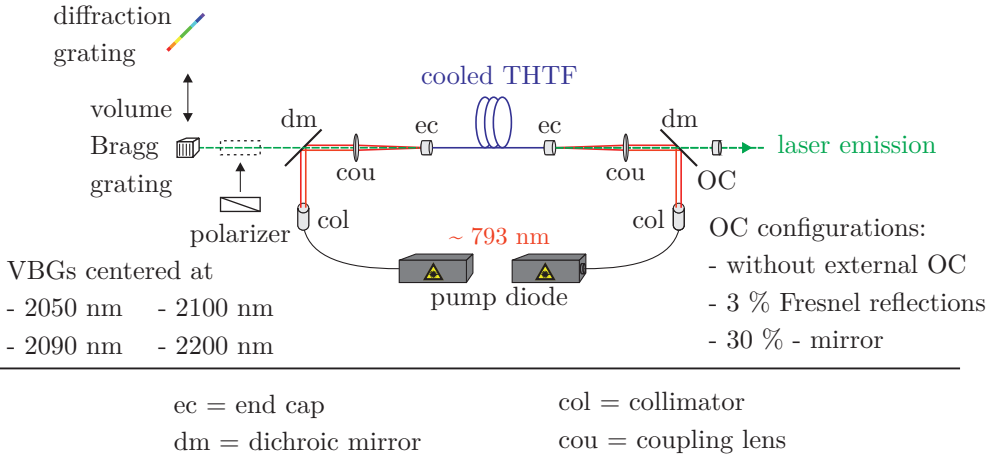


Figure 4.11: Setup scheme for CW laser configuration. Critical components are a narrowband and highly reflecting VBG as HR and various OCs (without external OC, 3%, and 30%).

In addition, the HR needs to provide narrowband feedback for a well-defined laser emission wavelength. Therefore, a VBG, a UV-written grating inside a photosensitive glass cube, is a perfect choice [128]. VBGs, which are reflecting at a wavelength of 2050 nm, 2090 nm, 2100 nm, and 2200 nm, are used to build a fiber laser. The fiber length and OC are chosen according to the information gained by the tuning measurements in Section 4.1.

The laser output spectrum is one of the most important optical characteristics for applications like nonlinear frequency conversion. Since the VBG significantly influences the output spectrum, it is essential to know the exact reflectance of this optical component. A small device has been built to measure the VBG reflectance, which is depicted in Fig. 4.12. The output of a HDF-based ASE source is entering port 1 of a fiber circulator. The signal exits port 2 and then launches into free space. The ASE signal is collimated by a lens and then directed on the VBG under investigation. The reflected ASE signal is back-coupled into the fiber and re-entering port 2 of the fiber circulator. After leaving port 3 of the circulator, an optical spectrum analyzer measures and displays the reflected ASE signal. The spectral reflectances of the VBGs are also shown in Fig. 4.12.

Every VBG has the same specification with a FWHM smaller than 1 nm. The measurement shows that the actual values differ by more than a factor of two. The 2050 nm VBG has a FWHM of 370 pm, whereas the 2090 nm VBG has a FWHM of 890 pm. The 2100 nm VBG is in-between with a FWHM of 430 pm.

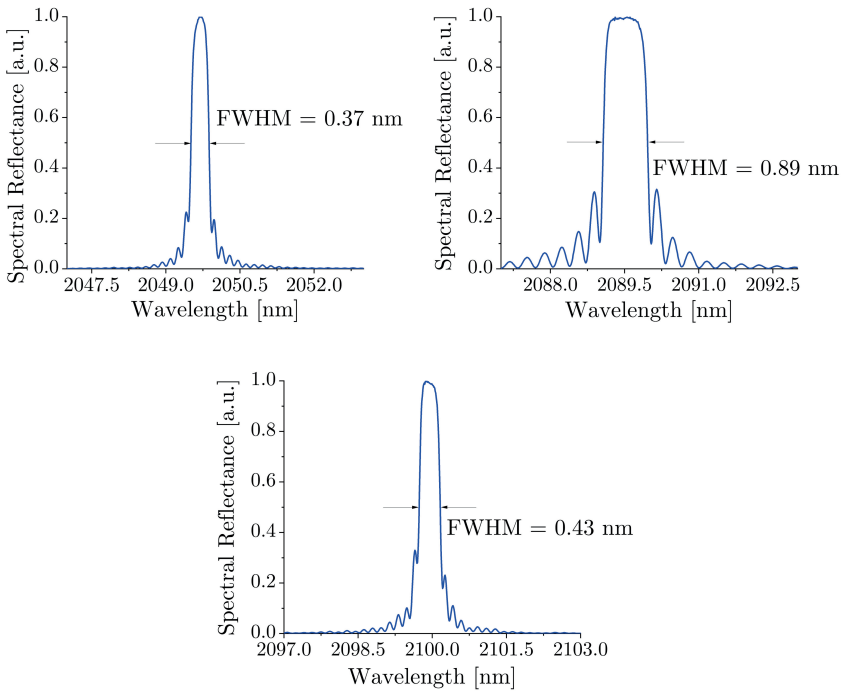
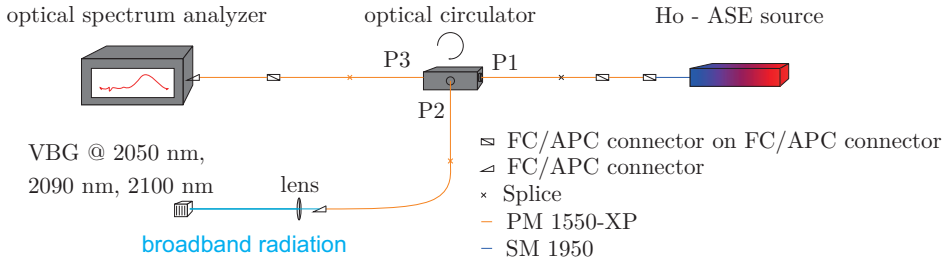


Figure 4.12: The upper half of the image shows a setup for measuring the reflection characteristics of VBGs. The signal of a holmium ASE source is reflected by the VBG and afterward measured using a spectrum analyzer. The lower half of the image shows the measured characteristics for three different VBGs centered at 2050 nm, 2090 nm, and 2100 nm.

This difference in FWHM will also be visible in the spectral width of the different laser sources later. Since the ASE source is not able to cover the wavelengths up to 2.2  $\mu\text{m}$ , it is not possible to measure the reflectance of this VBG.

The temperature dependence of the reflectance is also measured to explain possible spectral shifts. The temperature of the VBG holder is tuned from 10 °C to 40 °C. The shape of the reflectance is maintained, but the center wavelength shifts with  $1.83 \text{ pm K}^{-1}$ .

### 4.2.3 First experimental results below 2090 nm

Initial power scaling attempts are made after the first tuning curves (see Fig. 4.3) have been measured, showing limited wavelength accessibility. In a first measurement, the gain maximum at  $\sim 2030 \text{ nm}$  for a 4.1 nm long THF fiber is addressed. Since there was no VBG for this wavelength, the measurement is done with the DG as HR. Even though it is not advisable to perform power scaling with the DG as described earlier, the measurement is surprisingly stable. Figure 4.13 shows the laser output power versus the incident pump power. The maximum laser output power is 139 W for an incident pump power of 434 W. The threshold is 31 W with a slope efficiency of 36.2%. The power scaling attempt is pump power limited. It is obvious that the setup is not fully functional since the slope efficiency and the emission wavelength are relatively low.

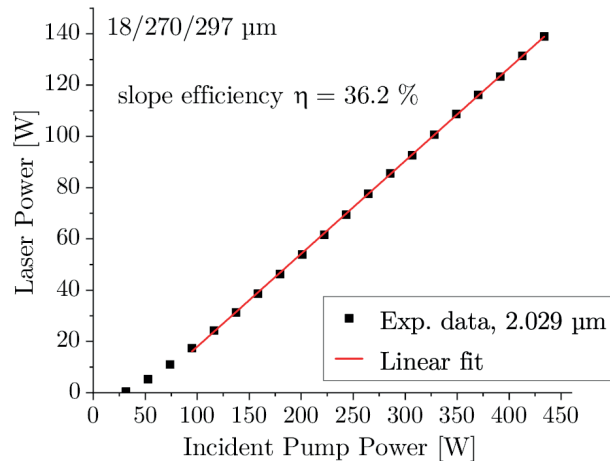


Figure 4.13: Laser output power versus pump power for an emission wavelength of 2020 nm. First power scaling attempts show relatively low slope efficiencies and laser operation is restricted to wavelengths far below 2090 nm.

A beam quality measurement shows another problem already described in Section 3. Bad splicing conditions and destructive signal coupling lead to a non-diffraction limited output beam despite a V-number close to a proper single-mode operation. The beam propagation factor  $M^2$  compares the beam propagation of the beam under investigation to that of a Gaussian beam, which has an  $M^2$  factor of 1 [129]. The beam propagation factor  $M^2$  is defined as the beam parameter product divided by  $\lambda/\pi$  [129]:

$$M^2 = \theta \omega_o \frac{\pi}{\lambda} \quad (4.1)$$

Therefore, the  $M^2$  factor indicates how well a laser beam can be focused or collimated. The laser beam quality can be measured by different methods, e.g., by using special wavefront sensors [130]. In our case, the  $M^2$  factor is measured as close as possible according to the ISO Standard 11146 [131] to reach a certain comparability within the community. The measurement itself is anything else than trivial [132]. To determine the beam quality, the caustic of the laser beam has to be measured and fitted to the Eq. (3.2) for Gaussian beam propagation. Out of this fit, the beam propagation factor can be calculated.

The procedure, according to the ISO standard, is as follows: The initial situation is a collimated laser beam, which is focused by an aberration-free lens. Using a suitable camera, the transverse beam profile must be measured at least five times within the Rayleigh range and five times outside of two Rayleigh lengths. The beam diameter must be determined according to the  $D4\sigma$ -width. The measurement of the beam propagation factor  $M^2$  at an output power of 119 W is displayed in Fig. 4.14. The bullets and triangles are the measured radii for certain relative propagation distances in the x- and y-direction, respectively. The two lines are the corresponding fits to Eq. (3.2). A beam propagation factor  $M^2_x$  of 1.87 and a beam propagation factor  $M^2_y$  of 1.78 is determined. The beam quality is not close to diffraction-limited, and according to the insets, non-negligible power is located around the Gaussian beam. This is another hint that the non-optimized laser setup is not working properly.

In the next step, the DG is replaced by a VBG centered at 2050 nm. The same power scaling is performed for the DG but with a longer emission wavelength. Figure 4.15 shows the output power versus the incident pump power. The laser threshold is reduced to 25 W, and the slope efficiency stays roughly unchanged. An output power of 140 W is reached with an incident pump power of 434 W.

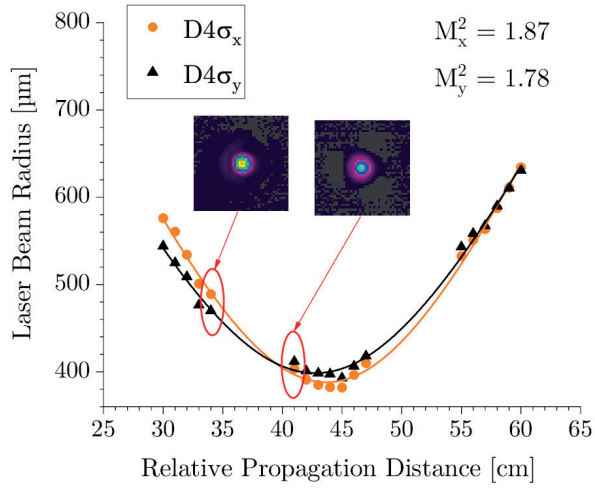


Figure 4.14: Beam quality measurement for an emission wavelength of 2029 nm and an output power of  $\sim 119$  W. The laser could not deliver a diffraction-limited beam quality without optimizing the setup.

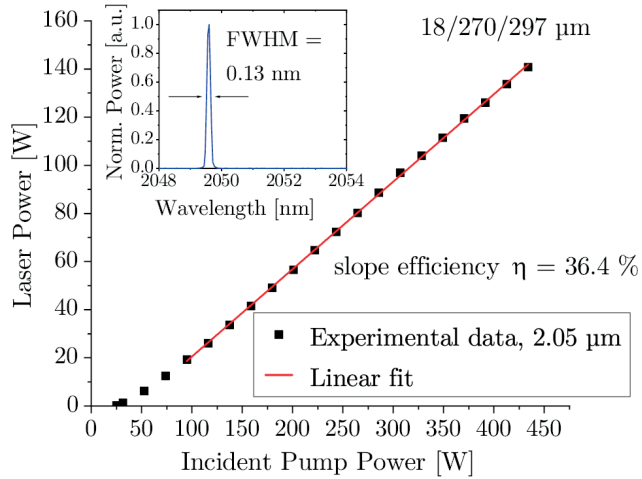


Figure 4.15: Laser output power versus pump power for an emission wavelength of 2050 nm. The inset shows the output spectrum for maximum output power.

The fiber laser performs similarly despite red-shifting the wavelength by 20 nm. This is due to the VBG, which provides higher and more stable feedback than the DG. Therefore, potentially longer wavelengths can be addressed as indicated by the tuning curves. The inset of Fig. 4.15 shows the laser output spectrum at 117 W of output power. A single peak is visible with a FWHM of 130 pm. The peak perfectly overlaps with the measured reflectivity curve of the VBG (compare to Fig. 4.12).

Looking at the first power scaling attempts in CW operation shows that the fiber integrated into the free-space setup can operate up to 140 W of output power without problems. However, the accessible wavelength region, slope efficiency, and beam quality fall short of expectations. This means simply exchanging the low-power pump diodes with higher-power versions will not lead to a successful high-power operation. Compared to a low-power setup, splicing, signal and pump coupling, and thermal issues must be addressed as explained in Chapter 3.

#### 4.2.4 Experimental Results at 2100 nm

The following measurements are done in an optimized laser setup. The tuning curves in Fig. 4.4 and 4.7 show that there is a gain maximum from 2080 to 2100 nm when the laser is operated with an OC reflectance of 3 %. Here, the laser should exhibit the highest slope efficiencies. VBGs centered at 2090 nm and 2100 nm are available. Since the 2100 nm VBG shows a narrower reflectance (Fig. 4.12), it is chosen for explicit power scaling. Also, the emission at a longer wavelength justifies using a THF compared to a TDF.

High output powers are targeted; in the best case, the laser will be pump power limited. In a symmetrically pumped laser setup, all non-absorbed pump power from the first diode laser will be directly sent back into the second diode laser and vice versa. The fiber length is changed from 4.7 m to 6.5 m to prevent damage to the diode lasers during high-power operation caused by non-absorbed pump radiation.

Figure 4.16 shows the laser output power in dependence on the incident pump power. The laser delivers 262 W of output power for a pump power of 574 W and a slope efficiency of 49.3 %. The laser power threshold is at 16 W.

The beam quality is measured for an output power of  $\sim 200$  W and is depicted in Fig. 4.17. A beam propagation factor  $M^2$  of 1.2 is determined on the x- and y-axis. This indicates an almost diffraction-limited beam propagation. The inset shows a picture of the laser beam.



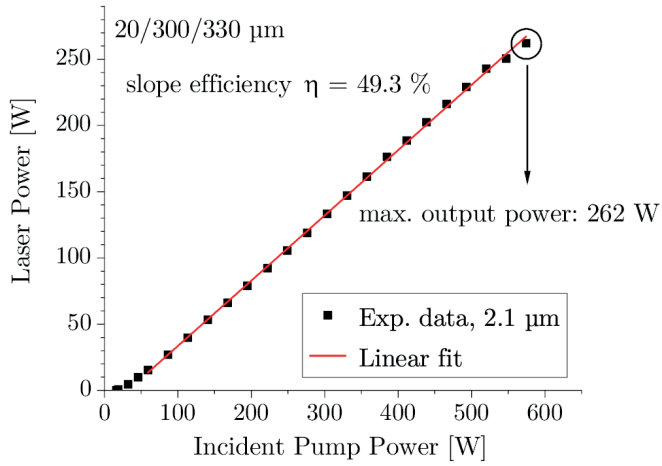


Figure 4.16: Laser output power versus pump power for an emission wavelength of 2100 nm. The laser shows a slope efficiency of 49.3% with a maximum output power of 262 W for an incident pump power of 574 W.

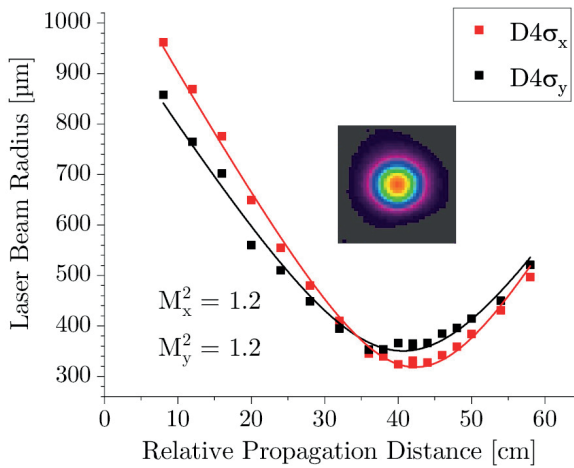


Figure 4.17: Beam quality measurement for an emission wavelength of 2100 nm and an output power of  $\sim 200$  W. A beam propagation factor  $M^2$  of 1.2 is measured.

Figure 4.18 shows the laser emission spectrum and a stability measurement, also measured for an output power of  $\sim 200$  W. Compared to the laser realized at 2050 nm, the emission spectrum shows 3 defined peaks with a FWHM of 89 pm and a 20 dB width of 600 pm. The origin of these equidistant peaks has yet to be explained. The peaks could result from an etalon effect within the cavity, but the responsible cavity could not be identified. The measured peaks are not the different longitudinal modes. One peak contains many longitudinal modes, which the optical spectrum analyzer can not resolve. As an example, for a 4.1 m fiber, the free spectral range in silica is determined by  $\Delta\nu = c/(2n_G l) = 24.9$  kHz [133], where  $l$  is the fiber length and  $n_G$  the group index of 1.469 [134]. Transferring this into a wavelength spacing at 2050 nm leads to a mode spacing of 366 fm, which differs by several orders of magnitude compared to the measured peak distance of 0.2 nm.

The reflectance bandwidth of the VBG determines how many peaks are supported and visible in the output spectrum. The VBG centered at 2050 nm shows the most narrow reflectance bandwidth and, therefore, only supports 1 or 2 emission peaks. Whereas for the 2100 nm VBG, 2 or 3 peaks are typically visible in the output spectrum, the emission spectrum of a laser built with the 2090 nm VBG shows 3 to 4 peaks and, therefore, also a much broader output spectrum. Besides the output power, the beam quality, and the output spectrum, the long-term performance of the laser is measured. For this purpose, the laser output power is measured over a time of 1 h. A standard deviation of 0.6 W is determined, showing a good power stability. The inset of Fig. 4.18 displays a closeup of the stability measurement.

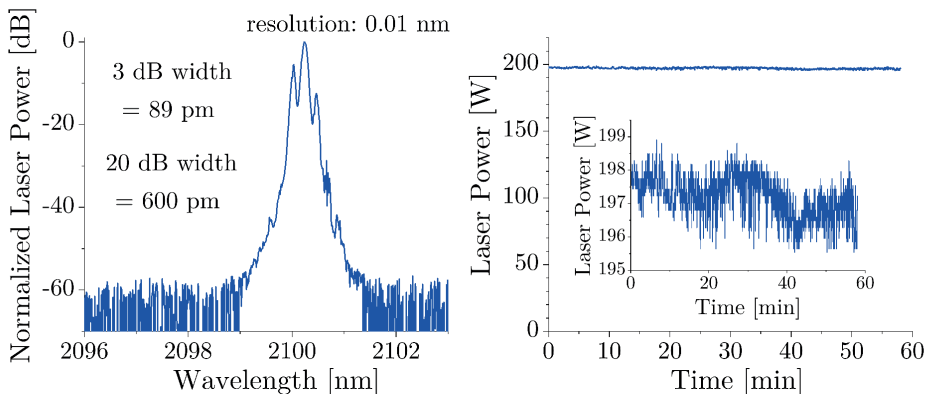


Figure 4.18: Left: Laser spectrum for an emission wavelength of 2100 nm. The FWHM is 89 pm. Right: Stability measurement for a laser output power of 200 W. The inset shows a closeup.

## 4.2.5 Experimental Results at 2200 nm

According to the tuning curves in Fig. 4.4 and Fig. 4.7, the tunable fiber laser can operate over a broad wavelength range and even wavelengths up to  $2.2\ \mu\text{m}$  can be achieved. An emission wavelength of  $2.2\ \mu\text{m}$  can be seen as the wavelength operation edge of silica fiber lasers. The longest wavelength emitted from silica-based fibers relying on stimulated emission is currently at  $2210\ \text{nm}$  [135]. At that wavelength, a HDF laser delivered  $120\ \text{mW}$  in 1996. The highest output power in this wavelength region is also achieved by a HDF laser with a maximum output power of  $8.9\ \text{W}$  [106].

In general, power scaling is quite challenging within this wavelength region, and this is based on two reasons. Firstly, the emission cross sections of  $\text{Tm}^{3+}:\text{silica}$  and  $\text{Ho}^{3+}:\text{silica}$  are becoming vanishingly small around  $2.2\ \mu\text{m}$  as can be seen in Fig. 2.8 and Fig. 2.10. Secondly, the signal absorption in silica fibers strongly increases towards  $2.2\ \mu\text{m}$ . The absorption consists of one part which is intrinsic to silica and one part which is related to impurities. During the manufacturing process, it is unavoidable to have a small hydroxyl ( $\text{OH}^-$ ) contamination inside the fiber leading to serious absorption due to the first overtone of the fundamental antisymmetric stretching vibration of OH [136]. In addition, the silica network absorbs the signal due to the uprising edge of multiphonon absorption [137, 138]. This means that increasing the fiber length can have a detrimental effect on the laser performance for fiber lasers emitting at  $2.2\ \mu\text{m}$ .

For power scaling at  $2.2\ \mu\text{m}$ , a  $4.7\ \text{m}$  and a  $6.5\ \text{m}$  long fiber are investigated. An OC reflectance of  $30\%$  is used. Despite the tuning curves do not show a clean laser operation at  $2.2\ \mu\text{m}$  using an OC reflectance of  $30\%$ , changing to an almost  $100\%$  reflecting VBG ensures a stable laser operation. Figure 4.19 shows the laser output power in dependence on the incident pump power for both fibers. First, the power scaling is performed with the  $4.7\ \text{m}$  long fiber. The threshold is  $21\ \text{W}$  with a slope efficiency of  $28.8\%$ . The adjustment of the free-space laser cavity is highly critical. Every small misadjustment leads to parasitic lasing. To avoid damaging any component when the fiber laser switches from a clean laser operation to a parasitic one, the power scaling is stopped at  $77\ \text{W}$ . The power scaling is performed with the  $6.5\ \text{m}$  long fiber active fiber in the next step. A  $23\ \text{W}$  power threshold is measured with a slope efficiency of  $25.3\%$ . The power scaling is much more stable regarding small misadjustments, and a pump-power-limited output power of  $145\ \text{W}$  is achieved. The slope is lower and the threshold higher compared to the shorter fiber.

Comparing both fiber lasers up to 77 W of output power, the longer fiber has a slope efficiency of 27.7% and is quite close to the 4.7 m fiber laser version. The slight decrease after 77 W is attributed to the increased thermal load in fiber and optical components due to the relatively large absorption at 2.2  $\mu\text{m}$ . Increasing the fiber length enables a more stable laser operation at the cost of a slightly lower slope and a higher threshold.

The following optical characteristics of the laser are measured for the 4.7 m fiber. Figure 4.20 shows the laser beam quality measured for an output power of  $\sim 70$  W of the 4.7 m fiber laser. The beam profile is depicted as an inset. The beam propagation factor is 1.1 and 1.2 in the x- and y-direction, respectively. This indicates an almost diffraction-limited beam quality. The V-number decreases compared to the emission of 2.1  $\mu\text{m}$ , closer to a strictly single-mode operation. The left-hand side of Fig. 4.21 displays the laser output spectrum measured for a laser output power of 77 W with a closeup as inset. No ASE or parasitic lasing is observed down to  $-50$  dB from the peak of the laser signal. The FWHM is 410 pm. The right-hand side of Fig. 4.21 shows a power stability measurement for an output power of 69 W. The laser output power is measured over 1 h, showing a standard deviation of 0.16 W. The inset shows a closeup of the measurement.

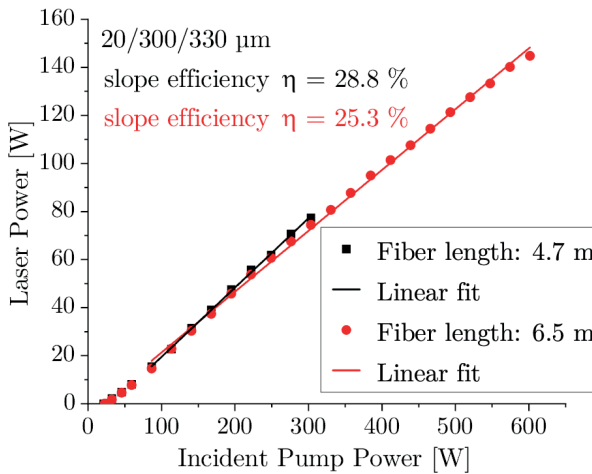


Figure 4.19: Laser output power versus pump power for an emission wavelength of 2200 nm and fiber lengths of 4.7 m and 6.5 m.

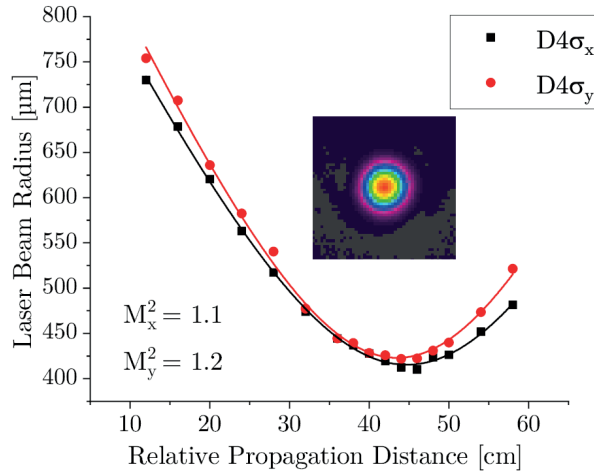


Figure 4.20: Beam quality measurement for an emission wavelength of 2200 nm and an output power of 69 W. The beam propagation factor  $M^2$  is 1.1 and 1.2 in the x- and y-direction, respectively. The inset shows a beam profile.

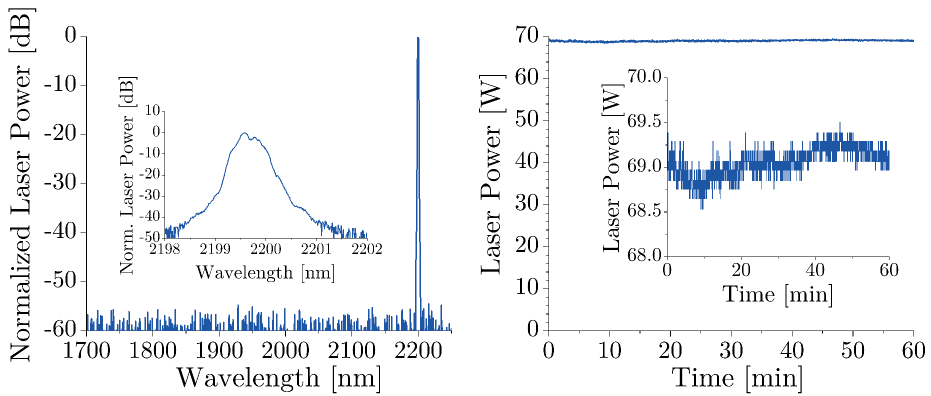


Figure 4.21: Left: Laser spectrum for an emission wavelength of 2200 nm. No ASE or parasitic lasing is visible. The inset shows a closeup. Right: Stability measurement for a laser output power of 69 W.

## 4.2.6 All-fiber Laser Realization at 2120 nm

So far, all setups are based on a free-space laser arrangement. Within this chapter, it is shown that the THF laser is capable of operating efficiently at long wavelengths ( $> 2.1 \mu\text{m}$ ). Based on this finding, realizing an integrated, more rugged, and compact THF laser setup is a reasonable next step. In a CW regime, building an all-fiber configuration is possible where no alignment is needed. However, this brings new challenges regarding adequate splicing [98–100]. Within this subsection a first all-fiber THF laser is described, emitting at 2120 nm. The results have been presented at [139].

Fig. 4.22 shows the relatively simple fiber laser schematic. The active fiber under investigation is the 20/300/330  $\mu\text{m}$  THF. A 275 W diode laser, emitting at 79X nm, is used as a pump source. The delivery fiber (200/240  $\mu\text{m}$ ) is directly spliced on a passive fiber that matches the active fiber. This fiber contains an FBG written into it. The FWHM reflection bandwidth is 2 nm centered at 2121 nm with a peak reflectivity of 99.8%. This first FBG will be used as an HR. The pump transmission of the FBG is 96.7%. The pump power is then defined as the power of the diode laser minus the losses of the HR-FBG. The corresponding low reflector (LR)-FBG has a reflection bandwidth of 0.43 nm and a peak reflectivity of 9.4%. A 7.5 m long active THF (20/300/330  $\mu\text{m}$ ) is sandwiched between the HR and the LR. A water basin actively cools the active fiber and the splices of both sides of the active fiber. A cladding light stripper is placed after the LR to remove the residual pump light. An end cap is spliced to the passive fiber to extract the signal from the fiber safely.

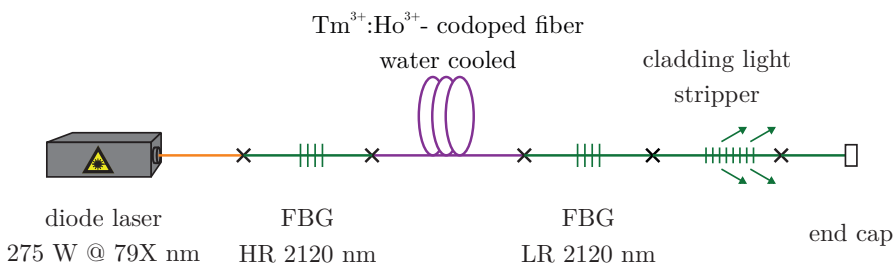


Figure 4.22: Schematic setup for an all-fiber THF laser. The setup consists of a 275 W diode laser, a FBG high and low reflector as the cavity, a 7.5 m THF (violet), a cladding light stripper, and an end cap. The fiber marked in green is a passive-matched fiber to the active fiber. The fiber displayed in orange is a 200/240  $\mu\text{m}$  MMF of the diode laser.

Figure 4.23 shows the measured laser output power in dependence on the pump power. The fiber laser has a threshold below 21 W and shows a slope efficiency of 47.2%. A maximum output power of 115 W is achieved. Despite using a cladding light stripper, 3.2 W of pump power still exits from the fiber end, which has to be removed.

The measurement of the beam propagation factor  $M^2$  for a laser output power of 50 W is shown in Fig. 4.24. An  $M^2$  factor of 1.32 and 1.38 is determined in x- and y-direction, respectively. The beam shape looks not entirely circular but has an oval shape. In addition, there is a background light in the shape of a sickle, which could be higher-order mode content.

Figure 4.25 displays the measured spectra. The left-hand side shows the spectra for an output power of 115 W from 1900 to 2200 nm. No ASE or parasitic lasing is observed down to  $-70$  dB. The right-hand side shows the spectra closer to the signal from 2110 to 2125 nm for different laser output powers. With increasing laser output power from 14 to 115 W, the spectra shift slightly to longer wavelengths and the FWHM spectral width increases from 142 to 198 pm. The all-fiber laser realization shows a stable power scaling without a thermal roll-off or damage, good slope efficiency, and a clean output spectrum. The setup is designed in a simple way, and further power scaling will be easily achieved by changing to a more powerful diode laser of 500 W. However, further power scaling will need a more careful optimization of the splices. This will increase the stability of the splices and most likely improve the beam quality.

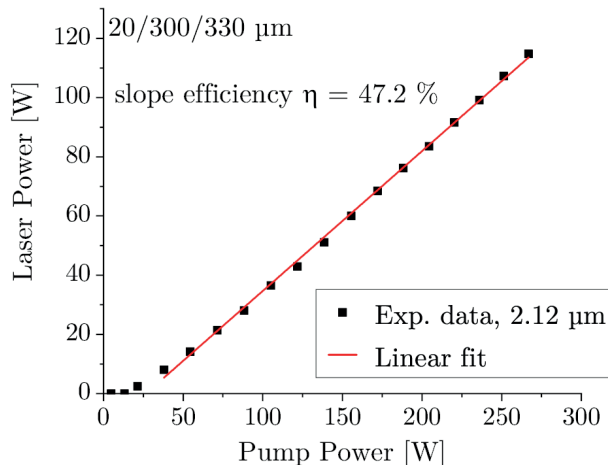


Figure 4.23: 2120 nm laser output power versus pump power of an all-fiber laser setup. A slope of 47.2% with a pump-power-limited maximum output power of 115 W is measured.

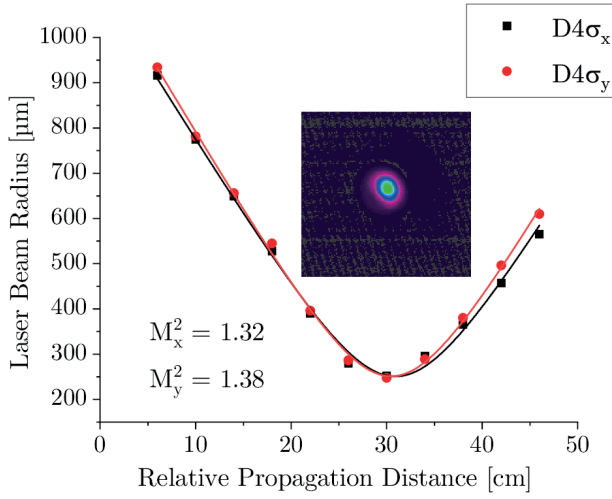


Figure 4.24: Beam quality measurement of the all-fiber laser setup for an emission wavelength of 2120 nm. The beam quality factor  $M^2$  is 1.32 and 1.38 in x- and y-direction, respectively.

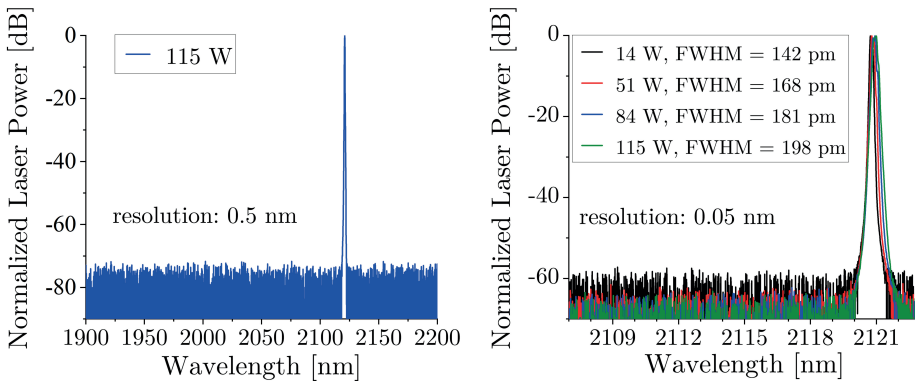


Figure 4.25: Spectral Power of the all-fiber laser setup at an emission wavelength of 2120 nm. Left: No ASE or parasitic lasing is visible on a wide wavelength range of 1900 to 2200 nm. Left: A closeup of the emission spectrum shows a small red-shift of the center wavelength and the FWHM for increasing laser output power.



## 4.2.7 Discussion

As a first conclusion, a successful pump-power-limited power scaling of several THF laser free-space single-oscillators with reasonable output power, efficiency, beam quality factor  $M^2$ , and long-term stability is achieved. The THF lasers operate in a wavelength region from 2100 to 2200 nm, which is typically dedicated to HDF lasers. With 262 W of output power for an emission wavelength of 2100 nm, the highest output power is achieved for a THF in general. Compared to HDF lasers, only Hemming et al. developed a more powerful laser system with a laser power of 407 W. Compared to the 40 % slope efficiency of the in-band pumped HDF laser, the demonstrated 49 % slope of the THF laser lays an excellent foundation to surpass the power value by installing more powerful diodes. 500 W diodes are available having roughly the same delivery fiber as the 300 W diodes, showing the possibility of reaching a new high-power record. There are also other HDF laser systems, which showed a slope efficiency of 60 %, but the maximum output power was smaller than 150 W. This shows that the thermal load developed in a THF is comparable to that of the HDFs. Moreover, comparing the 79X nm to  $\geq 2.09 \mu\text{m}$  efficiency, the THF is superior since the TDF used for pumping a HDF can be accounted for by 60 %. This leads to an overall optical-to-optical efficiency of 36 % for the tandem pumped systems. Of course, it has to be mentioned that the difference in emission wavelength from the investigated THF laser to the aforementioned HDF is 20 nm. The impressive result from Anderson et al. with 450 W at 2.11  $\mu\text{m}$  out of a TDF is not reached in terms of output power, but the efficiency is comparable. For an emission wavelength of 2.2  $\mu\text{m}$ , the THF can outperform current results by more than one order of magnitude and a new benchmark for power scaling close to the lasing edge of rare-earth doped silica fiber laser is set.

After a good free-space laser operation has been proven, the first step towards an all-fiber laser is already completed. With a slope efficiency of 47 % and output power of > 100 W, the laser is directly comparable to a high-power holmium system, which also operates at 2.12  $\mu\text{m}$ . Despite shifting the emission wavelength by 20 nm and going all-fiber, the slope efficiency drops negligible. This shows that the fiber is efficiently operated using a well-optimized laser setup. A good basis for further power scaling in CW operation is created and will be further used for pulsed laser operation.



## 5 Q-Switched Laser Operation

After investigating the THF in CW operation, this chapter focuses on the operation in the pulsed regime, more precisely in Q-switched operation. As for the CW operation, the Q-switching experiments are performed for different wavelengths spanning from 2050 nm to 2200 nm, covering the potential emission range of the THF. Thereby, different Q-switching regimes are addressed. For the Q-switching experiments at 2050 nm and 2090 nm, the fiber laser is operated at the gain maximum for each investigated setup. These lasers are potential sources for pumping an OPO to shift the high-power radiation further into the MWIR spectral range. Therefore, average power values of about 50 W are targeted in the beginning, being enough for pumping a linear OPO cavity with a  $\sim 40$  W damage threshold for the necessary isolator stage. Concerning the intended application, both lasers are realized with linearly polarized laser output. At 2130 nm, the fiber laser is operated slightly off the gain maximum, whereas at 2200 nm, the THF laser is pulsed far away from the gain maximum. For both cases, the main goal is to estimate potential pulse energies, pulse durations, and pulse peak powers. No direct application is intended. Therefore these wavelengths are investigated in a lower power regime and randomly polarized.

The fiber lengths are roughly chosen according to the fiber lengths investigated in Chapter 4, which have shown to enable good average power scaling even if this might not feature the best pulse energies. Setup limitations and the performance influences of different setup components are investigated to build an ideal pump source for nonlinear frequency conversion in the upcoming chapter. The chapter starts with an overview of state-of-the-art nanosecond pulsed laser sources with an emission in the long-wavelength  $2\ \mu\text{m}$  region (Section 5.1). Section 5.2 gives an overview of the Q-switched laser setup, particularly a brief introduction to an AOM, the intra-cavity device used to generate laser pulses. In the following, Q-switched results are presented at 2050 nm, 2090 nm, 2130 nm, and 2200 nm from Section 5.3 to Section 5.6. The chapter closes with a summary and conclusion in Section 5.7.

## 5.1 State-of-the-Art Nanosecond Pulsed Systems

To classify the following experimental Q-switching results, this chapter gives a brief overview of state-of-the-art nanosecond pulsed laser systems in the long-wavelength 2  $\mu\text{m}$  regime. However, literature containing pulsed lasers with an emission  $\geq 2.1 \mu\text{m}$  is very rare. Within this review, the main interest is put on actively Q-switched lasers and MOPA systems. Other systems like gain-switched and passively Q-switched laser sources are omitted. Most of the presented lasers also target nonlinear frequency conversion as an application. The review focuses on laser sources delivering high pulse energies, peak powers, and average output powers. Relevant literature is summarized in Tab. 5.1. Within the table, the literature values are sorted by technology and listed according to the emission wavelength.

Q-switching is one of the most compact methods to generate pulsed laser radiation in the nanosecond regime, relying on a low-complexity setup. The task is to maximize the extractable pulse energy [45]

$$E_p = \frac{1}{2} h\nu_s AL (\langle \Delta N \rangle_i - \langle \Delta N \rangle_f) = h\nu_s \underbrace{\frac{A}{\sigma_+(\lambda_s)}}_{=E_{\text{sat}}} (\ln G_i - \ln G_f). \quad (5.1)$$

The saturation energy  $E_{\text{sat}}$  is a measure for the extractable energy. Referring to Eq. (5.1), there are different ways of optimizing the pulse energy.

One way of maximizing the pulse energy is an engineering approach by improving the final and initial inversion, which are highly influenced by the cavity parameters. With increasing pulse energies and pulse peak power, standard SMFs have reached their scaling limits due to uprising fiber nonlinearities. These fiber nonlinearities arise from the third expansion term of the nonlinear polarization referred to as  $\chi^{(3)}$ -nonlinearities and are highly dependent on the fiber length and the pulse intensity [140]. Various  $\chi^{(3)}$ -mechanisms lead to a significant spectral broadening and a pulse distortion in pulsed laser operation, decreasing the laser performance. Therefore, the standard fibers are currently LMA fibers [64].

To the best of the author's knowledge, there are no actively Q-switched silica fiber lasers emitting beyond 2.1  $\mu\text{m}$  [27]. Also, there are no actively Q-switched  $\text{Ho}^{3+}$ -doped silica fiber lasers, and actively Q-switched THF lasers are rare. In 2008 Eichhorn et al. demonstrated a randomly polarized actively Q-switched THF laser with average output powers up to 12.3 W based on a 20/300  $\mu\text{m}$  DCF [141]. Pulse energies up to 226  $\mu\text{J}$  and pulse widths as short as 45 ns were generated with emission wavelengths up to 2072.7 nm.

This system was improved by Dalloz et al. in 2019 with an average output power of 55 W at a RR of 200 kHz [142]. The linearly polarized laser was also based on a 20/300  $\mu\text{m}$  DCF and delivered 720  $\mu\text{J}$  pulses, an average output power of 28.5 W, and pulse durations of 45 ns. An  $M^2$  of 1.7 was measured, and the emission wavelength was 2090 nm. So far, this is the most powerful Q-switched THF laser. The fiber was equipped with end caps as essential intra-cavity elements to prevent critical fiber end damage. Fiber nonlinearities are not explicitly mentioned to impact the laser performance for the pulsed laser systems cited above. However, fiber nonlinearities become a serious issue for higher intensities, even for the used LMA fibers.

This performance degradation due to fiber nonlinearities has already been shown by TDF lasers, where most of the literature of 2  $\mu\text{m}$  Q-switched fiber lasers concentrates on. The emission wavelengths of these lasers are mainly restricted to the shorter part of the 2  $\mu\text{m}$  region. Recently, Schneider et al. presented their results of pulse energy scaling of Q-switched TDF lasers starting with pulse energies of 800  $\mu\text{J}$  at 2044 nm and 2050 nm out of 20/300  $\mu\text{m}$  double-clad TDFs [143, 144]. At the moment, these randomly polarized laser sources deliver pulse energies close to 1 mJ at 2050 nm with pulse peak powers of 20.5 kW and pulse energies of 720  $\mu\text{J}$  at 2090 nm with pulse peak power of 6.5 kW [145]. These high pulse energies, which result in high pulse peak powers, have been achieved by carefully managing the parasitic lasing using selective feedback for the laser wavelength by an OC FBG. The aforementioned pulsed TDFs show high pulse energy and peak powers, but all these lasers were operated below 20 W and when it comes to longer emission wavelengths at 2090 nm the performance of the TDF decreased.

Another way of maximizing the pulse energy besides optimizing the possible initial and final inversion is to increase the core size of the active fiber and, consequently, the saturation energy  $E_{\text{sat}}$ . These large core fibers (LCFs) are typically photonic crystal fibers (PCFs) since standard step-index fibers are almost impossible to manufacture due to a minimal refractive index difference of core and cladding for single-mode laser output. An essential advantage of LCFs is a highly increased power threshold for nonlinearities, which is essentially required due to the increased pulse energies. Using a 81  $\mu\text{m}$  core diameter rod-type large pitch fiber, pulse energies up to 2.4 mJ and pulse peak powers of 150 kW were achieved with an average output power of 33 W for an unpolarized laser version [146]. The TDF laser had an emission wavelength below 2.0  $\mu\text{m}$ .

LCFs have shown that they can provide high energies but also have some drawbacks. For example, a dramatically increased lasing threshold since the higher saturation energy is linked to a higher saturation intensity and via Eq. (2.19) directly to the threshold power. In addition, there is a lack of literature with similar results of PCF at longer wavelengths.

Compared to actively Q-switched systems, where pulse energy, pulse duration, and pulse shape are inherently connected, MOPA systems allow a free choice of pulse shape while scaling the laser output power. The higher degree of freedom comes at the price of a much larger and more complex system. MOPA systems have been realized successfully at wavelengths above 2050 nm and even above 2100 nm. For example, Hemming et al. realized a linearly polarized MOPA based on an electro-optically Q-switched  $\text{Ho}^{3+}$ :YAG master oscillator emitting at 2090 nm [147]. The amplifier consisted of a 45/250  $\mu\text{m}$  large mode TDF. The MOPA delivered 2.25 mJ with an average power of 45 W and a pulse duration of 20 ns leading to pulse peak power of 100 kW. Whereas this amplifier system was free-space, Holmen et al. realized a three-stage all-fiber amplifier system with an emission wavelength of 2108 nm [148]. The emission from a diode was amplified by multiple HDF amplifiers up to an average output power of 5.2 W with pulse peak powers of 11 kW. As a significant advantage to the inherent Gaussian-like beam shape of Q-switched laser sources, an almost square-like pulse can be generated with regard to the use as a pump source for nonlinear frequency conversion. Another nanosecond pulsed MOPA system with average output powers close to 100 W was realized by Yao et al. [149]. The thulium-holmium hybrid MOPA was emitting at a wavelength of 2116 nm with pulse energies of 0.6 mJ. The overview shows that both technologies are currently investigated and have their advantages and disadvantages. MOPA systems can be optimized according to the desired output pulse shape. They can exhibit very high pulse energies and average output powers, but the scaling of both quantities is rarely shown. Moreover, power scaling in combination with pulse energy scaling is quite tricky and complex. There are often more than ten fiber components [148] that need to handle specific power and energy levels, and most of them cannot be bought off-the-shelf. In addition, careful management of fiber nonlinearities is highly required within these systems due to long interaction lengths.

By contrast, Q-switched lasers are characterized by simple setups which have shown potential with pulse peak powers up to 20 kW out of 20  $\mu\text{m}$  core fibers. However, the process and output characteristics are restricted to the Q-switch fundamentals resulting in a lack of freedom regarding pulse shape, pulse energy, and pulse duration. In addition, wavelengths above 2.09  $\mu\text{m}$  have not been addressed so far, and the average power scaling in combination with high pulse energies has not been shown.

Therefore, this chapter aims to provide an overview of possible Q-switching for an emission wavelength of  $\geq 2.09 \mu\text{m}$ . The THF is predestinated for this due to a more efficient operation at longer wavelengths than TDFs and still relies on a simple diode pumping scheme and a very compact and straightforward setup.

Table 5.1: State-of-the-art nanosecond pulsed laser sources in the long-wavelength 2- $\mu\text{m}$  region.

<b>Q-Switched Fiber Lasers</b>								
Active Fiber	Core Diameter	Operation Wavelength	Linearly Polarized	Average Power	Pulse Peak Power	Pulse Energy	Pulse Duration	Reference
TDF	81 $\mu\text{m}$	< 2000 nm	no	33 W	150 kW	2.4 mJ	15 ns	[146]
THF	20 $\mu\text{m}$	2017.8 nm 2072.7 nm	no	2.3 W 12.3 W	4.7 kW 2 kW	230 $\mu\text{J}$ 130 $\mu\text{J}$	45 ns 58 ns	[141]
TDF	20 $\mu\text{m}$	2050 nm 2090 nm	no	< 20 W	20 kW 6.5 kW	960 $\mu\text{J}$ 720 $\mu\text{J}$	44 ns 105 ns	[145]
THF	20 $\mu\text{m}$	2090 nm	yes	55 W 28.5 W	2.8 kW 15.3 kW	275 $\mu\text{J}$ 720 $\mu\text{J}$	100 ns 45 ns	[142]

<b>Nanosecond Pulsed MOPA Systems</b>								
Master	Amplifier	Operation Wavelength	Linearly Polarized	Average Power	Pulse Peak Power	Pulse Energy	Pulse Duration	Reference
Q-switched Ho <sup>3+</sup> :YAG	1 amplifier stage 45 $\mu\text{m}$ core HDF	2090 nm	yes	45 W	106 kW	2.25 mJ	20 ns	[147]
Diode laser	3 amplifier stage Ho <sup>3+</sup> based	2108 nm	yes	5.2 W	11 kW	520 $\mu\text{J}$	50 ns	[148]
Hybrid Tm <sup>3+</sup> :Ho <sup>3+</sup> self-pulsing	2 amplifier stage TDFs and HDFs	2116 nm	no	99.1 W	1.91 kW	615 $\mu\text{J}$	322 ns	[149]

## 5.2 Setup for Q-Switched Laser Operation

For operating the THF laser in a pulsed mode, the setup for CW laser output (Fig. 4.11) is slightly adapted. The revised setup is displayed in Fig. 5.1. An AOM [150, 151] is placed intra-cavity to modulate the cavity losses. Due to a modulation speed in the (lower) kHz regime, the setup is Q-switched. For Q-switching, the AOM is placed between the HR mirror and the according fiber end since excluding the HR from the cavity introduces more losses than excluding the OC. In the case of fiber lasers, this OC reflectance is typically below 10%. During the experiments, it has turned out that the 20  $\mu\text{m}$  core fiber is prone to suffer from a self-mode-locking when approaching extreme conditions like high pulse peak powers, which is also reported in [141]. The Q-switched fiber laser is then hardly adjustable. Therefore, most experiments are performed with the 18  $\mu\text{m}$  core fiber, which shows a more stable operation.

The schematic of an AOM is depicted in Fig. 5.2. The working principle of an AOM is based on the elasto-optic effect, or more precisely, the acousto-optic effect [72, 150, 151]. A transducer sends an acoustic wave through the acousto-optic material roughly perpendicular to the propagation direction of the laser beam. The acoustic wave produces strain, which leads to a local change in the material's density and a local change in the refractive index. The acoustic wave acts as a diffractive index grating traveling through the crystal.

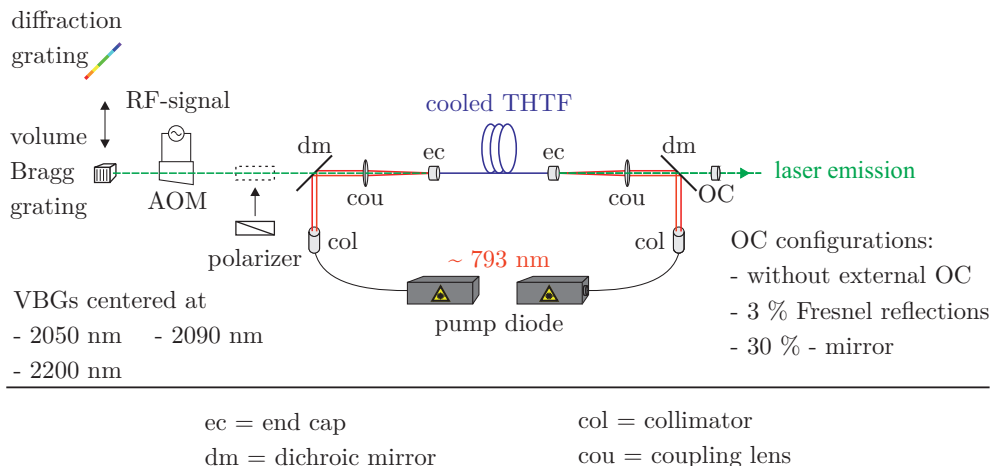


Figure 5.1: Laser Setup for Q-switched operation. For Q-switching, an AOM is placed between the HR and the active fiber end.



The acoustic wave is received by an absorber to avoid interference by the back-reflected wave. To further minimize this effect, the absorber is angled so that a partially reflected wave leaves the crystal from the side surface. Different operation regimes exist depending on the beam size and the interaction length of the beam and the acoustic wave. The Rahman-Nath regime describes a short interaction length of the laser beam and the index grating [45, 150]. The laser beam is split into multiple diffraction orders with the main power in the 0<sup>th</sup> order. This effect is similar to a multiple-slit experiment and cannot be used for Q-switching. For Q-switching, the AOM is operated in the Bragg regime [45, 150] for a sufficient large interaction of the index grating and the laser beam. In this case, the process is similar to the scattering of waves from a crystal lattice. A beam entering the AOM with the Bragg angle is efficiently diffracted into the first order with a deflection of two times the Bragg angle. The frequency of the diffracted beam is shifted by the frequency of the sound wave. With this method, a measured diffraction efficiency of > 85 % is reached, leading to an efficient suppression of lasing.

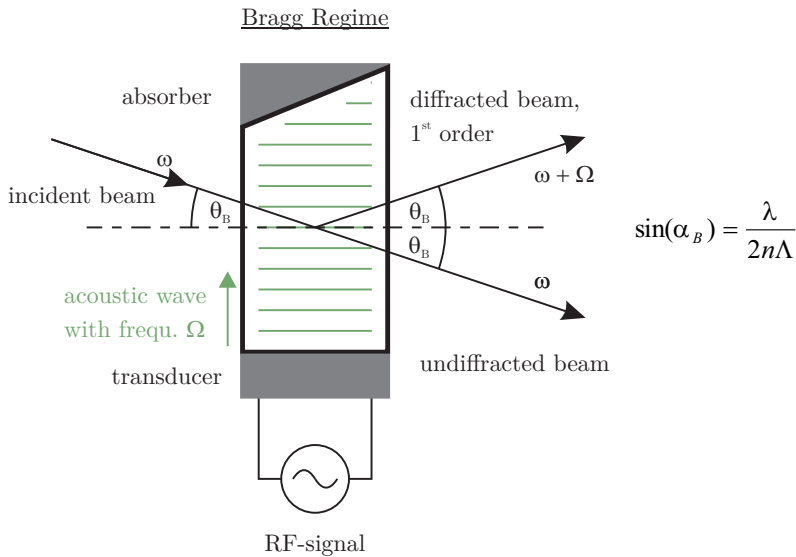


Figure 5.2: The figure shows the schematic of an AOM. The Bragg regime applies for a large input beam size and a long propagation through the AOM. A beam entering the AOM with the Bragg angle is efficiently diffracted into the first order with a deflection of two times the Bragg angle.

### 5.3 Q-Switching Results at 2050 nm

First Q-switched experiments, like in CW operation, are performed for a laser emission at 2050 nm and are published in [152, 153]. The active fiber is the 18  $\mu\text{m}$  core THF with a length of 5 m. The cavity is comprised of a VBG centered at 2050 nm on one side and a FTES acting as the OC on the other side of the fiber. Since this laser is initially intended to be used directly as a pump source for nonlinear frequency conversion utilizing birefringent phase matching, the laser is realized linearly polarized, aiming to reach roughly 50 W of average output power. For a pump power of 180 W, the laser delivers 53.4 W in CW mode.

Figure 5.3 shows the average laser output power plotted versus the modulation frequency or pulse RR  $\nu_r$ . The starting pulse RR is 150 kHz. At this frequency, the average output power drops to 52.1 W. The pulse RR is decreased towards 63 kHz accompanied by a further decrease of the average output power down to 48.1 W.

According to the theory part of Q-switching (see Section 2.1.4), the average laser output power is assumed to be constant, but the depicted power values indicate the opposite. There are at least two contributions to this power drop. Firstly, fiber lasers are comprised of a relatively long active region.

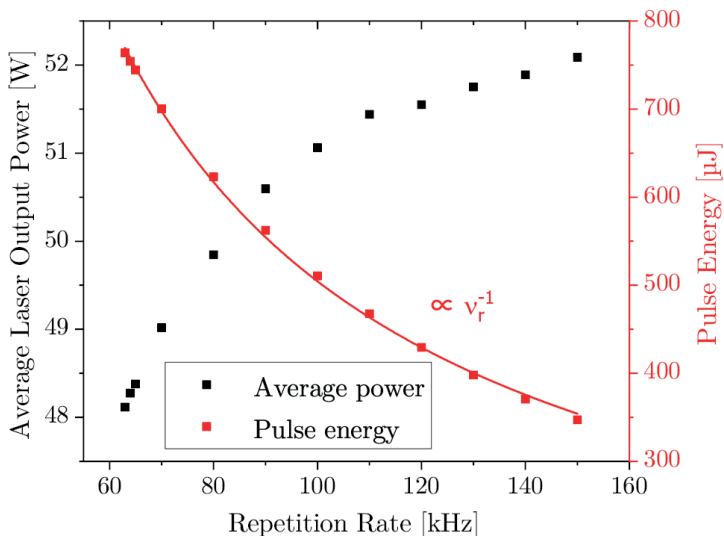


Figure 5.3: Average laser power and pulse energy plotted versus the pulse RR. The laser is operated in Q-switched mode with a constant pump power of 180 W at an emission wavelength of 2050 nm.

During the pumping phase, spontaneous emission, in combination with the waveguiding effect, can relax a substantial amount of excited electrons along the active fiber path. This ASE is equally emitted from both sides, increasing with decreasing pulse RRs. Secondly, approaching shorter RRs, the laser output spectrum changes due to fiber nonlinearities, introducing additional cavity losses. This will be discussed in more detail later on.

The calculated pulse energies (by dividing the average measured output power by the RR) versus the pulse RR are also depicted in Fig. 5.3. The pulse energy scales inversely with the RR, as expected from the theory. Pulse energies from 350  $\mu\text{J}$  up to 760  $\mu\text{J}$  are determined.

Figure 5.4 shows the determined pulse widths and peak powers. The pulses shapes are similar to Gaussian pulses, and the pulse width scale linearly with the pulse RR. For a RR of 63 kHz, pulse durations as short as 45.6 ns are determined. This leads to pulse peak powers of up to 15.7 kW. The corresponding pulse is depicted on the left-hand side of Fig. 5.5. The pulse peak power  $\hat{P}$  can be calculated according to the equation [154]

$$\hat{P} \approx 0.94 \frac{E_p}{\Delta t_p}. \quad (5.2)$$

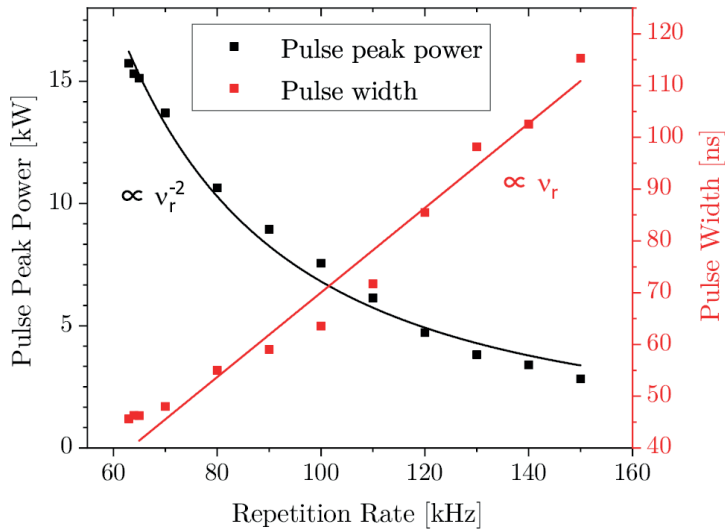


Figure 5.4: Pulse duration and the pulse peak power plotted versus the RR. The laser is operated in Q-switched mode with a constant pump power of 180 W at an emission wavelength of 2050 nm.

The prefactor refers to the Gaussian pulse shape. Due to the dependencies of  $\Delta t_p \propto \nu_r$  and  $E_p \propto \nu_r^{-1}$ , it holds  $\hat{P} \propto \nu_r^{-2}$ . We assume a typical Q-switching behavior as long as the measured data show these dependencies.

The right-hand side of Fig. 5.5 shows the beam quality measurement for the highest pulse energy. Compared to the CW values, the beam quality factor  $M^2$  is slightly increased, but with a value of 1.19 in the x-direction and 1.14 in the y-direction, the beam is still close to being diffraction limited.

So far, the measured optical characteristics of the Q-switched fiber laser at 2050 nm are excellent for nonlinear frequency conversion. Compared to state-of-the-art Q-switched fiber lasers in the nanosecond regime, the realized pulsed fiber laser shows high pulse peak powers, high average output powers, and good beam quality. However, the emission spectrum has been left out so far, being one of the critical parameters determining the efficiency of nonlinear processes. Figure 5.6 shows the emission spectrum of the fiber laser, one in CW operation (green line) and one in Q-switched operation (blue line) at the highest pulse energy. The FWHM increases from 54 pm to 290 pm. This broadening effect is caused by fiber nonlinearities. An interplay of different nonlinear processes is taking place, and the actual degree of nonlinearities can only be determined if an appropriate amount of power is launched into the OSA. For the Q-switched measurements at 2050 nm, the spectrum is measured overcautiously to prevent any damage to the optical spectrum analyzer. Therefore, a deeper analysis and explanation of these fiber nonlinearities will be performed in the following section.

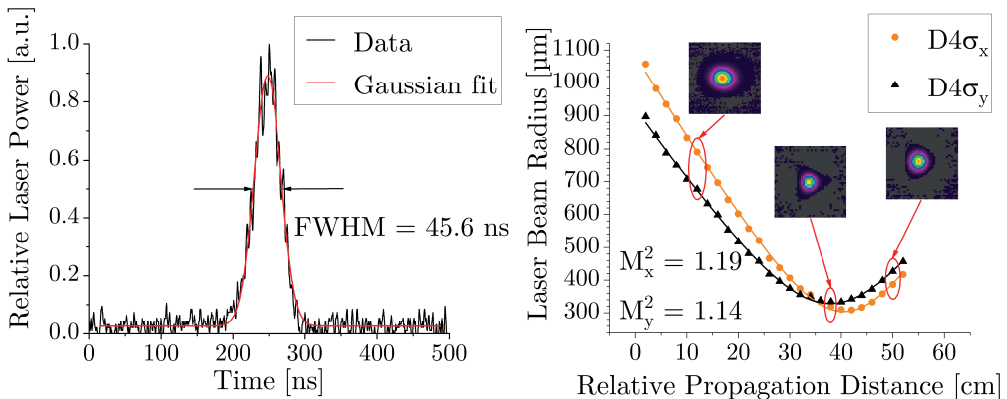


Figure 5.5: Laser characteristics in Q-switched operation at the shortest possible RR and a constant pump power of 180 W. Left: Gaussian-like pulse shape with a FWHM of 45.6 ns. Right: Beam quality measurement with an  $M^2_{x/y}$  of 1.19/1.14.

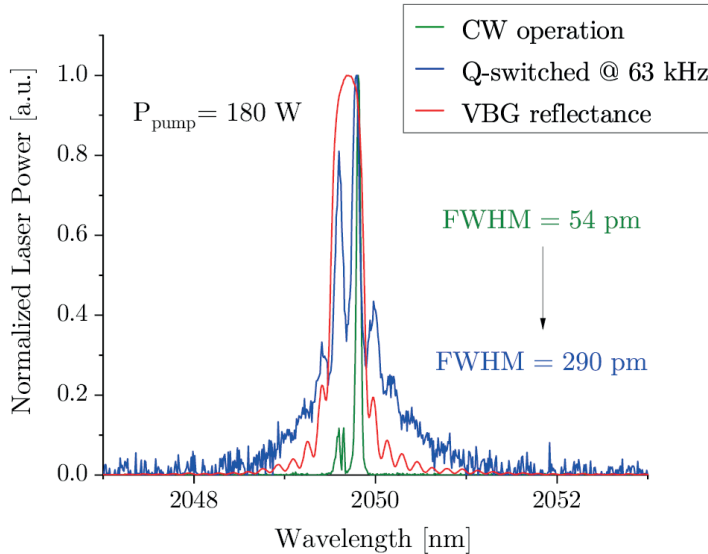


Figure 5.6: The output spectrum of the laser operated in CW mode is compared to the output spectrum of the same laser operated for the highest output energy in Q-switched mode. The operation wavelength is 2050 nm. An obvious broadening of the spectrum is visible.

However, this spectral broadening is one of the reasons for the drop in average power when decreasing the pulse RR for a constant pump power. The VBG acts as a spectral filter. The reflection characteristics (red line) are added to the output emission spectrum. A certain spectral amount of the pulse passes the VBG and is not reflected. This means that the spectral power outside of the spectral reflectance bandwidth of the VBG visible in the output spectrum is generated within one fiber length (from the VBG to the OC). A deeper analysis of the laser spectrum is performed for the upcoming measurements.

## 5.4 Q-Switching Results at 2090 nm

In a second Q-switch experiment, the laser wavelength is shifted to 2090 nm. With a fiber length of 5.5 m (18  $\mu\text{m}$  core fiber), an OC reflectance of 3%, and a VBG centered at 2090 nm, the realized laser operates at the gain maximum and lays the foundation for average power scaling. The red-shifted emission wavelength justifies using the codoped fiber compared to the 2050 nm experiment. The laser is realized linearly polarized by inserting a polarizer in the cavity.

The previous section shows that the targeted average output power of 50 W has not been reached due to a substantial power drop in Q-switched operation. Therefore, a larger initial CW power value is targeted this time to ensure staying above 50 W, also in Q-switched operation. Therefore, an incident pump power of  $\sim 170$  W is applied leading to a CW laser output of 65 W. Figure 5.7 shows the average output power, the pulse energy, and the pulse width as a function of the RR. For repetitive Q-switching, the loss modulation is started at a RR of 150 kHz down to 83 kHz. During this step, the average output power decreases from 59.4 W to 54.2 W. This decrease in average output power can be explained later on when the spectrum is investigated more carefully. The measured output powers result in pulse energies from 400  $\mu$ J to 650  $\mu$ J. While decreasing the pulse RRs the pulse durations decrease from 109 ns to 54 ns at a RR of 100 kHz. The otherwise Gaussian-like pulse starts to break up below 100 kHz as depicted in Fig. 5.8. Determining a FWHM or calculating a pulse peak power is omitted. The pulse looks Gaussian but is superimposed with a set of equally spaced, stronger, shorter pulses. The pulses have a spacing of  $\sim 12$  ns. As a comparison, the Gaussian pulse shape at a RR of 100 kHz is depicted on the left-hand side, and the heavily modulated pulse at a RR of 83 kHz is displayed on the right-hand side of Fig. 5.8. This behavior is attributed to the increase of non-negligible fiber nonlinearities.

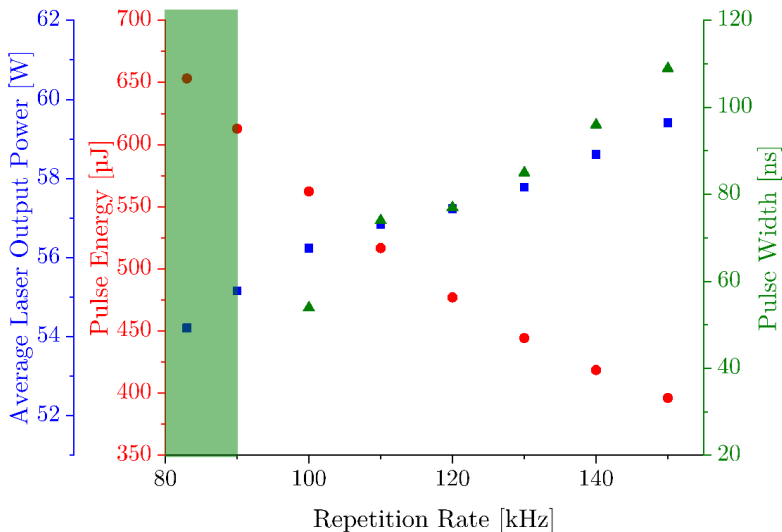


Figure 5.7: Average output power, pulse energy, and pulse duration plotted versus the RR for Q-switched operation at 2090 nm. The laser was operated at a constant pump power of 170 W. The green highlighted RR range marks a region where fiber nonlinearities strongly distort the otherwise Gaussian-like pulse shape.

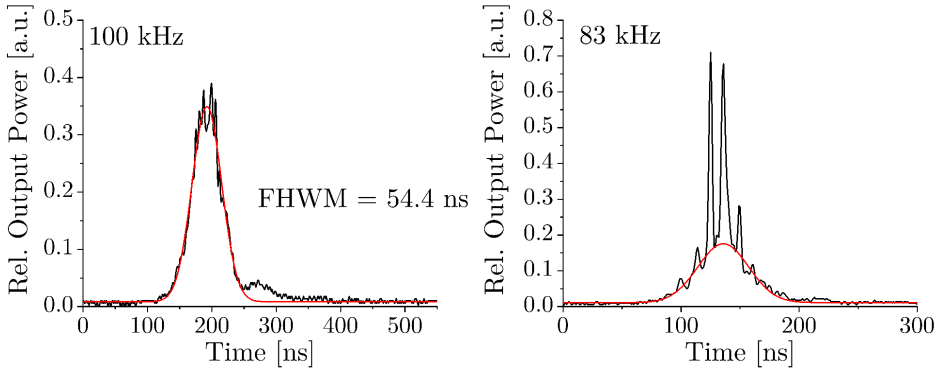


Figure 5.8: Comparison of different pulse shapes for Q-switched operation at 2090 nm. Left: Gaussian-like pulse shape. Right: Gaussian pulse shape with a superposition of multiple shorter and stronger pulses, probably due to increasing fiber nonlinearities.

The analysis of the emission spectrum of the pulsed laser source supports this. Compared to the measurements at 2050 nm, much more power is launched into the optical spectrum analyzer. The normalized spectra for different pulse RRs and in CW operation are displayed in Fig. 5.9. The investigated wavelengths range from 2000 nm to the limit of the spectrum analyzer at 2400 nm. The black curve shows the spectrum in CW operation. There is no ASE, parasitic lasing, or another signal visible except for the narrow emission line at 2090 nm. However, in pulsed operation, the spectrum starts to broaden. First, at high RRs, there is an almost symmetrical broadening around the signal center wavelength. Then, with decreasing RR, the symmetrical content increases, and more signal establishes mainly towards longer wavelengths. At the lowest repetition rate, there is almost a constant signal ranging from 2100 nm up to 2400 nm. Well-pronounced sidelobes evolve symmetrically from the left and right of the primary signal. These sidelobes are attributed to a nonlinear effect called modulation instabilities (MI) [140]. Another nonlinear effect superimposed to MI is self-phase modulation (SPM) [140, 155]. Due to an intensity-dependent refractive index (Kerr effect), the pulse induces an intensity-dependent phase shift to itself. This leads to a symmetrical frequency generation around the signal. A deeper insight into fiber nonlinearities is omitted since, for this thesis, it is only important to know that these exist and can impact fiber laser performance. No mitigation strategy can be used for Q-switched fiber lasers besides decreasing the intensity by increasing the core size or shortening the fiber. The nonlinearities are a function of the pulse peak power and the interaction length. A basic and more detailed discussion can be found in [140].

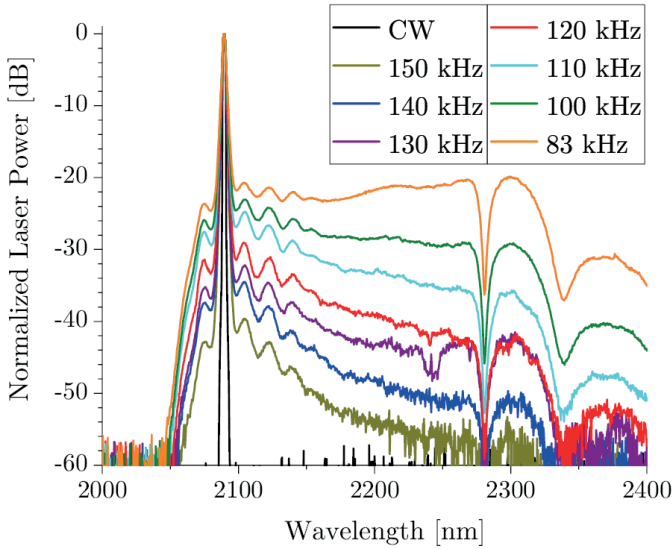


Figure 5.9: Comparison of different laser emission spectra for CW operation and Q-switching at 2090 nm plotted from 2000 to 2400 nm. Laser optics can slightly distort the emission spectra since the optics are not designed to cover a wavelength of more than 400 nm, which explains the slightly monotonically increasing output power for wavelengths above 2150 nm for a RR of 83 kHz.

The spectrum shown in Fig. 5.9 is not symmetrically broadened as indicated by the mentioned nonlinear mechanism but is heavily one-sided towards longer wavelengths. The transmission and reflection characteristics of the laser optics sharply cut the short wavelength edge. At the long-wavelength side, there are well-pronounced spectral transmission dips at 2280 nm and at 2340 nm, resulting from the transmission characteristics of the polarizers. In addition, there is substantial gain inside the fiber for longer wavelengths featuring a stronger amplification.

Figure 5.10 shows a close-up of the spectra around the original signal. In CW operation, the signal has a FWHM of 74 pm and a 20 dB-width of 0.88 nm. In Q-switched operation for a RR of 83 kHz, the FWHM roughly remains constant with a value of 0.75 nm but the 20 dB-width strongly increases to 8.32 nm. The spectrum shows four peaks, which are distinguishable in the CW regime down to 20 dB, however in Q-switched operation, the four smear out up to a level of 5 dB. The nonlinear effects around the signal are intrinsically more pronounced and supported by the reflection characteristics of the VBG. The signal is filtered at the VBG, and the part within the reflectance is seeding further nonlinearities on the backward propagation.



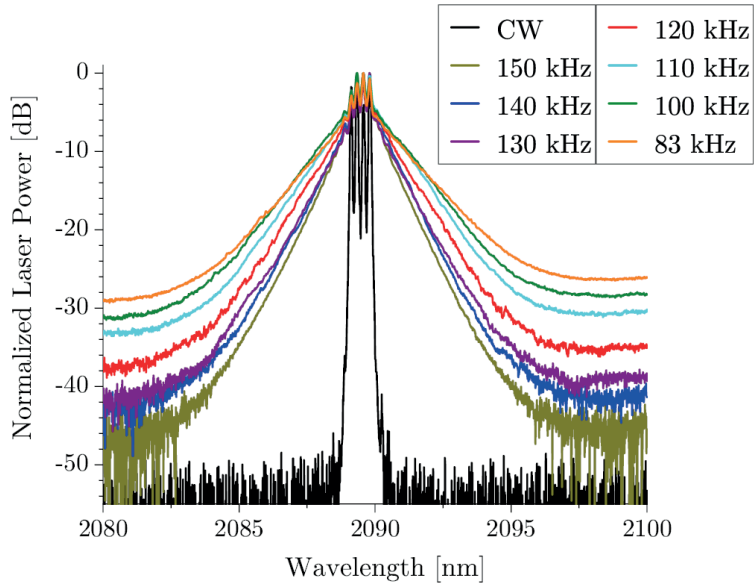


Figure 5.10: Comparison of different laser emission spectra for CW operation and Q-switching at 2090 nm plotted from 2080 to 2100 nm.

This reflection characteristic of the VBG is also the reason for the power loss of the average laser output power in Q-switched operation. Figure 5.11 shows the reflectance characteristic of the VBG, the measured normalized output spectrum at 83 kHz, and the transmitted normalized spectrum behind the VBG. The transmitted spectrum shows a dip in the center related to the reflectance of the VBG and is modulated by an interference effect of the four peaks visible in the output spectrum. The transmitted spectrum already indicates that the VBG does not reflect a significant amount of power. Additionally, measuring the transmitted power behind the VBG quantifies the strong spectral broadening. The measured transmitted power of 5.8 W at a RR of 83 kHz shows that a non-negligible amount of signal is directly converted into the direct vicinity of the spectrum and is not anymore covered by the reflection of the HR.

A strong signal broadening, pulse distortion, setup-related pulse energy, and average power drop represent an explicit limitation for Q-switched fiber lasers and show that the fiber length must be carefully selected. Choosing the fiber length according to the best results in CW operation is deceptive. The optimization of average power and pulse energy scaling are not decoupled. Also, LMA fibers come to their limit in mitigating fiber nonlinearities.

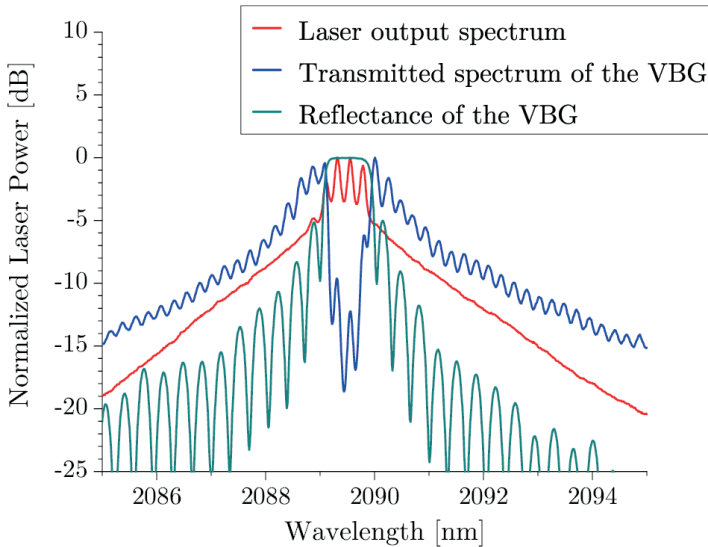


Figure 5.11: Comparison of the laser output spectrum, the spectral reflectance of the VBG, and the transmitted spectrum by the VBG for Q-switching at an emission wavelength of 2090 nm. This shows the strong spectral broadening of the laser signal and the filtering effect of the VBG leading to a strong power drop of the average output power in Q-switched operation.

## 5.5 Q-Switching Results at 2130 nm

For the Q-switched operation described at 2.05  $\mu\text{m}$  and 2.09  $\mu\text{m}$ , the setups are operated more or less at the gain maximum of each realized design. In the next step, the emission wavelength is red-shifted towards a wavelength of 2130 nm. Increasing the fiber length or increasing the reflectance of the OC would shift the gain maximum towards longer wavelengths, which must be avoided for two reasons. First, the cavity lifetime of the signal will be increased, leading to longer pulse widths, and since the main goal is to achieve high pulse peak powers, this would have the opposite effect. Second, the interaction length of the signal and fiber would be increased, leading to an increase in nonlinearities, which must also be avoided. Therefore, the 18  $\mu\text{m}$  fiber is used with a length of 5.5 m as for the 2090 nm results, and the experiments are not performed at the gain maximum. The cavity is comprised of a 3% OC reflectance and a diffraction grating since no VBG is available at this wavelength.

An average laser output power of 30 W is targeted, and therefore the incident pump power is chosen as  $\sim 130$  W. Figure 5.12 shows the determined pulse energies, pulse durations, and pulse peak powers when decreasing the pulse RR for the constant pump power.

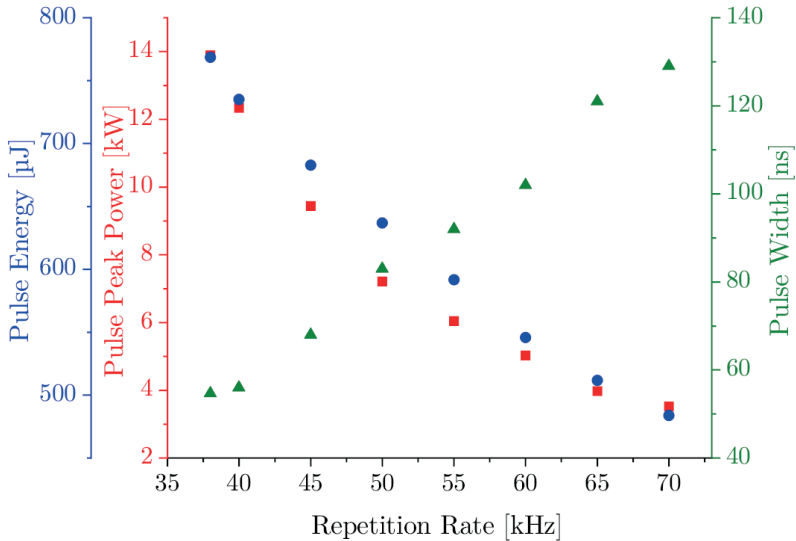


Figure 5.12: The graph shows the pulse energy and the pulse widths in Q-switched operation for an emission wavelength of 2130 nm. The setup, which is realized with a DG as an HR, is operated above 30 W of average output power. The calculated pulse peak power is also included in the graph.

The pulse RR is decreased from 70 to 38 kHz accompanied by a decrease of average output power from 33.8 to 29.2 W. A further decrease of the pulse RR or an increase in pump power will result in reaching threshold inversion for parasitic lasing and an additional laser emission at 2050 nm. Pulse energies up to 770  $\mu\text{J}$  are generated with a pulse duration as short as 52 ns leading to a pulse peak power of 13.9 kW.

A broader spectrum is reflected from the HR compared to the previous Q-switched laser experiments because the filtering effect, which is inherent to the VBG, is not that prominent for the DG. Figure 5.13 shows the measured spectra for various RRs. For a RR of 37 kHz, parasitic lasing is observed, which is depicted by the red curve. A supercontinuum rises when the pulse peak power is increased. The spectra also show the typical transmission characteristics of the intra-cavity dichroic mirrors, which reflect the signal at 2280 nm and 2340 nm. The left-hand side of Fig. 5.14 shows a close-up of the spectrum measured for a RR of 38 kHz. Compared to the previous Q-switched results, the emission spectrum is very broad and shows multiple equidistant peaks at the center of the emission wavelength. A FWHM of 1.3 nm and a 20 dB-width of 15.5 nm is determined. The right-hand side of Fig. 5.14 shows a pulse shape for the maximum pulse energy at the smallest RR. The pulse shape is close to a Gaussian and shows a FWHM of 54.7 ns.

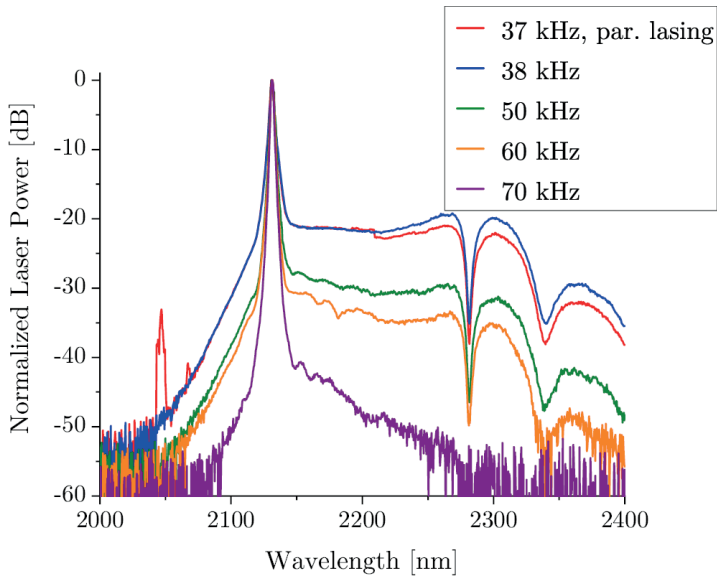


Figure 5.13: The figure shows the emission spectra for a constant pump power of 130 W and different repetition frequency in Q-switched laser operation. The signal wavelength of the laser is 2130 nm. With a decreasing RR, the pulse peak power increases, and by that, the fiber nonlinearities. Parasitic lasing at 2050 nm occurs when the pulse RR is below 37 kHz. The small power drop at 2.2  $\mu\text{m}$  for the 37 kHz is attributed to a measurement error.

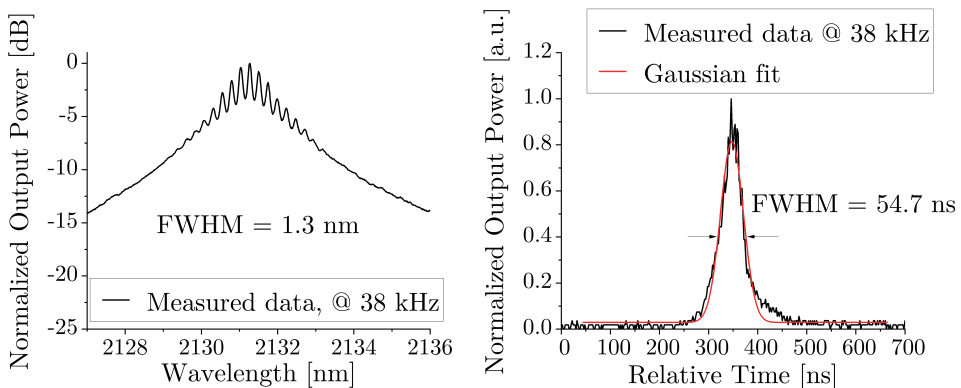


Figure 5.14: Laser characteristics in Q-switched operation for an emission wavelength of 2130 nm and the maximum pulse energy. Left: The close-up emission spectrum shows well-pronounced peaks around the main wavelength of 2120 nm. Right: The pulse shape resembles a Gaussian with a FWHM of 54.7 ns.

The Q-switched results at 2130 nm show that similar pulse energies compared to 2090 nm can be achieved with slightly longer pulse durations. However, the Q-switched laser emitting at 2130 nm is randomly polarized. Typically, linearly polarized Q-switched fiber lasers show a worse performance compared to a randomly polarized version. The longer pulses measured at 2130 nm may result due to a smaller gain compared to the shorter emission wavelengths.

## 5.6 Q-Switching Results at 2200 nm

The experiments in Chapter 4.2.5 show that laser emission with significant laser output power is possible at the edge of the transparency of silica despite vanishing small gain cross sections. The realization of a pulsed laser by Q-switching in this regime is investigated as a last experiment. For this experiment, the 20  $\mu\text{m}$  core fiber is used with a fiber length of 4.65 m. Like in Chapter 4.2.5, a 30% OC and a VBG centered at 2200 nm comprise the cavity. A few predictions can already be made ahead, taking the previous Q-switched results at shorter wavelengths as a reference. Due to an increase of the OC reflectance from 3% to 30%, the cavity lifetime increases directly linked to an increase of the pulse duration in Q-switched operation. Additionally, inserting a 30% broadband reflector decreases the achievable initial inversion since the threshold inversion for parasitic lasing is lowered. Parasitic lasing supported by a cavity consisting of the 30% reflection on one side and the FTES on the other side is likely to appear.

The main goal of this experiment is not explicitly power scaling but to see if Q-switching is possible at all since the continuous-wave operation is already quite challenging. The starting point is set to a continuous-wave output power of 10.6 W. Figure 5.15 shows the pulse energies  $E_p$  and pulse durations  $\Delta t_p$  plotted over the pulse RR  $\nu_R$ . By decreasing the RR from 60 kHz to 35 kHz, the average output power decreased from 10.4 W to 8.9 W. The calculated pulse energies are therefore increasing from 170  $\mu\text{J}$  to 270  $\mu\text{J}$ . As expected, the pulse widths are relatively broad, starting with a FWHM of 558 ns down to 256 ns. Further decrease in RR is accompanied by the start of parasitic lasing at 2075 nm.

The left-hand side of Fig. 5.16 shows the measured spectra for various pulse RRs. As for the previous Q-switched experiments, fiber nonlinearities lead to the broadening of the laser output spectrum. In case of CW operation, three clearly distinguishably peaks are visible with a 3 dB-width of 600 pm and a 20 dB-width of 700 pm. The spectrum broadens in Q-switched operation with increasing pulse peak powers, and the three peaks smear out. At the minimum RR of 35 kHz, the 20 dB-width shows a base broadening of 2180 pm.

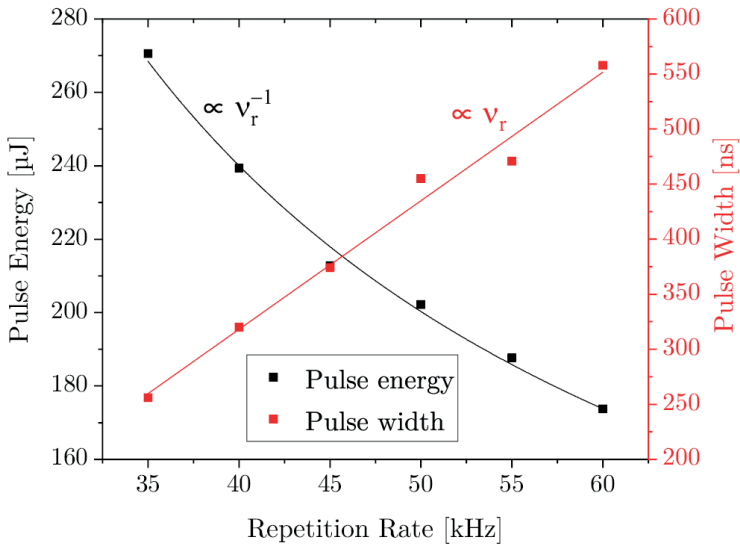


Figure 5.15: The graph shows the pulse energies and pulse durations plotted versus the pulse RR in Q-switched operation for an emission wavelength of 2200 nm.

With a maximum pulse peak power of 1 kW, the resulting intensity combined with the used fiber length is too low to generate visible MI and a strong supercontinuum content.

The right-hand side of Fig. 5.16 shows the pulse duration measured at a pulse RR of 35 kHz. So far, the measured pulse shapes are similar to a Gaussian. This situation also holds for a RR of 60 kHz. However, the leading edge becomes continuously steeper while decreasing the pulse RR. According to [48], the leading edge depends on the amplification present in the fiber. The larger the pump over threshold factor  $r$ , the steeper the leading edge. When passing the peak of the pulse, the inversion falls below the threshold inversion, and no amplification is possible anymore. Therefore, the trailing edge is roughly determined by the exponential decay based on the cavity photon lifetime [48]. However, an almost symmetrical pulse shape would indicate an  $r$  parameter of about 2. This would apply roughly to the previous Q-switched values.

These results show that Q-switching at 2.2  $\mu\text{m}$  is possible. However, the pulse widths are relatively long compared to the Q-switch experiments at shorter operation wavelengths. This is mainly due to the necessary high reflectance of the OC and its inherent high cavity photon lifetime, but there is space for improvement. One big problem is the broadband coating of the OC highly featuring parasitic lasing.

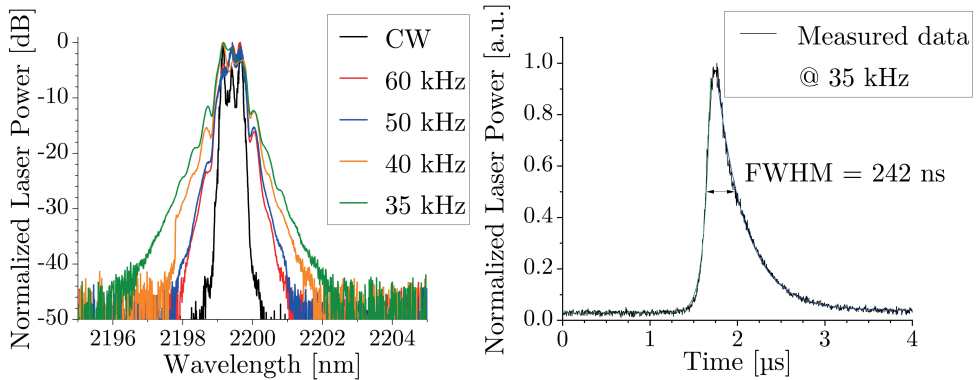


Figure 5.16: Left: The graph shows the emission spectra in CW operation and in Q-switched operation for different pulse RRs down to the limit of 35 kHz. Right: The figure depicts the pulse shape at a RR of 35 kHz, which shows a strong asymmetry of the leading and trailing edge.

By having a narrowband wavelength selective OC by adapting the coating or using an FBG, the threshold for parasitic lasing can be increased. If pulsed operation towards 2.2  $\mu\text{m}$  region is required, Q-switched THF lasers can be considered.

## 5.7 Conclusion

This chapter shows that Q-switching has been successfully established over a wide wavelength range from 2.05 to 2.2  $\mu\text{m}$ . To the best of the author's knowledge, the currently longest Q-switched silica fiber operation wavelength of 2090 nm [27, 142] is red-shifted by 110 nm for the first time, leading to an overlap with interesting atmospheric transmission bands. After it is shown in Chapter 4 that power scaling at an edge-wavelength of 2.2  $\mu\text{m}$  is possible, a first Q-switched fiber laser is realized at that wavelength. With 270  $\mu\text{J}$  per pulse, considerable pulse energies are achieved, but the setup-inherent long pulse widths of 242 ns lead to relatively low pulse peak powers of 1 kW. By decreasing the emission wavelength, special inversion management by a high OC reflectance is no longer required, and a low reflective OC is sufficient. This results in a substantially higher gain, accompanied by much shorter pulses and higher pulse energies. Therefore, at laser wavelengths from 2050 to 2130 nm high pulse peak powers up to 15 kW are shown even for the polarized laser versions. Current Q-switched THF laser sources are outperformed in pulse energy, pulse peak power, average output power, and higher spatial brightness (see Section 5.1).

Additionally, the presented results above an emission wavelength of 2050 nm justify the use of a THF and show the advantages of THFs compared to TDFs when it comes to Q-switching at this extended wavelength region.

However, the experiments also show that fiber nonlinearities already become a limiting factor for LMA Q-switched fiber lasers. The increased peak powers lead to significant spectral broadening and even pulse shape distortion, mainly with fiber lengths optimized for efficient average power scaling. System optimization toward efficient power scaling and high pulse energy at the same time is very challenging and is probably not possible. The Q-switched laser system must be optimized for a specific application.

Concerning the main application targeted, the experiments show that a suitable pump source for an efficient nonlinear conversion is realized. Nevertheless, combining the preconditions for nonlinear frequency conversion, presented in the next chapter, with the insight gained by the Q-switching experiments in this chapter shows that a few setup modifications must be made.

In general, as Schneider et al. have shown, further improvements in setup engineering are possible, but a scaling factor of 2 or larger is relatively unlikely. Therefore, simultaneously increasing the saturation energy and the nonlinear threshold using LCFs is a reasonable step.



# 6 Nonlinear Frequency Conversion by a Q-Switched THTF-laser-pumped ZGP OPO

In this last experimental chapter, the findings of Chapter 5 are used to realize a suitable pump source for an efficient nonlinear frequency conversion using an OPO based on the nonlinear material ZGP. The work summarized in this chapter aims to push the average output power to the limits of a linear OPO cavity, which is inherently pump power restricted due to the damage threshold of the required isolator stage. The chapter starts with a short review of the nonlinear material ZGP (Section 6.1). Suitable phase-matching angles and the spectral pump acceptance bandwidth are calculated. The following Section 6.2 gives an overview on ZGP-based OPOs, which are pumped by 2  $\mu\text{m}$  fiber sources. Section 6.3 introduces the pump source and OPO setup, whereas the performance of the pump source is briefly presented in Section 6.4. Compared to Section 5.4, the pump source shows fewer fiber nonlinearities and a smaller emission bandwidth due to a shorter fiber length and a more narrowband VBG. Section 6.5 contains the actual OPO measurements with a new power record for 2  $\mu\text{m}$  fiber-laser-pumped ZGP OPOs.

## 6.1 Zinc Germanium Phosphide - ZGP

There are several materials for converting solid-state laser radiation from 1 to 2  $\mu\text{m}$  into the mid-wave infrared (MWIR). It can be distinguished between quasi-phase-matchable crystals like OP-GaAs and orientation-patterned gallium phosphide (OP-GaP) and birefringent crystals like cadmium silicon phosphide (CSP) and ZGP [24, 156].

There are even more materials, but those mentioned above exhibit relatively large nonlinear coefficients combined with a wide transparency range. Among these crystals, ZGP is probably the most investigated and the only one being commercially available with a sufficiently good quality. This makes ZGP a reasonable and adequate choice as a nonlinear crystal. Table 6.1 shows an overview of essential material data of ZGP. The crystal exhibits a chalcopyrite crystal lattice structure with a suitable birefringence for exploiting phase matching but not strong enough to induce a large beam walk-off [24]. For a pump wavelength of 2.1  $\mu\text{m}$  and assuming the pump wave is propagating at the crystal's cut angle of 54.5°, a walk-off angle of 11.6 mrad was calculated. ZGP has a reported damage threshold of 1–4 J/cm<sup>2</sup> [24], a thermal conductivity of 35 W/(K m) [157], and a relatively large nonlinear coefficient of 75 pm/V [158] leading to a strong parametric gain (compare to Eq. (2.41)). Therefore, ZGP has important properties as a nonlinear material and can enable an efficient conversion in a high-power regime.

The intention of using ZGP restricts the selection of possible pump sources. Due to a sharp defect-related absorption edge, the relevant transparency region is limited at  $\sim 2 \mu\text{m}$  towards the short-wavelength edge [24]. This excludes 1  $\mu\text{m}$  laser sources as pump sources and demands 2  $\mu\text{m}$  sources emitting at the far end of the wavelength band to avoid the absorption tail. An additional advantage of using a 2  $\mu\text{m}$  source is that the generated signal and idler waves can both lay in the MWIR. ZGP is transparent up to  $\sim 8.5 \mu\text{m}$ , where a strong multi-photon absorption feature starts to rise [24]. The absorption coefficients are plotted in Fig. 1.2 of the introduction. Before using ZGP as a nonlinear crystal, some critical preliminary considerations have to be made concerning the pump source and setup. The possible phase-matching angles inside the crystal and the spectral acceptance bandwidth are calculated, both being essential quantities for an efficient frequency conversion. Therefore, the ordinary and extraordinary refractive indices are determined out of the Sellmeier equation:

$$n^2 = A + \frac{B\lambda^2}{\lambda^2 - C} + \frac{D\lambda^2}{\lambda^2 - E}. \quad (6.1)$$

The necessary coefficients are taken from [159] and are depicted in Tab. 6.2. Figure 6.1 shows the resulting refractive indices. By definition, in positive uniaxial crystals, the ordinary wave experiences a smaller refractive index than the extraordinary wave. As already discussed in Section 2.2.3, there are only two possibilities for the phase matching of positive uniaxial crystals: Type I phase matching  $o \rightarrow ee$ , and type II phase matching  $o \rightarrow eo$ . Other combinations are not allowed due to the refractive index characteristics of ZGP. Equation (2.39) in combination with the Eqs. (2.44) and (2.35) are used to calculate the phase-matching conditions explicitly.

Table 6.1: Relevant material data for ZGP, which make it a good choice for an efficient and high-power MWIR radiation.

Material Data of ZnGeP <sub>2</sub> /ZGP	
crystal structure	II-IV-V <sub>2</sub> chalcopyrite lattice [24]
transparency range	2–8.5 $\mu\text{m}$ [24]
nonlinear coefficient	75 pm/V [158]
thermal conductivity	35 W/(K m) [157]
damage threshold	1–4 J/cm <sup>2</sup> [24]
walk-off angle( $\theta = 54.5^\circ$ , $\lambda = 2.1 \mu\text{m}$ )	11.6 mrad

Table 6.2: Sellmeier coefficients for determining the ordinary and extraordinary refractive indices of ZGP taken from [159].

Sellmeier Coefficients	A	B	C	D	E
ordinary axis	8.0409	1.68625	0.40824	1.2880	611.05
extraordinary axis	9.0929	1.8649	0.41468	0.84052	452.04

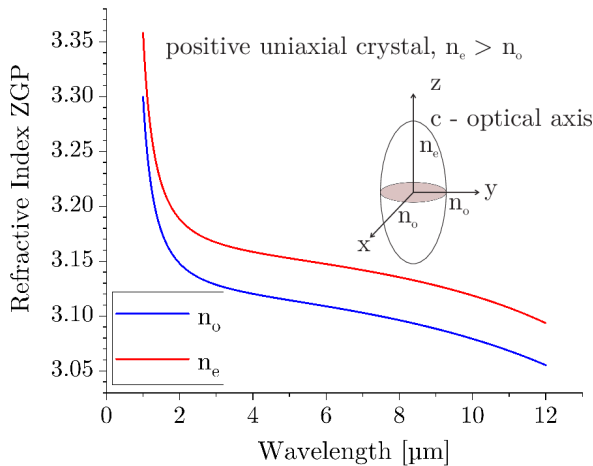


Figure 6.1: Ordinary and extraordinary refractive indices of the positive uniaxial crystal ZGP plotted versus wavelength.

The respective signal and idler pairs are determined for different phase-matching angles  $\theta$ . Figure 6.2 shows such a graph assuming a pump wavelength of 2.1  $\mu\text{m}$ . The graph displayed on the left-hand side shows the calculated type I and type II phase-matching possibilities.

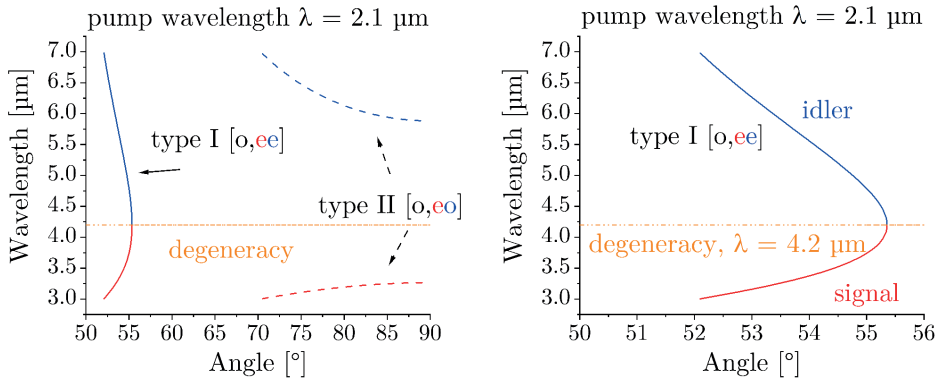


Figure 6.2: Phase-matching curves of matching signal and idler pairs as a function of the phase-matching angle  $\theta$ . The left-hand side shows an overview of possible type I and type II phase matching for a pump wavelength of  $2.1 \mu\text{m}$ . The right-hand side shows a close-up of the experimentally used type I phase matching.

For large angles up to  $90^\circ$ , which corresponds to the propagation along a principal axis (not the optical axis), type II phase matching is possible. Despite an advantageous walk-off free propagation along a principal axis at  $\theta = 90^\circ$ , the generated signal and idler only cover a tiny fraction of the MWIR spectrum. Therefore, type II phase matching can be omitted, and type I phase matching is the favored technique being realized for the OPO experiments. The right-hand side of Fig. 6.2 shows the type I phase matching as a close-up. With a pump radiation wavelength of  $2.1 \mu\text{m}$ , the phase-matching angle  $\theta$  is roughly between  $52$  to  $55.4^\circ$ .

A laser does not consist of a monochromatic plane wave as assumed for the phase-matching conditions but has a finite spectral emission bandwidth. Some estimates can be made to predict if a specific laser emission bandwidth will lead to an efficient conversion. This theoretical spectral acceptance bandwidth of the pump radiation is calculated as follows [73]:

Starting from a phase-matching angle  $\theta = 54.5^\circ$ , identical to the cut-angle of the used crystal, the matching signal and idler pair is determined. While keeping the idler wavelength and propagation angle constant, the phase mismatch and efficiency are calculated depending on the pump wavelength (Eqs. (2.39),(2.43)). The signal wavelength is adjusted according to the energy conservation (Eq. (2.35)). The determined values for a 1 cm long ZGP crystal are displayed in Fig. 6.3. By evaluating the FWHM of the  $\text{sinc}^2$ -function the spectral acceptance bandwidth of the pump wave is determined to 3.1 nm, being considered as an acceptable bandwidth for an efficient nonlinear process. For a 20 mm long crystal, like it has been used for the experiments, the maximum acceptable emission bandwidth for the Q-switched fiber laser decreases to 1.55 nm.

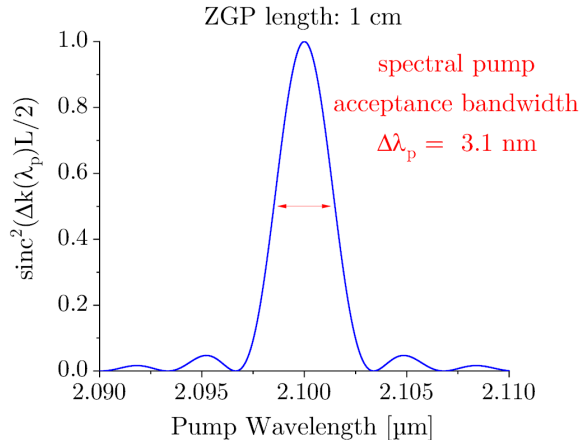


Figure 6.3: Conversion efficiency as a function of the pump wavelength to determine the spectral acceptance bandwidth for the pump radiation. For a 1 cm long ZGP crystal, a center emission wavelength of 2.1  $\mu\text{m}$ , and a propagation angle  $\theta = 54.5^\circ$ , the emission bandwidth of the pump laser must stay below 3.1 nm to achieve an efficient nonlinear frequency conversion.

## 6.2 Overview of 2 $\mu\text{m}$ -Fiber-Pumped ZGP OPOs

High peak powers are required to drive an efficient frequency conversion. Therefore, crystal lasers and, in particular,  $\text{Ho}^{3+}$ :YAG lasers are common pump sources for OPOs based on ZGP. These systems have already shown good efficiencies and high output powers [126, 160, 161]. However, power scaling of  $\text{Ho}^{3+}$ :YAG lasers while preserving a good beam quality tends to be challenging. With the improvements in 2  $\mu\text{m}$  pulsed fiber lasers, fiber lasers have become a possible and reasonable alternative to crystal lasers and earlier tandem OPO systems [162]. Fiber lasers deliver inherently smaller pulse energies than crystal lasers but promise the advantage of a more likely average power scaling with an excellent beam quality. Furthermore, fiber lasers offer the possibility of choosing out of a broad range of possible 2  $\mu\text{m}$  wavelengths to generate a specific set of idler and signal and operate at a wavelength being transparent for the nonlinear crystal.

A summary of relevant 2  $\mu\text{m}$  fiber laser pump sources used for nonlinear frequency conversion via ZGP OPOs is depicted in Tab. 6.4, the corresponding OPO results are displayed in Tab. 6.3. The data is listed according to their publication year. A few things stand out studying the literature overview. There is a tendency to increase the OPO pump wavelength from 2  $\mu\text{m}$  to  $> 2.1 \mu\text{m}$  to keep the pump absorption and thermal lens as small as possible.

Table 6.3: Overview of relevant 2  $\mu\text{m}$  fiber-laser-pumped OPOs.

Year Autor	OPO Setup	OPO Power W	OPO Pulse Energy $\mu\text{J}$	Conversion Efficiency %
2008 Creeden et al. [53]	linear OPO	> 0.64	> 21	22
2008 Creeden et al. [163]	linear OPO	2	> 20	16
2012 Simakov et al. [164]	linear OPO walk-off compensated	2.9	39	25
2014 Gebhardt et al. [165]	linear OPO	0.66	165	25
2015 Kieleck et al. [166]	linear OPO	6.5	163	32
2019 Daloz et al. [115]	linear OPO	8.1	81	24
2021 Schneider et al. [167]	linear OPO	3.9	230	39
2021 Holmen et al. [148]	V-shaped OPO	3.0	300	59
2023 Lorenz et al. [168]	linear OPO	8.1	162	44

This is a critical requirement for power scaling ZGP OPOs. In addition, there has been a change in pump source architecture over time. First, pulsed fiber laser sources were used for OPO pumping comprised of MOPA setups, which were amplifying gain- or Q-switched master oscillators by one or two amplifier stages [53, 163–165]. The systems were quite complex, and maximum conversion efficiencies of 26% with output powers of 2.9 W were achieved. Also, most sources were not realized linearly polarized, halving the total useful power for nonlinear frequency conversion. The following progress of pumping ZGP was driven by Q-switched single-oscillators. The advantage of these systems was a very compact setup with reduced complexity and the easy realization of a linearly polarized laser output. The single-oscillators showed excellent pulse peak powers up to 11 kW with improved conversion efficiencies of up to 39% and a boost in output power of up to 8.1 W, which is still the published power record of fiber-pumped ZGP OPOs [115, 166, 167]. So far, further power scaling of this system still needs to be proven.

Table 6.4: Overview of relevant 2  $\mu\text{m}$  fiber laser pump sources for nonlinear frequency conversion via ZGP OPOs. The corresponding OPO setups and results are summarized in Tab. 6.3.

Year Autor	Setup Specifications	Operation Wavelength	Pulse Peak Power <sup>+</sup>	Pulse Energy $\mu\text{J}$	Repetition Rate kHz	Pulse Duration <sup>*</sup> ns
2008 Creeden et al. [53]	Er <sup>3+</sup> gain-sw. TDF 1 TDF amplifier	1995	3.0	96	30	30
2008 Creeden et al. [163]	Er <sup>3+</sup> gain-sw. TDF 2 TDF amplifier	1995	4.0	127	100	30
2012 Simakov et al. [164]	Er <sup>3+</sup> gain-sw. TDF 1 TDF amplifier	2044	-	150	75	- <sup>†</sup>
2014 Gebhardt et al. [165]	Q-switched TDF 2 TDF amplifier	1980	89.0	663	4	7
2015 Kieleck et al. [166]	Q-switched TDF	2024	5.2	500	40	65
2019 Daloz et al. [115]	Q-switched THF	2090	3.6	340	100	90
2021 Schneider et al. [167]	Q-switched TDF	2050	11.1	590	17	50
2021 Holmen et al. [148]	diode seeded 3 HDF amplifier	2108	11	520	10	50
2023 Lorenz et al. [168]	diode seeded 3 HDF/TDF amplifier	2047	7.3	367	50	50

<sup>\*</sup> The blue marked pulse widths are assumed to be Gaussian-like pulses. The violet marked pulse widths are specially shaped square-like pulses.

<sup>†</sup> The pulse width is not mentioned. Therefore, no pulse peak power is calculated.

<sup>+</sup> For comparability, the peak powers of the Gaussian-like pulses are calculated by Eq. (5.2) since some publications are missing the Gaussian prefactor. The pulse peak power of Lorenz et al. is calculated by assuming a squared pulse.

Similar results in terms of pulse peak powers are also expected by up-to-date MOPA systems since fiber nonlinearities are prone to limit both technologies. However, Q-switched single-oscillators have one crucial disadvantage of a Q-switch inherent pulse shape. Therefore, some parts of the pulse do not exceed the nonlinear threshold, and a non-negligible amount of energy does not contribute to the nonlinear conversion process. Some pulse shapes are more, and some are less suitable for nonlinear conversion [169, 170]. A new trend is to reach back to MOPA systems, which are diode seeded. This offers the possibility of a free pulse shaping optimized for the nonlinear process and slightly better control of the spectral emission characteristics. Recently, conversion efficiencies of 59 % and output powers of 8.1 W were achieved [106, 168]. These systems show a performance competing with crystal lasers, but further power scaling still has to be realized.

In this thesis, the concept of Q-switched single-oscillators is pursued using a THF laser with the main interest in realizing a very compact and straightforward setup since the MOPA systems are very space-consuming and optimization complex.

## 6.3 Pump Source and OPO Setup

The experimental setup is divided into the pump source and the OPO. The pump source includes the Q-switched single-oscillator as depicted in Fig. 5.1, an isolator stage, and an attenuation stage. The pump source scheme is shown in Fig. 6.4. The Q-switched single-oscillator is based on the 18/270/297  $\mu\text{m}$  TCF. A VBG centered at 2.1  $\mu\text{m}$  as HR and a 3 % Fresnel reflection of an uncoated silica glass as OC form the cavity.

The laser is realized in a linearly polarized and a randomly polarized manner by inserting or removing an intra-cavity polarizer. By realizing both laser systems, the pump source shows a performance that can be theoretically used for quasi-phase-matchable and birefringent phase-matchable crystals. Generally, quasi-phase-matching does not require linearly polarized pump radiation but is shown to be advantageous [171]. Further reasons for comparing the polarized and unpolarized versions are explained later on. The randomly polarized laser output is directly measured after the OC at position A. In the case of the linearly polarized laser, the radiation is directed through an isolator stage to prevent any back reflections into the single-oscillator from the optics of the linear OPO cavity. The isolator stage introduces a loss of  $\sim 10\%$ . Switching to a ring cavity instead of a linear cavity would make the isolator stage redundant and would boost the performance of the linearly polarized pump source.



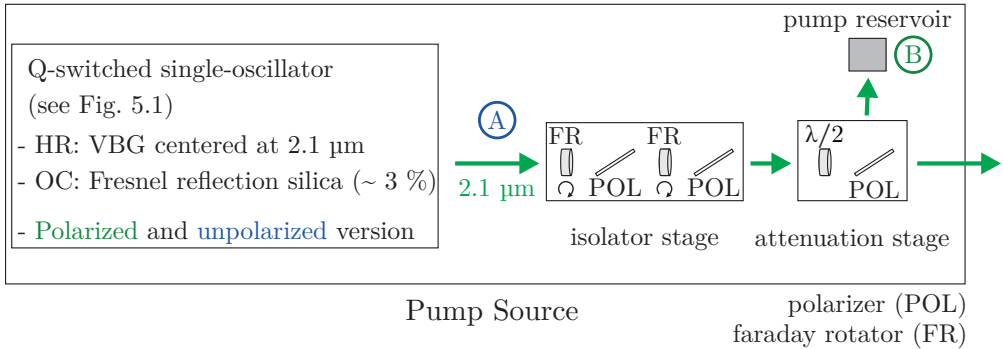


Figure 6.4: Scheme of the pump source used for pumping an OPO. The pump source is comprised of a Q-switched fiber single-oscillator, an isolator stage, and an attenuation stage. At position A, the radiation of a randomly polarized laser is measured, which could be used for pumping quasi-phase-matchable crystals. The laser output of a linearly polarized laser version is measured at position B.

In the last step, an attenuator is placed after the isolator stage to continuously adjust the pulse energy and average laser power, which can be sent on the OPO. The attenuator is comprised of a half-wave plate and a polarizer. The characteristics of the linearly polarized pump source are measured at position B, referred to as the pump reservoir. For these measurements, the attenuation stage is adjusted to reflect the laser radiation by the polarizer completely. For pumping the OPO, the half-wave plate is rotated to transmit the radiation through the polarizer and direct it to the OPO.

The scheme of the OPO setup is depicted in Fig. 6.5. The polarization emitted by the pump source is the p-polarization, which is equivalent to the extraordinary polarization related to the ZGP since the optical axis of the ZGP is placed parallel to the surface of the optical table. Another half-wave plate is used after the polarizer to adjust the polarization to match the ordinary polarization of the ZGP for type I phase matching. Then, a lens focuses the pump radiation into the nonlinear crystal. The linear OPO consists of an input coupler (IC), which is anti-reflection coated for the pump radiation and highly reflective for signal and idler from 3 to  $5 \mu\text{m}$ . The OC is partially reflective for signal and idler with a reflectivity of 50% and also anti-reflection coated for the pump radiation. The ZGP crystal is cut under an angle of  $54.5^\circ$  and has an aperture of  $6 \times 6 \text{ mm}$  with a length of 20 mm. Behind the OPO, a dichroic mirror separates the residual pump from the signal and idler.

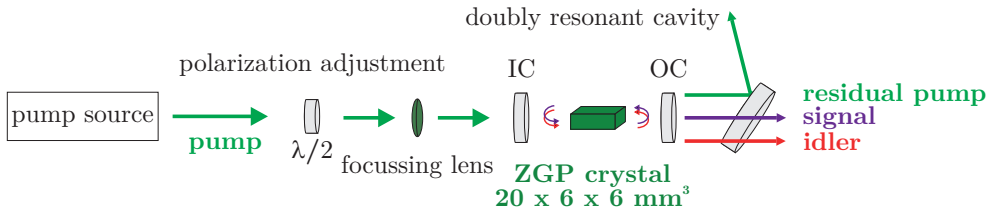


Figure 6.5: Scheme of the OPO used for nonlinear frequency conversion. A half-wave plate is used to adjust the polarization state of the pump radiation to match the ordinary polarization of the ZGP crystal, followed by a focusing lens. A linear cavity is utilized for a simple and compact setup design.

Boyd and Kleinmann have investigated the focussing conditions for an efficient OPG [172]. Comparing the suitable confocal parameters with the damage threshold of 1 to 2 J/cm<sup>2</sup> shows that focusing the pump radiation close to the damage threshold should lead to the most efficient conversion. Therefore, lenses with a focal length of 200 mm and 300 mm are used, leading to fluences of 1.8 J/cm<sup>2</sup> and 0.8 J/cm<sup>2</sup>, respectively.

In the next step, the resonator is typically designed to achieve the best mode matching between the pump and the generated signal and idler. Crucial to consider are thermal and gain lensing. Especially the thermal lensing can lead to a much smaller beam waist of the pump radiation in the ZGP crystal for a high average pump power. Therefore, focusing the pump radiation more loosely can be advantageous when operating the OPO with a larger pump power. For focused nanosecond OPOs, a plane-parallel cavity typically leads to a stable operation and good conversion efficiencies [173]. For the experiments, the mirrors are placed in the direct vicinity of the ZGP crystal leading to a cavity length of 22 mm.

When operating the OPO for higher average pump powers, it has been noticed that one set of OPO optics absorbs a certain amount of the pump radiation, leading to a non-negligible additional thermal lens. Therefore, the plane IC 1 is replaced by a plano-concave mirror with a radius of curvature of 100 mm, which is made from an IR material (IC 2). There is no according optic to replace the OC.

## 6.4 Pump Source Performance

This section briefly introduces the pulsed laser source, which has finally been used as a pump source for nonlinear frequency conversion. Using a birefringent crystal and a linear OPO cavity introduces several deteriorations to the originally unpolarized laser version due to the need to realize a linearly polarized laser version and the usage of an additional isolator stage.

For all graphs, which are displayed within this section, the green curves are related to the actual pump radiation directly sent on the OPO (measurement position B in Fig. 6.4). The blue curves show the same characteristics for the identical laser but for an unpolarized laser setup, directly measured after the OC (measurement position A in Fig. 6.4).

One of the outcomes of Chapter 5 is the finding that optimizing the relevant optical characteristics for an efficient nonlinear frequency conversion can not be considered detached from scaling the average laser output power. This means that the typical fiber lengths used for efficient power scaling in CW operation lead to a critical interaction length for the signal radiation with the active fiber. The resulting nonlinearities deteriorate the spectral and temporal characteristics necessary for an efficient nonlinear process. As a result of the spectral broadening, the pulse energy decreases since a non-negligible amount of power is no longer reflected by the VBG, and also a significant amount of energy is no longer within the spectral acceptance bandwidth. Therefore, in the first step, the CW power scaling of the shortened laser source is investigated. This shows how power scaling is hindered when shortening the fiber. The left-hand side of Fig. 6.6 displays the laser output power versus the incident pump power. As shown in Section 4.2.4, slope efficiencies close to 50 % can be reached for a sufficient fiber length. However, for the relatively short fiber used in this chapter, the efficiency related to the incident pump power decreases, as expected, to 40 %. An output power of 59 W is reached for an incident pump power of 167 W. The slope efficiency of the fully assembled pump source is determined to 34.5 %, leading to a reduced output power of 51 W.

Firstly, the optimized laser source for nonlinear conversion shows a significant drop in performance compared to the systems optimized for power scaling with a slope efficiency difference of about 10 %. Even more, the power, which can be sent on the OPO, is reduced even further when realizing the linearly polarized laser. This means that the power scaling in Q-switched operation compared to CW operation is much more difficult due to a large discrepancy in slope efficiency. In addition, the risk of damaging the diode laser is highly increased when using a shorter fiber due to more unabsorbed pump radiation, which is back-coupled into the other diode in the symmetric pump configuration.

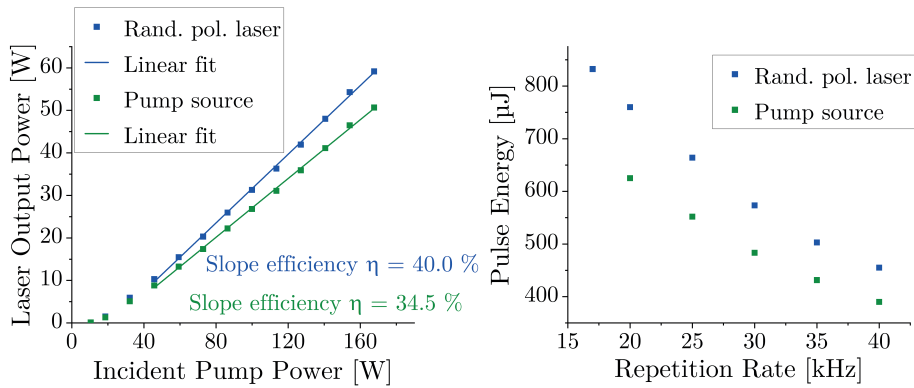


Figure 6.6: Comparison of the laser output characteristics of a randomly polarized laser setup and the actual radiation left over for nonlinear conversion. Left: Power scaling in CW operation. Right: Pulse energies for a diode pump power of 73 W in Q-switched operation.

The right-hand side of Fig. 6.6 shows both systems' representative maximum reachable pulse energies. The comparison is performed for an incident pump power of 73 W. Of course, the same pulse energies and the associated emission spectra, pulse shapes, and pulse widths can be recreated at higher average output powers and repetition rates, which are linked by Eq. (2.27). For nonlinear frequency conversion, the laser is typically operated at the highest pulse peak power for a specific incident pump power to obtain the best conversion efficiency. The pure unpolarized laser source reached pulse energies up to 820  $\mu\text{J}$  with pulse durations of 37 ns, the assembled pump source delivers 625  $\mu\text{J}$  with slightly smaller pulse durations of 36 ns. The pulses suffer from an energy loss of 195  $\mu\text{J}$ . For the randomly polarized laser, the RR could be lowered down to 17 kHz, whereas for the polarized laser version, the RR only reaches 20 kHz. The pulses are nicely Gaussian-like, indicating substantially smaller fiber nonlinearities than the heavily modulated pulse in Fig. 5.8. The pulses are depicted on the left-hand side of Fig. 6.7. The polarized laser shows the same pulse width for a higher repetition rate resulting from the fact that one polarization experienced all the gain.

This fact is also reflected in the measured emission spectra. The output spectra of both systems are compared on the right-hand side of Fig. 6.7. The pure randomly polarized laser shows an almost symmetrical nonlinear spectral broadening with a FWHM of 370 pm and a 20 dB-width of 2750 pm. Since the laser radiation is linearly polarized in the final pump source, the fiber nonlinearities are more pronounced. In this case, a FWHM of 470 pm and a 20 dB-width of 3480 pm are determined.

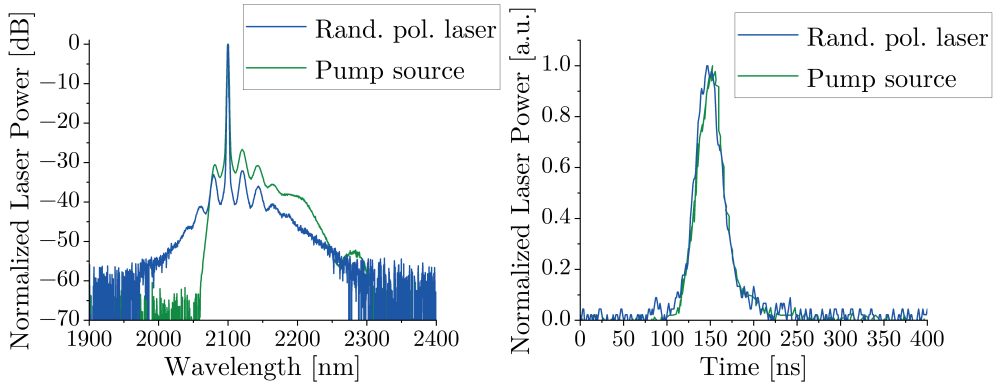


Figure 6.7: Comparison of the temporal and spectral output characteristics of a randomly polarized laser setup and the linearly polarized laser setup used for nonlinear conversion.

80 % of the signal is within the calculated spectral acceptance bandwidth of 1.55 nm. In comparison, the Q-switched laser realized in Section 5.4 emitted less than 50 % of the signal power within the spectral acceptance bandwidth. Again, the spectrum of the pump source shows a strong cut for shorter wavelengths because of the transmission characteristics of the thin film polarizers.

All in all, the gained knowledge from the Q-switching experiments and the restrictions for an efficient nonlinear frequency conversion have led to the realization of a very suitable pump source with a nice Gaussian-like 36 ns-broad pulse shape and a pulse peak power above 16 kW. Comparing the realized pump source with the presented pump sources in Tab. 6.3 shows that an excellent pump source is obtained in terms of pulse energy, pulse peak power, and emission wavelength.

## 6.5 OPO Results

Initial OPO experiments are performed with the focussing lens having a focal length of 200 mm. Figure 6.8 shows the measured OPO power as a function of the incident pump radiation. Pump power values of  $\sim 12.2$  W and  $\sim 28.8$  W are used to pump the OPO for the high fluence value of  $1.8$  J/cm<sup>2</sup>. Besides the power difference, the other optical characteristics of the pump radiation stay the same.

Using IC 1 average mid-IR output powers of 4.8 W and 10.3 W are generated with conversion efficiencies of 39.7% and 35.9%, respectively. IC 2 is only installed for a pump power of  $\sim 12.2$  W since it shows a power and fluence-dependent damage threshold, which is almost reached in this setup configuration. For IC 2, a conversion efficiency of 47.8% is reached, resulting in an average OPO output power of 5.9 W.

By changing the input coupler from IC 1 to IC 2, a significant improvement in terms of conversion efficiency by 20% is achieved. To ensure that the performance boost is not due to a better mode matching achieved by the curved mirror, the input coupler is changed to a 100 mm concave mirror from the IC 1 series. No improvements are noticed. Therefore, it is presumed that the performance boost is material related. The non-negligible absorption of the pump radiation in IC 1 can lead to a serious thermal lensing effect, which probably deteriorates the OPO performance. This theory is supported by the decrease in conversion efficiency when increasing the incident pump power. A higher incidental average pump power consequently leads to stronger thermal lensing. Further power scaling is stopped at a pump power of  $\sim 28.8$  W to avoid surpassing the damage threshold of ZGP by even stronger thermal lensing.

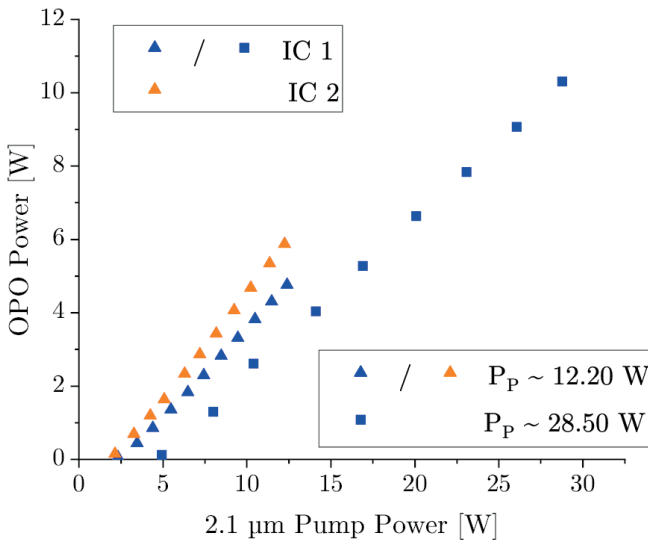


Figure 6.8: Average OPO power as a function of the incident pump power for a focal length of 200 mm. Different average pump powers and ICs are measured.

To ease the thermal lensing effect and allow for further power scaling, a focusing lens with a larger focal distance of 300 mm is installed. The average pump power is again stepwise increased. The incident pump powers are  $\sim 12.2$  W,  $\sim 28.3$  W, and 36.1 W, which corresponds to 40 W entering the isolator stage. Higher power values exceed the damage threshold of the Faraday rotators. The corresponding OPO results are summarized in Fig. 6.9. Using IC 1, mid-IR output powers of 4.5 W, 10.3 W, and 11.7 W are generated with conversion efficiencies of 37.5 %, 36.2 %, and 32.5 %, respectively. Due to the decreased fluence of the pump radiation, further power scaling is also achieved for IC 2. Mid-IR output powers of 5.2 W and 12.2 W with conversion efficiencies of 42.5 % and 43.3 % are achieved for the lower pump powers, respectively. However, IC 2 has been damaged when approaching an average output power of 36.1 W.

IC 1 features a continuous decrease in conversion efficiency with an increase in average pump power, which is again connected to the thermal lens effect. The effect is not visible for the OPO performances of IC 2 due to a lower pump absorption. In addition, the conversion efficiency drops when changing from a focal length of 200 mm to 300 mm. This can be attributed to a smaller parametric gain according to the optimum focussing condition [172].

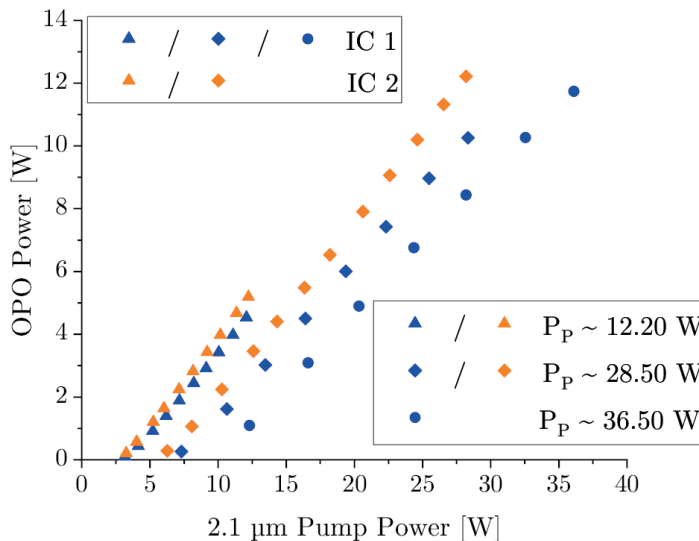


Figure 6.9: Average OPO power as a function of the incident pump power for a focal length of 300 mm. Different average pump powers and ICs are measured.

However, when increasing the pump power, the thermal effect is more prone to deteriorate the OPO performance for a tighter focus. Consequently, it can be advantageous to relax the focus for power scaling. Table 6.5 summarizes the OPO results and displays the average output power, the conversion efficiency, the maximum pulse energy, and the slope efficiency.

To determine the temporal stability of the OPO, the laser output power is measured for the configuration delivering the largest MWIR output power (IC 2,  $P_p=28.2$  W, and  $f=300$  mm). The measurement is depicted in Fig. 6.10. The output power is 12.2 W with a standard deviation of 0.029 W, which corresponds to a percentage standard deviation of 0.24 %. This shows that the output is very stable.

As a further substantial quantity next to the conversion efficiency and the temporal stability, the beam quality factor  $M^2$  is measured. A dichroic mirror separates the signal and idler to perform this measurement. The signal and idler waist of the  $M^2$ -measurement for the same operation point as for the stability measurement is depicted in Fig. 6.11.

The left-hand side shows the signal, and the right-hand side shows the idler measurement. The signal/idler has an  $M^2$  of 3.5/4.0 and 3.9/4.3 in x- and y-direction, respectively. The  $M^2$  seems relatively high. The literature mentioned in Tab. 6.3 shows  $M^2$  values around two but are measured at lower average output powers. Measuring the beam quality with the same setup but with the lower average pump power of  $\sim 12$  W and an OPO power of 5.2 W also leads to an  $M^2$  of  $\sim 2$ .

The reason for a general deterioration of the  $M^2$  can be diverse. First, a relatively strong focus of the pump radiation due to the inherent low pulse energies of the fiber laser can lead to thermal lensing in the nonlinear crystal when power scaling the OPO setup, which cannot be ruled out.

Table 6.5: Comparison of OPO results for different average pump powers, focus conditions, and ICs.

EFL	200 mm			300 mm				
Input Coupler	IC 1		IC 2	IC 1			IC 2	
Average Input Power [W]	12.2	28.8	12.4	12.1	28.30	36.1	12.2	28.20
mid-IR output power [W]	4.8	10.3	5.9	4.5	10.3	11.7	5.2	12.2
conversion efficiency [%]	39.7	35.9	47.8	37.5	36.4	32.5	42.5	43.3
pulse energy [ $\mu$ J]	240	229	295	225	229	195	260	271
slope efficiency [%]	48.7	42.6	57.4	50.5	48.4	44.8	56.0	55.1



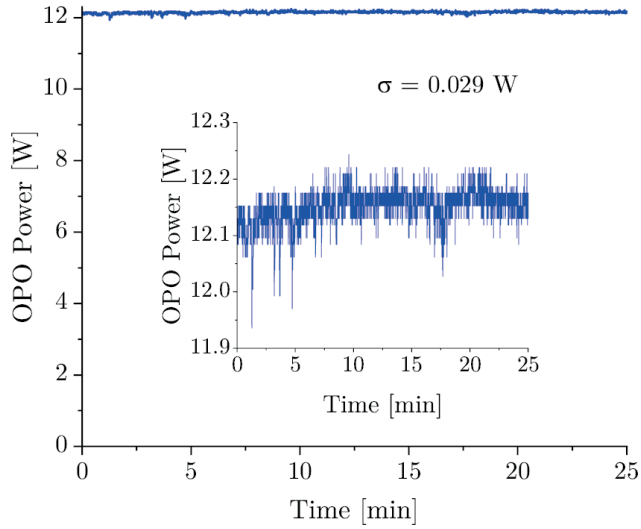


Figure 6.10: Long term measurement of the average OPO power for a duration of 25 min at the highest output power achieved.

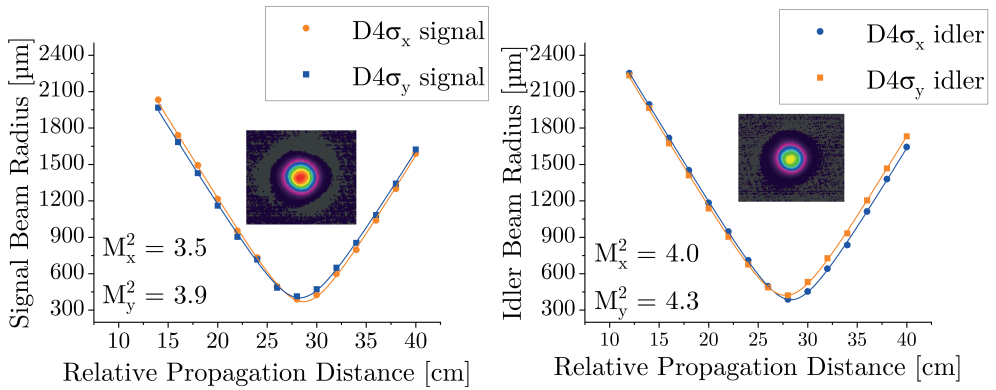


Figure 6.11: Beam quality measurement of signal and idler for an average OPO power of 12.2 W. Left: Signal measurement with an  $M_{x/y}^2$  of 3.5/3.9. Right: Idler measurement with an  $M_{x/y}^2$  of 4.0/4.3.

The experiments also show a strong absorption and thermal lens within the utilized optics. This absorption is mainly removed in the IC 2 using another material, but this is impossible for the OC. Therefore, a strongly absorbing cavity element could not be removed, certainly impacting the beam quality. The deterioration increases with increasing average power. Secondly, the dichroic mirror does not perfectly decouple signal and idler wavelengths since the cut-on and cut-off wavelengths do not perfectly match the spectral characteristics of the OPO emission wavelengths. Repeating the measurements with improved optics is recommended to make a more meaningful statement.

The last measurement investigates the pulse shapes for the pump, the residual pump, and signal/idler radiation. The left-hand side of Fig. 6.12 shows the initial pump pulse, the residual pump pulse, and the signal/idler pulse for an average OPO power of 5.2 W (setup configuration: IC 2,  $P_p=12.2$  W, and  $f=300$  mm). The pulses are scaled according to their pulse energies. A 36 ns pump pulse results in a 30 ns OPO pulse.

The residual pump pulse misses the highest instantaneous power values (central peak), compared to the initial pump pulse. A significant amount of this energy is converted into mid-IR. There is a small peak at the leading edge since an efficient pump depletion will only occur when a certain amount of signal and idler has already been built up [169]. The nonlinear threshold is already reached before. However, the residual pump pulse also features another peak. This peak can be related to a small back conversion [169], which already takes place and slightly decreases the conversion efficiency. To avoid such a back-conversion, smaller peak intensities must be used by either increasing the waist diameter of the pump, increasing the signal/idler outcoupling at the OC, or adjusting the OC reflectivity of the pump laser itself to adjust the pulse width.

Different residual pump pulses are depicted on the right-hand side of Fig. 6.12, related to different input pump energies. The pulses are again scaled according to their energy. The black curve belongs to the smallest input energy. The pump depletion starts very close to the middle of the pulse. The onset of pump depletion shifts to the leading edge of the pulse when the pulse energies are increased. The red curve shows a small plateau after the leading peak, whereas back conversion starts for the blue and green curves indicated by a second peak. The effect does not seem strong since there is no kink in the power scaling curves depicted in Fig. 6.8 and 6.9.

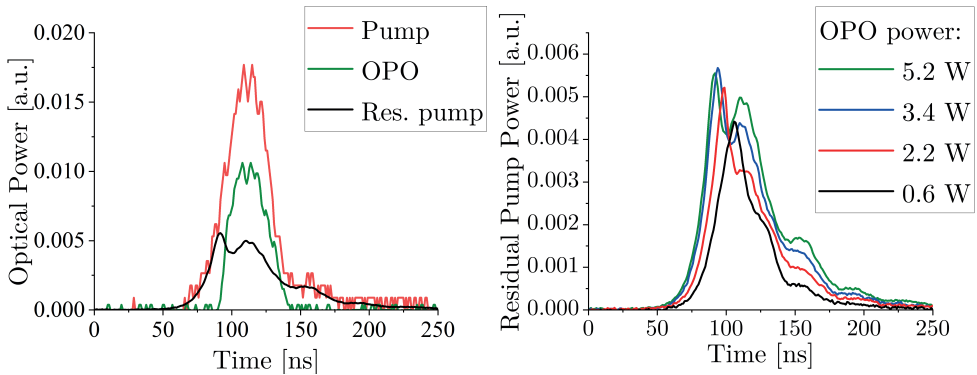


Figure 6.12: Comparison of different pulses involved in the nonlinear conversion process. Left: Initial pump, residual pump, and OPO pulse. Right: Residual pump pulses for different OPO output powers while increasing the average power and pulse energy incident on the OPO.

## 6.6 Summary and Conclusion

A powerful OPO has been built using a well-optimized Q-switched THF laser pump source. Using a simple linear cavity with a plane-plane resonator, an average power of signal and idler up to 11.7 W is generated with pulse energies up to 270  $\mu\text{J}$  when using IC 1. The measurements are only pump power limited since the maximum average power for the required isolator stage is reached. The pump source itself can deliver more power. Therefore, changing the OPO geometry from a linear cavity to a ring cavity will open the path for further power scaling.

An important aspect is the choice of suitable OPO optics. Some optics show strong absorption features and limit the power scaling by dramatically decreasing the conversion efficiency, most likely due to strong thermal lensing. Changing some of the optics (IC 1  $\rightarrow$  IC 2) leads to a conversion efficiency of 43.3% and output powers of up to 12.2 W, which results in a new record in terms of MWIR power generated from a fiber-laser-pumped ZGP OPO by an increase of 50% compared to former results [115, 168]. Even conversion efficiencies approaching 50% are demonstrated in a lower power regime. Already a conversion efficiency of 43.3% is a new efficiency record for Q-switched fiber-laser-pumped ZGP OPOs. The only OPOs that show a better conversion efficiency are those pumped by diode-seeded MOPA systems, which have superior pulse shaping capabilities [106, 168]. The investigation of the signal/idler pulse shape shows a small back conversion. Overall, the pump source is well optimized, and further investigations must focus on optimizing optics and the OPO design itself.

One drawback is a relatively large beam quality factor of  $\sim 4$ . A cavity redesign can eventually improve the beam quality factor, but in the first step, a possible influence of insufficient optics must be investigated.

# 7 Conclusion and Outlook

## 7.1 Conclusion

The aim of this thesis is the performance investigation of state-of-the-art THFs for laser operating wavelengths  $\geq 2.09 \mu\text{m}$ . The focus is put on power scaling in CW operation and average-power and pulse-energy scaling in nanosecond pulsed operation. Based on experimental results, it turns out that THFs are not only excellently suited for laser operation at  $2.09 \mu\text{m}$  but are predestined for lasing up to wavelengths of  $2.2 \mu\text{m}$ . The performance of the realized fiber lasers surpasses former estimations by far. The efficiencies reached in the experiments are close to the ones from HDF lasers, with the advantage of a much more compact setup and reduced complexity. Taking into account the tandem pumping of HDF lasers ( $79\text{X nm} \rightarrow \text{TDF} \rightarrow \text{HDF}$ ), the developed THF lasers ( $79\text{X nm} \rightarrow \text{THF}$ ) show a much better overall efficiency. Therefore, THF lasers are a serious alternative to current purely HDF lasers.

In the beginning, various tunable laser setups are realized to locate a possible operation regime. The experimental results show that wavelengths up to  $2.2 \mu\text{m}$  can be efficiently covered, which are typically dedicated to HDF lasers [27, 28]. Even laser emission at  $2.24 \mu\text{m}$  is achieved for the first time.

To realize such a broad tunability, a successful analysis and an ongoing improvement of the free-space laser setup have been required. Especially, the longer emission wavelengths of THF lasers compared to TDF lasers have created problems regarding chromatic aberrations and increased absorption. Critical elements, which have been investigated and optimized, are fiber end caps, the material of optics, and the coupling of signal and pump radiation with the active fiber. However, based on an optimized laser setup, long wavelength operation and stable power scaling are achieved.

In a CW regime and at an emission wavelength of 2.1  $\mu\text{m}$ , laser output powers of 260 W are realized with a slope efficiency of  $\sim 50\%$ . At the edge of laser emission for silica-based fibers at 2.2  $\mu\text{m}$ , laser output powers of up to 145 W are shown with a slope efficiency close to 30%. These pump-power-limited laser performances show that successful power scaling is achieved, comparable to or even better than for HDF lasers (see Section 4.2.1). At 2.2  $\mu\text{m}$ , a new power record is set with a scaling factor of 15 compared to the prior power value [106].

Regarding the results mentioned above, the setup exhibits the characteristics of a fiber bench as it is implemented in a free-space configuration. For products designed for practical applications, it is essential to develop a more robust and space-efficient system. This integration step is already partially introduced with an all-fiber laser setup comprised of FBGs at an emission wavelength of 2.12  $\mu\text{m}$  and a maximum output power of 145 W. The slope efficiency of 47% shows that the implementation is well accomplished with a strong potential for further power scaling. Therefore, new power records in the wavelength regime of 2.1 to 2.2  $\mu\text{m}$  with output powers exceeding current 400 W [30] are expected.

Initially, the THF has been intended to be used as a pump source for nonlinear frequency conversion. To act as a pump source, the fiber laser is Q-switched to realize a nanosecond pulsed laser. Like for the CW regime, the THF laser is operated over a wavelength range from 2.1 to 2.2  $\mu\text{m}$ . Based on these experiments, the impact of different laser parameters is investigated. One primary finding is that the determined fiber lengths for an efficient power scaling in CW operation show strong detrimental fiber nonlinearities in pulsed operation. These fiber nonlinearities, mainly created by an improved pulse peak power in a pulsed regime, combined with a filtering effect of the HR, ultimately limit the pulse energy and decrease the average output power in Q-switched laser systems. Depending on the intended application of the pulsed laser source, this must definitely be taken into account when designing such a laser source.

The experimentally generated pulse energies range from 800  $\mu\text{J}$  at an emission wavelength of 2.1  $\mu\text{m}$  down to 300  $\mu\text{J}$  at 2.2  $\mu\text{m}$ , which shows that good performance, even at this edge wavelength, is possible. However, at 2.2  $\mu\text{m}$ , the high reflectance of the installed OC has some detrimental effects, leading to relatively long pulse durations and, therefore, low pulse peak powers. To the best of the author's knowledge, the realized Q-switched silica fiber lasers are the first ones operating at  $\geq 2.1$   $\mu\text{m}$  overlapping with application-related atmospheric transmission windows.

For nonlinear frequency conversion, the Q-switched fiber laser is optimized to keep as much energy as possible within the spectral acceptance bandwidth for an efficient nonlinear process. With pulse peak powers of 16 kW at 2.1  $\mu\text{m}$  and an average output power of  $\sim 40$  W, a Q-switched fiber laser source is created, which is more than suitable for nonlinear frequency conversion, when comparing with other pump sources (see Section 5.1). This is confirmed by the accomplished OPO results. By using a linear OPO cavity and ZGP as a nonlinear crystal, a mid-IR power of 12.2 W is generated with a conversion efficiency of 43.3%. The mid-IR power out of a fiber-laser-pumped ZGP OPO is increased by 50% [115, 168], and the conversion efficiencies are only inferior to diode-seeded MOPA systems with the capability of pump pulse shaping (see Section 6.2). The mid-IR output power of the nonlinear frequency conversion is only limited by the damage threshold of the isolator stage, restricting the supplied pump power.

To sum up, using a THF turns out to be an elegant way of generating laser radiation in CW and Q-switched operation up to wavelengths of 2.2  $\mu\text{m}$ . So far, the fibers are mainly used in free-space single-oscillator configurations, but the lasers created show more than promising results within this configuration. This can have a lasting effect on strategies for power scaling of 2  $\mu\text{m}$  laser radiation, especially in the longer wavelength region.

## 7.2 Outlook

In perspective, future work will focus on both power scaling and the further integration of the laser setup. So far, the realized laser sources are only pump power limited. A logical step will be the replacement of the installed 300 W diodes with more powerful diodes as an intuitive way of increasing the laser output power further.

Another important step towards power scaling will be the transition from single-oscillators to MOPA systems [5]. This can be accomplished based on the example of Romano et al. [16]. The implementation of a MOPA system is also a path to a more integrated and rugged laser system, which is more desirable within a commercial product. Such an all-fiber system can also be realized for single-oscillators [100], where the first steps are already done within this thesis for a low-power level. The aforementioned setup integration has the need for high-performance fiber components [174, 175]. Most likely, off-the-shelf solutions are unavailable due to the requirements, complexity, and unique kinds of fibers used. Therefore, a major and necessary task will be the realization of tailored in-house fiber components.

In terms of nonlinear frequency conversion, further progress is not hindered by the developed Q-switched pump source but by the OPO cavity itself. The limits of the linear OPO cavity are reached, and a setup redesign is required. Using a ring cavity will make the isolator stage redundant [77]. Besides the possibility of further power scaling, this will boost the supplied pump pulse energy by saving about 10 % losses from the omitted isolator stage.



# Bibliography

- [1] T. H. Maiman, “Stimulated Optical Radiation in Ruby,” *Nature*, vol. 187, pp. 493–494, 1960.
- [2] A. Tünnermann, T. Schreiber, and J. Limpert, “Fiber lasers and amplifiers: an ultrafast performance evolution,” *Appl. Opt.*, vol. 49, no. 25, F71–F78, Sep. 2010.
- [3] J. Limpert *et al.*, “The Rising Power of Fiber Lasers and Amplifiers,” *IEEE Journal of Selected Topics in Quantum Electronics*, vol. 13, no. 3, pp. 537–545, 2007.
- [4] D. J. Richardson, J. Nilsson, and W. A. Clarkson, “High power fiber lasers: current status and future perspectives,” *J. Opt. Soc. Am. B*, vol. 27, no. 11, B63–B92, Nov. 2010.
- [5] A. Braglia, A. Califano, Y. Liu, and G. Perrone, “Architectures and components for high power CW fiber lasers,” *International Journal of Modern Physics B*, vol. 28, no. 12, p. 1 442 001, 2014.
- [6] L. Dong and B. Samson, *Fiber lasers: basics, technology, and applications*. CRC press, 2016.
- [7] M. J. Digonnet, *Rare-earth-doped fiber lasers and amplifiers, revised and expanded*. CRC press, 2001.
- [8] M. N. Zervas, “High power ytterbium-doped fiber lasers - fundamentals and applications,” *International Journal of Modern Physics B*, vol. 28, no. 12, p. 1 442 009, 2014.
- [9] B. Shiner, “Fiber lasers for material processing,” in *Critical Review: Industrial Lasers and Applications*, vol. 5706, SPIE, 2005, pp. 60–68.
- [10] P. M. Becker, A. A. Olsson, and J. R. Simpson, *Erbium-doped fiber amplifiers: fundamentals and technology*. Elsevier, 1999.

- [11] J. Townsend, W. Barnes, and S. Crubb, “Yb<sup>3+</sup> sensitised Er<sup>3+</sup> doped silica optical fibre with ultra high transfer efficiency and gain,” *MRS Online Proceedings Library (OPL)*, vol. 244, p. 143, 1991.
- [12] J. Geng and S. Jiang, “Fiber lasers: the 2 μm market heats up,” *Optics and Photonics News*, vol. 25, no. 7, pp. 34–41, 2014.
- [13] A. Sincore, J. D. Bradford, J. Cook, L. Shah, and M. C. Richardson, “High Average Power Thulium-Doped Silica Fiber Lasers: Review of Systems and Concepts,” *IEEE Journal of Selected Topics in Quantum Electronics*, vol. 24, no. 3, pp. 1–8, 2018.
- [14] T. Ehrenreich, R. Leveille, I. Majid, K. Tankala, G. Rines, and P. Moulton, “1-kW, All-Glass Tm: fiber Laser,” in *Fiber Lasers VII: Technology, Systems, and Applications*, vol. 7580, SPIE, 2010.
- [15] B. M. Anderson, J. Solomon, and A. Flores, “1.1 kW, beam-combinable thulium doped all-fiber amplifier,” in *Fiber Lasers XVIII: Technology and Systems*, vol. 11665, SPIE, 2021, 116650B.
- [16] C. Romano, D. Panitzek, D. Lorenz, P. Forster, M. Eichhorn, and C. Kieleck, “937 W Thulium:silica fiber MOPA operating at 2036 nm,” in *European Physical Journal Web of Conferences*, vol. 267, 2022, p. 02016.
- [17] K. Scholle, S. Lamrini, P. Koopmann, and P. Fuhrberg, “2 μm Laser Sources and Their Possible Applications,” in *Frontiers in Guided Wave Optics and Optoelectronics*, IntechOpen, 2010, ch. 21.
- [18] P. Fuhrberg, A. Ahrens, A. Schkutow, and T. Frick, “2 μm laser transmission welding: welding of transparent and opaque polymers with single-mode tm-doped fiber lasers,” *PhotonicsViews*, vol. 17, no. 2, pp. 64–68, 2020.
- [19] A. Daniels, *Field Guide to Infrared Optics, Materials, and Radiometry*. SPIE, 2018.
- [20] Z. Mierczyk, “Eye-safe laser systems,” in *Laser Technology VI: Progress in Lasers*, vol. 4237, SPIE, 2000, pp. 177–188.
- [21] P. A. Budni, L. A. Pomeranz, M. L. Lemons, C. A. Miller, J. R. Mosto, and E. P. Chicklis, “Efficient mid-infrared laser using 1.9 μm-pumped Ho:YAG and ZnGeP<sub>2</sub> optical parametric oscillators,” *J. Opt. Soc. Am. B*, vol. 17, no. 5, pp. 723–728, May 2000.

- 
- [22] D. Faye, E. Lallier, A. Grisard, B. Gérard, C. Kieleck, and A. Hirth, “High efficiency mid-infrared OPO based on low-loss orientation-patterned GaAs samples (OP-GaAs),” in *Nonlinear Frequency Generation and Conversion: Materials, Devices, and Applications VII*, vol. 6875, SPIE, 2008, 68750G.
- [23] J. Mikołajczyk *et al.*, “Analysis of free-space optics development,” *Metrology and Measurement Systems*, vol. 24, no. 4, pp. 653–674, 2017.
- [24] P. G. Schunemann, K. T. Zawilski, L. A. Pomeranz, D. J. Creeden, and P. A. Budni, “Advances in nonlinear optical crystals for mid-infrared coherent sources,” *J. Opt. Soc. Am. B*, vol. 33, no. 11, pp. D36–D43, Nov. 2016.
- [25] C. Romano, “Design of Optimized Thulium-doped Fiber Amplifiers through Experiment and Performance Simulation,” Ph.D. thesis, Télécom ParisTech, Dec. 2018.
- [26] P. F. Moulton *et al.*, “Tm-Doped Fiber Lasers: Fundamentals and Power Scaling,” *IEEE Journal of Selected Topics in Quantum Electronics*, vol. 15, no. 1, pp. 85–92, 2009.
- [27] A. Hemming, N. Simakov, J. Haub, and A. Carter, “A review of recent progress in holmium-doped silica fibre sources,” *Optical Fiber Technology*, vol. 20, no. 6, pp. 621–630, 2014.
- [28] J. L. Gouët, F. Gustave, P. Bourdon, T. Robin, A. Laurent, and B. Cadier, “Realization and simulation of high-power holmium doped fiber lasers for long-range transmission,” *Opt. Express*, vol. 28, no. 15, pp. 22 307–22 320, Jul. 2020.
- [29] B. Beaumont, P. Bourdon, A. Barnini, L. Kervella, T. Robin, and J. Le Gouët, “High Efficiency Holmium-Doped Triple-Clad Fiber Laser at 2120 nm,” *Journal of Lightwave Technology*, vol. 40, no. 19, pp. 6480–6485, 2022.
- [30] A. Hemming *et al.*, “A monolithic cladding pumped holmium-doped fibre laser,” in *CLEO: 2013*, Optica Publishing Group, 2013, CW1M.1.
- [31] A. S. Kurkov, E. M. Sholokhov, A. V. Marakulin, and L. A. Minashina, “Effect of active-ion concentration on holmium fibre laser efficiency,” *Quantum Electronics*, vol. 40, no. 5, p. 386, Aug. 2010.
- [32] J. Wang, N. Bae, S. B. Lee, and K. Lee, “Effects of ion clustering and excited state absorption on the performance of Ho-doped fiber lasers,” *Opt. Express*, vol. 27, no. 10, pp. 14 283–14 297, May 2019.
- [33] C. Ghisler, W. Lüthy, and H. Weber, “Cladding-pumping of a  $\text{Tm}^{3+}:\text{Ho}^{3+}$  silica fibre laser,” *Optics Communications*, vol. 132, no. 5, pp. 474–478, 1996.
-

- [34] S. Jackson, "The effects of energy transfer upconversion on the performance of  $\text{Tm}^{3+}$ ,  $\text{Ho}^{3+}$ -doped silica fiber lasers," *IEEE Photonics Technology Letters*, vol. 18, no. 17, pp. 1885–1887, 2006.
- [35] N. J. Ramírez-Martínez, M. Núñez-Velázquez, and J. K. Sahu, "Study on the dopant concentration ratio in thulium-holmium doped silica fibers for lasing at  $2.1 \mu\text{m}$ ," *Opt. Express*, vol. 28, no. 17, pp. 24 961–24 967, Aug. 2020.
- [36] J. A. Buck, *Fundamentals of optical fibers*. John Wiley & Sons, 2004, vol. 50.
- [37] J. Broeng, T. Søndergaard, S. E. Barkou, P. M. Barbeito, and A. Bjarklev, "Waveguidance by the photonic bandgap effect in optical fibres," *Journal of Optics A: Pure and Applied Optics*, vol. 1, no. 4, p. 477, Jul. 1999.
- [38] E. Hecht, *Optik*. de Gruyter, 2018.
- [39] J. Hecht, *Understanding fiber optics*. Laser Light Press, 2015.
- [40] A. Yariv, *Quantum electronics*. John Wiley & Sons, 1989.
- [41] E. Snitzer, "Cylindrical Dielectric Waveguide Modes," *J. Opt. Soc. Am.*, vol. 51, no. 5, pp. 491–498, May 1961.
- [42] P.-A. Belanger, "Beam quality factor of the LP<sub>01</sub> mode of the step-index fiber," *Optical Engineering*, vol. 32, no. 9, pp. 2107–2109, 1993.
- [43] C. Emslie, "Chapter 8 - Polarization Maintaining Fibers," in *Specialty Optical Fibers Handbook*, Academic Press, 2007, pp. 243–277.
- [44] Y. Sasaki, K. Okamoto, T. Hosaka, and N. Shibata, "Polarization-maintaining and absorption-reducing fibers," in *Optical Fiber Communication*, Optica Publishing Group, 1982, ThCC6.
- [45] M. Eichhorn, *Laser physics: from principles to practical work in the lab*. Springer, 2014.
- [46] M. Eichhorn, "Quasi-three-level solid-state lasers in the near and mid infrared based on trivalent rare earth ions," *Applied Physics B*, vol. 93, pp. 269–316, 2008.
- [47] W. Koechner, *Solid-state laser engineering*. Springer, 2013, vol. 1.
- [48] A. E. Siegman, *Lasers*. University science books, 1986.
- [49] R. G. Gould *et al.*, "The LASER, light amplification by stimulated emission of radiation," in *The Ann Arbor conference on optical pumping, the University of Michigan*, vol. 15, 1959, p. 92.
- [50] B. G. Wybourne, *Spectroscopic properties of rare earths*. Interscience Publishers, 1965.

- 
- [51] P. Zhou *et al.*, “High-power fiber lasers based on tandem pumping,” *J. Opt. Soc. Am. B*, vol. 34, no. 3, Mar. 2017.
- [52] M. Meleshkevich, N. Platonov, D. Gapontsev, A. Drozhzhin, V. Sergeev, and V. Gapontsev, “415W Single-Mode CW Thulium Fiber Laser in all-fiber format,” in *CLEO/Europe and IQEC 2007 Conference Digest*, Optica Publishing Group, 2007.
- [53] D. Creeden, B. R. Johnson, S. D. Setzler, and E. P. Chicklis, “Resonantly pumped Tm-doped fiber laser with >90% slope efficiency,” *Opt. Lett.*, vol. 39, no. 3, pp. 470–473, Feb. 2014.
- [54] M. M. Broer, D. M. Krol, and D. J. DiGiovanni, “Highly nonlinear near-resonant photodarkening in a thulium-doped aluminosilicate glass fiber,” *Opt. Lett.*, vol. 18, no. 10, pp. 799–801, May 1993.
- [55] D. C. Hanna, R. M. Percival, I. R. Perry, R. G. Smart, P. J. Suni, and A. C. Tropper, “Continuous-Wave Oscillation of a Monomode Thulium-Doped Silica Fiber Laser,” in *Advanced Solid State Lasers*, Optica Publishing Group, 1989.
- [56] S. D. Jackson and S. Mossman, “Efficiency dependence on the  $\text{Tm}^{3+}$  and  $\text{Al}^{3+}$  concentrations for  $\text{Tm}^{3+}$ -doped silica double-clad fiber lasers,” *Appl. Opt.*, vol. 42, no. 15, pp. 2702–2707, May 2003.
- [57] P. C. Shardlow, D. Jain, R. Parker, J. Sahu, and W. A. Clarkson, “Optimising Tm-Doped Silica Fibres for High Lasing Efficiency,” in *2015 European Conference on Lasers and Electro-Optics - European Quantum Electronics Conference*, Optica Publishing Group, 2015.
- [58] B. Faure, W. Blanc, B. Dussardier, and G. Monnom, “Improvement of the  $\text{Tm}^{3+}$ :  $^3\text{H}_4$  level lifetime in silica optical fibers by lowering the local phonon energy,” *Journal of Non-Crystalline Solids*, vol. 353, no. 29, pp. 2767–2773, 2007.
- [59] N. J. Ramírez-Martínez, M. Núñez-Velázquez, A. A. Umnikov, and J. K. Sahu, “Highly efficient thulium-doped high-power laser fibers fabricated by MCVD,” *Opt. Express*, vol. 27, no. 1, pp. 196–201, Jan. 2019.
- [60] A. Hemming, N. Simakov, J. Haub, and A. Carter, “High power resonantly pumped holmium-doped fibre sources,” in *Optical Components and Materials XI*, M. J. F. Digonnet and S. Jiang, Eds., International Society for Optics and Photonics, vol. 8982, SPIE, 2014, p. 898 202.
- [61] X. Wang *et al.*, “Spectroscopic properties of  $\text{Ho}^{3+}$  and  $\text{Al}^{3+}$  co-doped silica glass for 2  $\mu\text{m}$  laser materials,” *Journal of Luminescence*, vol. 166, pp. 276–281, 2015.
-

- [62] D. L. Dexter, "A Theory of Sensitized Luminescence in Solids," *The Journal of Chemical Physics*, vol. 21, no. 5, pp. 836–850, Dec. 2004.
- [63] P. Laperle, C. Paré, H. Zheng, A. Croteau, and Y. Taillon, "Yb-doped LMA triple-clad fiber laser," in *Photonics North 2006*, vol. 6343, SPIE, 2006, p. 63430X.
- [64] N. Broderick, H. Offerhaus, D. Richardson, R. Sammut, J. Caplen, and L. Dong, "Large mode area fibers for high power applications," *Optical Fiber Technology*, vol. 5, no. 2, pp. 185–196, 1999.
- [65] E. Snitzer, H. Po, F. Hakimi, R. Tumminelli, and B. C. McCollum, "Double clad, offset core Nd fiber laser," in *Optical Fiber Sensors*, Optica Publishing Group, 1988, PD5.
- [66] S. D. Jackson, "Towards high-power mid-infrared emission from a fibre laser," *Nature photonics*, vol. 6, no. 7, pp. 423–431, 2012.
- [67] M. Eichhorn, "Pulsed 2  $\mu\text{m}$  fiber lasers for direct and pumping applications in defence and security," in *Technologies for Optical Countermeasures VII*, vol. 7836, SPIE, 2010, 78360B.
- [68] R. W. Boyd, *Nonlinear optics*. Academic press, 2020.
- [69] R. L. Sutherland, *Handbook of nonlinear optics*. CRC press, 2003.
- [70] G. I. Stegeman and R. A. Stegeman, *Nonlinear optics: phenomena, materials and devices*. John Wiley & Sons, 2012.
- [71] D. L. Mills, *Nonlinear optics: basic concepts*. Springer, 2012.
- [72] C. Koos, *Lecture Notes: Nonlinear Optics*. Summer Term 2018, Karlsruhe Institute of Technology (KIT).
- [73] P. E. Powers, *Field Guide to Nonlinear Optics*. SPIE, 2013.
- [74] M. Ebrahim-Zadeh. "8/44 OPOs concepts, technology and Applications II at International School on Parametric Nonlinear Optics," Youtube. (2015), [Online]. Available: <https://www.youtube.com/watch?v=9zX1v1NKeEE> (visited on 08/08/2023).
- [75] J. A. Armstrong, N. Bloembergen, J. Ducuing, and P. S. Pershan, "Interactions between Light Waves in a Nonlinear Dielectric," *Phys. Rev.*, vol. 127, pp. 1918–1939, 6 Sep. 1962.
- [76] B. D. Guenther and D. Steel, *Encyclopedia of modern optics*. Academic Press, 2018.
- [77] E. Lippert, H. Fonnum, G. Arisholm, and K. Stenersen, "A 22-watt mid-infrared optical parametric oscillator with V-shaped 3-mirror ring resonator," *Opt. Express*, vol. 18, no. 25, pp. 26 475–26 483, Dec. 2010.

- 
- [78] A. Hemming *et al.*, “A high power mid-IR ZGP ring OPO,” in *CLEO: 2013*, 2013, pp. 1–2.
- [79] A. V. Smith and D. J. Armstrong, “Nanosecond optical parametric oscillator with 90° image rotation: design and performance,” *J. Opt. Soc. Am. B*, vol. 19, no. 8, pp. 1801–1814, Aug. 2002.
- [80] S. Bigotta, G. Stöppler, J. Schöner, M. Schellhorn, and M. Eichhorn, “Novel non-planar ring cavity for enhanced beam quality in high-pulse-energy optical parametric oscillators,” *Opt. Mater. Express*, vol. 4, no. 3, pp. 411–423, Mar. 2014.
- [81] C. Ebert, T. Guiney, D. Irwin, and S. Patterson, “New advancements in 793 nm fiber-coupled modules for Tm fiber laser pumping, including packages optimized for low SWaP applications,” in *Laser Technology for Defense and Security XII*, vol. 9834, SPIE, 2016, 98340J.
- [82] T. Könnig *et al.*, “Advances in fiber coupled high power diode laser modules at 793nm and 976nm for defense applications,” in *High-Power Diode Laser Technology XX*, vol. 11983, SPIE, 2022, p. 119830I.
- [83] T. Könnig *et al.*, “Wavelength stabilized fiber coupled modules at 79x nm, 88x nm, and 97x nm with up to 600W output power based on single emitters,” in *High-Power Diode Laser Technology XIX*, vol. 11668, SPIE, 2021, 116680F.
- [84] C. Ebert, T. Guiney, J. Braker, D. Stapleton, K. Alegria, and D. Irwin, “High-power pump diodes for defense applications,” in *Laser Technology for Defense and Security XIII*, vol. 10192, SPIE, 2017, p. 101920D.
- [85] K. Oh, T. F. Morse, A. Kilian, L. Reinhart, and P. M. Weber, “Continuous-wave oscillation of thulium-sensitized holmium-doped silica fiber laser,” *Opt. Lett.*, vol. 19, no. 4, pp. 278–280, Feb. 1994.
- [86] A. Knigge, C. Knothe, U. Oechsner, and G. Federau, “Fibers with end caps,” *Physics’ Best*, pp. 2–5, 2017.
- [87] S. Sinha, K. E. Urbanek, A. Krzywicki, and R. L. Byer, “Investigation of the suitability of silicate bonding for facet termination in active fiber devices,” *Opt. Express*, vol. 15, no. 20, pp. 13 003–13 022, Oct. 2007.
- [88] N. Boling, M. Crisp, and G. Dube, “Laser induced surface damage,” *Applied Optics*, vol. 12, no. 4, pp. 650–660, 1973.
-

- [89] A. J. Glass and A. H. Guenther, "Laser induced damage of optical elements—a status report," *Applied Optics*, vol. 12, no. 4, pp. 637–649, 1973.
- [90] N. Bloembergen, "Role of cracks, pores, and absorbing inclusions on laser induced damage threshold at surfaces of transparent dielectrics," *Applied optics*, vol. 12, no. 4, pp. 661–664, 1973.
- [91] S. Boehme, E. Beckert, R. Eberhardt, and A. Tünnermann, "Laser splicing of end caps: process requirements in high power laser applications," in *Laser-based Micro-and Nanopackaging and Assembly III*, vol. 7202, SPIE, 2009, p. 720 205.
- [92] J. Limpert, F. Roser, T. Schreiber, and A. Tünnermann, "High-power ultrafast fiber laser systems," *IEEE Journal of Selected Topics in Quantum Electronics*, vol. 12, no. 2, pp. 233–244, 2006.
- [93] N. Simakov, "Development of components and fibres for the power scaling of pulsed holmium-doped fibre sources," Ph.D. dissertation, University of Southampton Library, 2017.
- [94] R. Paschotta. "Passive fiber optics." (2023), [Online]. Available: [https://www.rp-photonics.com/tutorial\\_passive\\_fiber\\_optics5.html](https://www.rp-photonics.com/tutorial_passive_fiber_optics5.html) (visited on 08/03/2023).
- [95] A. D. McLachlan and F. P. Meyer, "Temperature dependence of the extinction coefficient of fused silica for CO<sub>2</sub> laser wavelengths," *Applied optics*, vol. 26, no. 9, pp. 1728–1731, 1987.
- [96] A. D. Yablon, *Optical fiber fusion splicing*. Springer, 2005, vol. 103.
- [97] FCC FibreCableConnect GmbH. "End Cap für Multimode Fasern." (2023), [Online]. Available: [https://www.fibrecableconnect.de/produkte-dienstleistungen/technologie/end\\_cap/](https://www.fibrecableconnect.de/produkte-dienstleistungen/technologie/end_cap/) (visited on 08/03/2023).
- [98] C. Jollivet *et al.*, "Design optimization of Tm-doped large-mode area fibers for power scaling of 2  $\mu$ m lasers and amplifiers," in *Fiber Lasers XIV: Technology and Systems*, vol. 10083, SPIE, 2017, p. 100830I.
- [99] N. Simakov *et al.*, "Design and experimental demonstration of a large pedestal thulium-doped fibre," *Opt. Express*, vol. 23, no. 3, pp. 3126–3133, 2015.
- [100] T. Walbaum, M. Heinzig, T. Schreiber, R. Eberhardt, and A. Tünnermann, "Monolithic thulium fiber laser with 567 W output power at 1970 nm," *Opt. Lett.*, vol. 41, no. 11, pp. 2632–2635, 2016.



- 
- [101] D. Marcuse, "Loss analysis of single-mode fiber splices," *Bell system technical journal*, vol. 56, no. 5, pp. 703–718, 1977.
- [102] D. Marcuse, "Gaussian approximation of the fundamental modes of graded-index fibers," *J. Opt. Soc. Am.*, vol. 68, no. 1, pp. 103–109, Jan. 1978.
- [103] J. Alda, "Laser and gaussian beam propagation and transformation," *Encyclopedia of optical engineering*, vol. 999, pp. 1013–1013, 2003.
- [104] J. Bentley and C. Olson, *Field guide to lens design*. SPIE, 2012.
- [105] Zemax LLC, *Zemax opticstudio 15.5*, 2015.
- [106] L. G. Holmen *et al.*, "Tunable holmium-doped fiber laser with multiwatt operation from 2020 nm to 2200 nm," *Opt. Lett.*, vol. 44, no. 17, pp. 4131–4134, Sep. 2019.
- [107] T. S. McComb, V. Sudesh, L. Shah, R. A. Sims, and M. C. Richardson, "Widely tunable (>100 nm) continuous-wave narrow-linewidth high-power thulium fiber laser," in *Solid State Lasers XVIII: Technology and Devices*, vol. 7193, SPIE, 2009, p. 7193II.
- [108] W. A. Clarkson, N. P. Barnes, P. W. Turner, J. Nilsson, and D. C. Hanna, "High-power cladding-pumped Tm-doped silica fiber laser with wavelength tuning from 1860 to 2090 nm," *Opt. Lett.*, vol. 27, no. 22, pp. 1989–1991, Nov. 2002.
- [109] Z. Li, S. U. Alam, Y. Jung, A. M. Heidt, and D. J. Richardson, "All-fiber, ultra-wideband tunable laser at 2  $\mu\text{m}$ ," *Opt. Lett.*, vol. 38, no. 22, pp. 4739–4742, Nov. 2013.
- [110] T. S. McComb *et al.*, "High-power widely tunable thulium fiber lasers," *Appl. Opt.*, vol. 49, no. 32, pp. 6236–6242, Nov. 2010.
- [111] K. Yin, B. Zhang, G. Xue, L. Li, and J. Hou, "High-power all-fiber wavelength-tunable thulium doped fiber laser at 2  $\mu\text{m}$ ," *Opt. Express*, vol. 22, no. 17, pp. 19947–19952, Aug. 2014.
- [112] N. Simakov, A. Hemming, W. A. Clarkson, J. Haub, and A. Carter, "A cladding-pumped, tunable holmium doped fiber laser," *Opt. Express*, vol. 21, no. 23, pp. 28415–28422, Nov. 2013.
- [113] N. Simakov, A. Hemming, W. A. Clarkson, A. Carter, and J. Haub, "Tuneable Operation of Core and Cladding Pumped Holmium Fibre Lasers," in *2013 Conference on Lasers and Electro-Optics - International Quantum Electronics Conference*, Optica Publishing Group, 2013.

- [114] A. Hemming, S. Jackson, A. Sabella, S. Bennetts, and D. Lancaster, "High power, narrow bandwidth and broadly tunable  $\text{Tm}^{3+}$ ,  $\text{Ho}^{3+}$ -co-doped aluminosilicate glass fibre laser," *Electronics Letters*, vol. 46, no. 24, p. 1, 2010.
- [115] N. Dalloz, T. Robin, B. Cadier, C. Kieleck, M. Eichhorn, and A. Hildenbrand-Dhollande, "High power Q-switched  $\text{Tm}^{3+}$ ,  $\text{Ho}^{3+}$ -codoped 2  $\mu\text{m}$  fiber laser and application for direct OPO pumping," in *Fiber Lasers XVI: Technology and Systems*, vol. 10897, SPIE, 2019, 108970J.
- [116] P. Forster, C. Romano, M. Eichhorn, and C. Kieleck, "Recent advances in high-power 2  $\mu\text{m}$  fiber lasers for frequency conversion into the mid-IR," in *Nonlinear Frequency Generation and Conversion: Materials and Devices XIX*, vol. 11264, SPIE, 2020, 112640H.
- [117] P. Forster, C. Romano, C. Kieleck, and M. Eichhorn, "Advances in two-micron lasers for nonlinear conversion into the mid-IR," in *Micro-Structured and Specialty Optical Fibres VI*, vol. 11355, SPIE, 2020, p. 1 135 509.
- [118] P. Forster, C. Romano, J. Schneider, M. Eichhorn, and C. Kieleck, "High-power continuous-wave  $\text{Tm}^{3+}:\text{Ho}^{3+}$ -codoped fiber laser operation from 2.1  $\mu\text{m}$  to 2.2  $\mu\text{m}$ ," *Opt. Lett.*, vol. 47, no. 10, pp. 2542–2545, May 2022.
- [119] C. Palmer and E. G. Loewen, "Diffraction grating handbook," 2005.
- [120] B. M. Anderson, A. Taliaferro, and A. Flores, "Mode instability in kW-class thulium doped fiber amplifiers," in *Fiber Lasers XIX: Technology and Systems*, vol. 11981, SPIE, 2022, 119810Y.
- [121] C. Gaida *et al.*, "Observation of transverse-mode instabilities in a thulium-doped fiber amplifier," in *Fiber Lasers XVI: Technology and Systems*, vol. 10897, SPIE, 2019, p. 1 089 702.
- [122] B. Anderson, A. Flores, J. Grosek, and I. Dajani, "High Power Tm-doped All-Fiber Amplifier at 2130 nm," in *Conference on Lasers and Electro-Optics*, Optica Publishing Group, 2017, SM1L.3.
- [123] A. Motard *et al.*, "Diffraction limited 195 W continuous wave laser emission at 2.09  $\mu\text{m}$  from a  $\text{Tm}^{3+}:\text{Ho}^{3+}$ -codoped single-oscillator monolithic fiber laser," *Opt. Express*, vol. 29, no. 5, pp. 6599–6607, Mar. 2021.
- [124] S. D. Jackson, A. Sabella, A. Hemming, S. Bennetts, and D. G. Lancaster, "High-power 83 W holmium-doped silica fiber laser operating with high beam quality," *Opt. Lett.*, vol. 32, no. 3, pp. 241–243, Feb. 2007.

- 
- [125] A. Motard, C. Louot, I. Manek-Hönninger, N. Dalloz, and A. Hildenbrand-Dhollande, “Optimizing the performance of a monolithic  $\text{Tm}^{3+}$ ,  $\text{Ho}^{3+}$ -codoped fiber laser by FBG reflected wavelength and fiber gain matching,” *Opt. Express*, vol. 31, no. 12, pp. 18 939–18 948, Jun. 2023.
- [126] A. Hemming, S. Bennetts, N. Simakov, A. Davidson, J. Haub, and A. Carter, “High power operation of cladding pumped holmium-doped silica fibre lasers,” *Opt. Express*, vol. 21, no. 4, pp. 4560–4566, Feb. 2013.
- [127] P. Forster, C. Romano, J. Schneider, M. Eichhorn, and C. Kieleck, “High-power and highly-efficient laser operation of  $\text{Tm}^{3+}$ : $\text{Ho}^{3+}$ -codoped silica fiber lasers emitting at 2.1  $\mu\text{m}$  and 2.2  $\mu\text{m}$ ,” *EPJ Web Conf.*, vol. 267, p. 02 007, 2022.
- [128] I. Divliansky, “Volume Bragg Gratings: Fundamentals and Applications in Laser Beam Combining and Beam Phase Transformations,” in *Holographic Materials and Optical Systems*, IntechOpen, 2017, ch. 3.
- [129] A. E. Siegman, “Defining, measuring, and optimizing laser beam quality,” in *Laser Resonators and Coherent Optics: Modeling, Technology, and Applications*, vol. 1868, SPIE, 1993, pp. 2–12.
- [130] J.-C. Chanteloup, “Multiple-wave lateral shearing interferometry for wave-front sensing,” *Appl. Opt.*, vol. 44, no. 9, pp. 1559–1571, Mar. 2005.
- [131] ISO, *Lasers and laser-related equipment — Test methods for laser beam widths, divergence angles and beam propagation ratios*. Beuth Verlag, Berlin, 2005.
- [132] A. E. Siegman, “How to (Maybe) Measure Laser Beam Quality,” in *DPSS (Diode Pumped Solid State) Lasers: Applications and Issues*, Optica Publishing Group, 1998, MQ1.
- [133] R. Paschotta. “Free spectral range.” (2023), [Online]. Available: [https://www.rp-photonics.com/free\\_spectral\\_range.html](https://www.rp-photonics.com/free_spectral_range.html) (visited on 08/03/2023).
- [134] M. Polyanskiy. “Optical constants of  $\text{SiO}_2$  from Malitson et al. of 1965.” (2023), [Online]. Available: <https://refractiveindex.info/> (visited on 08/03/2023).
- [135] S. Antipov *et al.*, “Holmium fibre laser emitting at 2.21  $\mu\text{m}$ ,” *Quantum Electronics*, vol. 43, no. 7, p. 603, Jan. 2013.
- [136] O. Humbach, H. Fabian, U. Grzesik, U. Haken, and W. Heitmann, “Analysis of OH absorption bands in synthetic silica,” *Journal of Non-Crystalline Solids*, vol. 203, pp. 19–26, 1996, Optical and Electrical Properties of Glasses.
-

- [137] S. Nagel, J. MacChesney, and K. Walker, "An Overview of the Modified Chemical Vapor Deposition (MCVD) Process and Performance," *IEEE Transactions on Microwave Theory and Techniques*, vol. 30, no. 4, pp. 305–322, 1982.
- [138] T. Izawa, N. Shibata, and A. Takeda, "Optical attenuation in pure and doped fused silica in the IR wavelength region," *Applied Physics Letters*, vol. 31, no. 1, pp. 33–35, 1977.
- [139] P. Forster, C. Romano, D. Lorenz, J. Schneider, M. Eichhorn, and C. Kieleck, "Single-end-pumped  $\text{Tm}^{3+}:\text{Ho}^{3+}$ -codoped all-fiber laser at 2120 nm," in *Conference on Lasers and Electro-Optics/Europe - European Quantum Electronics Virtual Conferences*, Optica Publishing Group, 2023.
- [140] G. P. Agrawal, *Nonlinear Fiber Optics, fifth edition*. Academic Press, 2012.
- [141] M. Eichhorn and S. D. Jackson, "High-pulse-energy, actively Q-switched  $\text{Tm}^{3+}:\text{Ho}^{3+}$ -codoped silica 2  $\mu\text{m}$  fiber laser," *Opt. Lett.*, vol. 33, no. 10, pp. 1044–1046, 2008.
- [142] N. Dalloz, T. Robin, B. Cadier, C. Kieleck, M. Eichhorn, and A. Hildenbrand-Dhollande, "55 W actively Q-switched single oscillator  $\text{Tm}^{3+}:\text{Ho}^{3+}$ -codoped silica polarization maintaining 2.09  $\mu\text{m}$  fiber laser," *Opt. Express*, vol. 27, no. 6, pp. 8387–8394, 2019.
- [143] J. Schneider, P. Forster, C. Romano, M. Eichhorn, and C. Kieleck, "High pulse energy  $\text{ZnGeP}_2$  OPO directly pumped by a Q-switched  $\text{Tm}^{3+}$ -doped single-oscillator fiber laser," *Opt. Lett.*, vol. 46, no. 9, pp. 2139–2142, 2021.
- [144] J. Schneider, P. Forster, C. Romano, M. Eichhorn, and C. Kieleck, "Investigation of the pulse energy limits of actively Q-switched polarization-maintaining  $\text{Tm}^{3+}$ -doped fiber lasers," *OSA Continuum*, vol. 4, no. 5, pp. 1577–1586, 2021.
- [145] J. Schneider *et al.*, "Pulse energy enhancement by means of fiber Bragg gratings in actively Q-switched  $\text{Tm}^{3+}$ -doped fiber lasers operating at 2050 nm and 2090 nm," *EPJ Web Conf.*, vol. 267, p. 02 004, 2022.
- [146] F. Stutzki, F. Jansen, C. Jauregui, J. Limpert, and A. Tünnermann, "2.4 mJ, 33 W Q-switched  $\text{Tm}$ -doped fiber laser with near diffraction-limited beam quality," *Opt. Lett.*, vol. 38, no. 2, pp. 97–99, Jan. 2013.
- [147] A. Hemming *et al.*, "Pulsed operation of a resonantly pumped, linearly polarised, large mode area holmium-doped fibre amplifier," *Opt. Express*, vol. 22, no. 6, pp. 7186–7193, Mar. 2014.
- [148] L. G. Holmen and H. Fonnum, "Holmium-doped fiber amplifier for pumping a  $\text{ZnGeP}_2$  optical parametric oscillator," *Opt. Express*, vol. 29, no. 6, pp. 8477–8489, Mar. 2021.

- 
- [149] W. Yao *et al.*, “High-power nanosecond pulse generation from an integrated Tm-Ho fiber MOPA over 2.1  $\mu\text{m}$ ,” *Opt. Express*, vol. 26, no. 7, pp. 8841–8848, Apr. 2018.
- [150] C. D. Tran, “Acousto-Optic Devices,” *Analytical chemistry*, vol. 64, no. 20, 971A–981A, 1992.
- [151] A. P. Goutzoulis, *Design and fabrication of acousto-optic devices*. CRC Press, 2021.
- [152] P. Forster, C. Romano, M. Eichhorn, and C. Kieleck, “High-pulse-energy high-brightness Q-switched  $\text{Tm}^{3+}:\text{Ho}^{3+}$ -codoped triple-clad polarization- maintaining fiber laser,” *OSA Continuum*, vol. 4, no. 7, pp. 1907–1915, Jul. 2021.
- [153] P. Forster, C. Romano, M. Eichhorn, and C. Kieleck, “Q-switched, high average output power  $\text{Tm}^{3+}:\text{Ho}^{3+}$ -codoped triple-clad fiber laser for nonlinear frequency conversion,” in *Nonlinear Frequency Generation and Conversion: Materials and Devices XX*, vol. 11670, SPIE, 2021, 116700E.
- [154] R. Paschotta, *Field guide to laser pulse generation*. SPIE, 2008, vol. 14.
- [155] Y. Wang and C.-Q. Xu, “Actively Q-switched fiber lasers: Switching dynamics and nonlinear processes,” *Progress in Quantum Electronics*, vol. 31, no. 3, pp. 131–216, 2007.
- [156] P. G. Schunemann, “New Nonlinear Crystals for the Mid-Infrared,” in *Nonlinear Optics*, Optica Publishing Group, 2017, NTu2A.1.
- [157] J. D. Beasley, “Thermal conductivities of some novel nonlinear optical materials,” *Appl. Opt.*, vol. 33, no. 6, pp. 1000–1003, Feb. 1994.
- [158] G. Boyd, E. Buehler, and F. Storz, “Linear and nonlinear optical properties of  $\text{ZnGeP}_2$  and  $\text{CdSe}$ ,” *Applied Physics Letters*, vol. 18, no. 7, pp. 301–304, 1971.
- [159] D. E. Zelmon, E. A. Hanning, and P. G. Schunemann, “Refractive-index measurements and Sellmeier coefficients for zinc germanium phosphide from 2 to 9  $\mu\text{m}$  with implications for phase matching in optical frequency-conversion devices,” *J. Opt. Soc. Am. B*, vol. 18, no. 9, pp. 1307–1310, Sep. 2001.
- [160] L. Wang *et al.*, “Mid-infrared ZGP-OPO with a high optical-to-optical conversion efficiency of 75.7%,” *Opt. Express*, vol. 25, no. 4, pp. 3373–3380, Feb. 2017.
- [161] G. Liu *et al.*, “161 W middle infrared  $\text{ZnGeP}_2$  MOPA system pumped by 300 W -class Ho:YAG MOPA system,” *Opt. Lett.*, vol. 46, no. 1, pp. 82–85, Jan. 2021.

- [162] M. Henriksson, L. Sjöqvist, G. Strömqvist, V. Pasiskevicius, and F. Laurell, “Tandem PPKTP and ZGP OPO for mid-infrared generation,” in *Technologies for Optical Countermeasures V*, vol. 7115, SPIE, 2008, 71150O.
- [163] D. Creeden *et al.*, “Thulium fiber laser-pumped mid-IR OPO,” in *Laser Source Technology for Defense and Security IV*, vol. 6952, SPIE, 2008, 69520S.
- [164] N. Simakov *et al.*, “Mid-infrared generation in ZnGeP<sub>2</sub> pumped by a monolithic, power scalable 2- $\mu$ m source,” in *Fiber Lasers IX: Technology, Systems, and Applications*, vol. 8237, SPIE, 2012, 82373K.
- [165] M. Gebhardt *et al.*, “High peak-power mid-infrared ZnGeP<sub>2</sub> optical parametric oscillator pumped by a Tm: fiber master oscillator power amplifier system,” *Opt. Lett.*, vol. 39, no. 5, pp. 1212–1215, Mar. 2014.
- [166] C. Kieleck, A. Berrou, B. Donelan, B. Cadier, T. Robin, and M. Eichhorn, “6.5 W ZnGeP<sub>2</sub> OPO directly pumped by a Q-switched Tm<sup>3+</sup> single-oscillator fiber laser,” *Opt. Lett.*, vol. 40, no. 6, pp. 1101–1104, Mar. 2015.
- [167] J. Schneider, P. Forster, C. Romano, M. Eichhorn, and C. Kieleck, “High pulse energy ZnGeP<sub>2</sub> OPO directly pumped by a Q-switched Tm<sup>3+</sup>-doped single-oscillator fiber laser,” *Opt. Lett.*, vol. 46, no. 9, pp. 2139–2142, May 2021.
- [168] D. Lorenz *et al.*, “Nanosecond pulsed narrow-linewidth all-fiber source for ZGP-OPO pumping,” *Opt. Continuum*, vol. 2, no. 3, pp. 660–669, Mar. 2023.
- [169] Z. Sacks, O. Gayer, E. Tal, and A. Arie, “Improving the efficiency of an optical parametric oscillator by tailoring the pump pulse shape,” *Opt. Express*, vol. 18, no. 12, pp. 12 669–12 674, Jun. 2010.
- [170] G. Aoust, A. Godard, M. Raybaut, J.-B. Dherbecourt, G. Canat, and M. Lefebvre, “Pump duration optimization for optical parametric oscillators,” *J. Opt. Soc. Am. B*, vol. 31, no. 12, pp. 3113–3122, Dec. 2014.
- [171] C. Kieleck, M. Eichhorn, D. Faye, E. Lallier, and S. D. Jackson, “Polarization effects and fiber-laser-pumping of a 2- $\mu$ m-pumped OP-GaAs OPO,” in *Nonlinear Frequency Generation and Conversion: Materials, Devices, and Applications IX*, vol. 7582, SPIE, 2010, p. 758 212.
- [172] G. D. Boyd and D. A. Kleinman, “Parametric Interaction of Focused Gaussian Light Beams,” *Journal of Applied Physics*, vol. 39, no. 8, pp. 3597–3639, 1968.

- [173] A. V. Smith, *Crystal nonlinear optics: with SNLO examples*. AS-Photonics Albuquerque, NM, USA, 2018.
- [174] F. Gonthier *et al.*, “High-power All-Fiber components: the missing link for high-power fiber lasers,” in *Fiber Lasers: Technology, Systems, and Applications*, vol. 5335, SPIE, 2004, pp. 266–276.
- [175] D. Stachowiak, “High-Power Passive Fiber Components for All-Fiber Lasers and Amplifiers Application—Design and Fabrication,” *Photonics*, vol. 5, no. 4, 2018.





# List of Publications

## Journal Contributions

**P. Forster**, C. Romano, M. Eichhorn, and C. Kieleck, "High-pulse-energy high-brightness Q-switched  $\text{Tm}^{3+}:\text{Ho}^{3+}$ -codoped triple-clad polarization-maintaining fiber laser," OSA Continuum **4**(7), 2542-2545 (2021). (editor's pick)

**P. Forster**, C. Romano, J. Schneider, M. Eichhorn, and C. Kieleck, "High-power continuous-wave  $\text{Tm}^{3+}:\text{Ho}^{3+}$ -codoped fiber laser operation from 2.1  $\mu\text{m}$  to 2.2  $\mu\text{m}$ ," Opt. Lett. **47**(10), 2542-2545 (2022).

J. Schneider, **P. Forster**, C. Romano, M. Eichhorn, and C. Kieleck, "High pulse energy  $\text{ZnGeP}_2$  OPO directly pumped by a Q-switched  $\text{Tm}^{3+}$ -doped single-oscillator fiber laser," Opt. Lett. **46**(9), 2139-2142 (2021).

J. Schneider, **P. Forster**, C. Romano, M. Eichhorn, and C. Kieleck, "Investigation of pulse energy limits of actively Q-switched polarization-maintaining  $\text{Tm}^{3+}$ -doped fiber laser," OSA Continuum **4**(5), 1577-1586 (2021).

D. Lorenz, C. Romano, D. Panitzek, **P. Forster**, J. Schneider, H. Bükér, M. Eichhorn, and C. Kieleck, "Nanosecond pulsed narrow-linewidth all-fiber source for ZGP-OPO pumping," OSA Continuum **2**(3), 660-669 (2023).

## Conference Contributions

**P. Forster**, C. Romano, M. Eichhorn, and C. Kieleck, "Recent advances in high-power 2  $\mu\text{m}$  fiber lasers for frequency conversion into mid-IR," Proc. SPIE **11264**, 112640H (2020).

**P. Forster**, C. Romano, M. Eichhorn, and C. Kieleck, "Advances in two-micron lasers for nonlinear conversion into mid-IR," Proc. SPIE **11355**, 1135509 (2020).

**P. Forster**, C. Romano, M. Eichhorn, and C. Kieleck, "Q-switched, high average output power  $\text{Tm}^{3+}:\text{Ho}^{3+}$ -codoped triple-clad fiber laser for nonlinear frequency conversion," Proc. SPIE **11670**, 116700E (2021).

**P. Forster**, C. Romano, J. Schneider, M. Eichhorn, and C. Kieleck, "High-power and highly-efficient laser operation of  $\text{Tm}^{3+}:\text{Ho}^{3+}$ -codoped silica fiber lasers emitting at 2.1  $\mu\text{m}$  and 2.2  $\mu\text{m}$ ," in *Europhoton*, EPJ Web Conf. **267**, 02007 (2022).

**P. Forster**, D. Panitzek, C. Romano, D. Lorenz, J. Schneider, M. Eichhorn, and C. Kieleck, "Single-end-pumped  $\text{Tm}^{3+}:\text{Ho}^{3+}$ -codoped all-fiber laser at 2120 nm," in *Conference on Lasers and Electro-Optics/Europe – European Quantum Electronics Virtual Conferences* (2023), paper CJ-10.5.

J. Schneider, **P. Forster**, M. Eichhorn, and C. Kieleck, "High-pulse-energy actively Q-switched polarization-maintaining  $\text{Tm}^{3+}$ -doped silica fiber laser," in *OSA High-brightness Sources and Light-driven Interactions Congress (EUVXRAY, HILAS, MICS)* (2020), paper MF2C.3.

J. Schneider, **P. Forster**, C. Romano, M. Eichhorn, and C. Kieleck, "Advances in 2  $\mu\text{m}$  polarization-maintaining thulium-doped Q-switched fiber lasers for frequency conversion into the mid-IR," Proc. SPIE **11670**, 116700B (2021).

D. Lorenz, C. Romano, D. Panitzek, **P. Forster**, J. Schneider, H. Bükler, M. Eichhorn, and C. Kieleck, "Three-stage MOPA 2  $\mu\text{m}$  fiber laser for ZGP OPO pumping," Proc. SPIE **11985**, 119850H (2022).

C. Romano, D. Panitzek, D. Lorenz, **P. Forster**, M. Eichhorn, and C. Kieleck, "937 W Thulium:silica fiber MOPA operating at 2036 nm," in *Europhoton*, EPJ Web Conf. **267**, 02016 (2022).

D. Lorenz, C. Romano, D. Panitzek, **P. Forster**, J. Schneider, M. Eichhorn, and C. Kieleck, "High-peak-power  $\text{Ho}^{3+}$  and  $\text{Tm}^{3+}$ -doped fiber MOPA for mid-IR conversion," in *Europhoton*, EPJ Web Conf. **267**, 02006 (2022).

J. Schneider, **P. Forster**, D. Panitzek, D. Lorenz, C. Romano, M. Eichhorn, and C. Kieleck, "Pulse energy enhancement by means of fiber Bragg gratings in actively Q-switched  $\text{Tm}^{3+}$ -doped fiber lasers operating at 2050 nm and 2090 nm," in *Europhoton*, EPJ Web Conf. **267**, 02004 (2022).



INSTITUTE OF CONTROL SYSTEMS

LASERS AND OPTRONICS: MATERIALS,  
TECHNOLOGIES AND APPLICATIONS

01

This series contains scientific reports on laser technology and optronics performed at or in cooperation with the IRS. The topics range from laser-related materials like crystals and glasses and their elaboration over laser physics and technologies up to laser and optronic applications.

Two main aspects of the current laser research focus on power scaling and developing new emission wavelengths to bridge gaps in the electromagnetic spectrum of optical radiation, therefore opening up new fields of application.

In this work, rarely used thulium:holmium-codoped fiber lasers are investigated as promising candidates for power scaling laser radiation in the long-wavelength 2  $\mu\text{m}$  region, ranging from 2.09  $\mu\text{m}$  up to 2.2  $\mu\text{m}$ . Accompanied by an extensive setup analysis and optimization, complexity-reduced and compact free-space fiber laser sources are realized. Wavelength-fixed and tunable continuous-wave, as well as nanosecond-pulsed lasers, are built and improved within the whole dedicated wavelength range. As a potential application, a nanosecond-pulsed  $\text{Tm}^{3+}:\text{Ho}^{3+}$ -codoped fiber laser is used for nonlinear frequency conversion through an optical parametric oscillator based on the nonlinear material zinc germanium phosphide.